UNIVERSITY OF OKLAHOMA

GRADUATE COLLEGE

CONVECTION INITIATION CAUSED BY HETEROGENEOUS GREAT PLAINS LOW- LEVEL JETS

A THESIS

SUBMITTED TO THE GRADUATE FACULTY

in partial fulfillment of the requirements for the

Degree of

MASTER OF SCIENCE IN METEOROLOGY

By

JOSHUA GREGORY GEBAUER
Norman, Oklahoma
2017

CONVECTION INITIATION CAUSED BY HETEROGENEOUS GREAT PLAINS LOW- LEVEL JETS

A THESIS APPROVED FOR THE
SCHOOL OF METEOROLOGY

BY

_____
Dr. Alan Shapiro, Chair

_____
Dr. Evgeni Fedorovich, Co-Chair

_____
Dr. Petra Klein

Acknowledgements

I would like to thank my advisors Dr. Alan Shapiro, Dr. Evgeni Fedorovich, and Dr. Petra Klein for giving me the opportunity to join the BLISS group here at OU and work on this project. They gave me freedom in conducting my research, but also gave helpful advice and guidance when it was needed.

I extend my gratitude to Elizabeth Smith, Chris Riedel, Matt Flournoy, Kenzie Krocak, Allie Brannan, Shawn Handler and all the other friends I have here at OU. Their friendship has helped me get through many stressful times during the last two years.

Finally, I want to thank Kathryn Ordiway for always being willing to listen to my sometimes crazy research ideas, helping to proofread my work, and most of all, for providing love and support.

Table of Contents

List of Tables

List of Figures

Abstract

Nocturnal convection is a common feature of the Great Plains region. Forecasting this convection, however, is challenging, as the processes leading up to convection initiation (CI) can be subtle. It has been discussed in literature that the nocturnal low-level jet (LLJ) plays an important role in nocturnal CI over the Great Plains. The LLJ provides both dynamic and thermodynamic support for convection, particularly north of the jet wind speed maximum. Convection that initiates outside of this region is harder to diagnose, as the forcing is not as obvious. One of the objectives of PECAN was to better understand the role of the LLJ in CI. On three nights during the field campaign, north-south lines of CI occurred on the eastern side of the LLJ. The lines of CI were parallel to the LLJ axis and the forcing for the CI was unknown. These nights were analyzed using PECAN observations, numerical weather prediction models, and established analytical frameworks to identify the cause of the CI.

A common feature on all three nights was a horizontally heterogeneous LLJ with wind direction veering with height. The structure of these LLJs resulted in elevated convergence at the top, eastern region of the jets. The veering with height wind direction also resulted in eastward moisture advection at the top of the LLJ. Along with the moisture advection, Rapid Refresh (RAP) model cross-sections and Weather Research and Forecasting (WRF) model back-trajectories indicate that subtle lift was occurring within the LLJ. This subtle lift caused the air to become saturated as it was advected eastward, which further increased the instability. The combined analysis of observations and model output indicate that convergence, moisture advection, and subtle long term lift initiated the convection. The horizontal

heterogeneity of the LLJ can be explained by buoyancy gradients over the sloped terrain, which created a northerly thermal wind and also an east-west gradient in the geostrophic wind. As a result of the horizontal gradient in the geostrophic wind and the typical soil moisture gradient across Kansas, the daytime boundary layer was deeper in western Kansas than in eastern Kansas, which caused the vertical structure of the LLJ to vary across the slope. This ultimately led to the convergence later in the night.

Since the unique structure of the LLJ on these nights was critical for initiation the convection, a planetary boundary layer (PBL) scheme sensitivity test was conducted using WRF to determine if there was an ideal PBL scheme for modeling these CI events. It was found that the CI was highly sensitive to the PBL scheme. The Yonsei University (YSU) scheme was determined to be the best for modeling these north-south lines of CI, but all PBL schemes, including YSU, produced inaccuracies in the LLJ structure. The westerly wind maximum at the top of the LLJ tended to be stronger and higher than what was observed, and significant errors in moisture were often found in the model. This indicates that models may struggle with consistent, accurate forecasting of these north-south lines of CI. Therefore, a conceptual model for north-south lines of CI was created to aid in forecasting these events.

Chapter 1: Introduction

1.1 Low-Level Jets

1.1.1 LLJ Climatology

Wind speed maxima that occur in the lowest levels of the atmosphere have remained a heavily researched subject for over 60 years. These wind speed maxima are called low-level jets (LLJs) and depending on the cause of the jet can occur as low as 200 m above ground level (AGL) (Whiteman et al. 1997). LLJs are known to occur worldwide, but are most frequent east of mountain ranges or in coastal regions (Stensrud 1996). Many climatologies of North American LLJs have been completed, but due to the difficulty in sampling LLJs, most climatologies have either sacrificed temporal resolution to create a spatial climatology with twice daily radiosonde data (e.g. Bonner 1968; Walters et al. 2008) or sacrificed spatial information for increased temporal resolution at a specific site (e.g. Whiteman et al. 1997; Song et al. 2005). Mitchell et al. (1995) used the NOAA Wind Profiler Network (NWPN) to create a climatology that could provide both spatial and temporal information on LLJs. The NWPN, however, did not measure the low-level wind profile adequately as the wind profilers first range gate was at 500 m AGL. Therefore, the NWPN could not accurately capture LLJs for a climatology since the wind profilers cannot measure winds below 500 m and the LLJ is typically below this height (Whiteman et al. 1997). An additional problem with the NWPN is that bird migrations can cause significant biases in profiler-estimated wind speeds (Wilkzak et al. 1995).

Reanalysis data sets have also been used in an attempt to improve LLJ climatologies (e.g. Rife et al. 2010, Doubler et al. 2015). Use of these datasets also

introduces problems, however, as they tend to under represent the frequency of LLJs, especially strong LLJs (Anderson and Arritt, 2001). In a study comparing the North American Regional Reanalysis (NARR) to radiosonde observations, Walters et al. (2014) found that only 60% of LLJs were found on both the NARR dataset and the radiosonde dataset.

Despite the problems with LLJ climatologies, all spatial climatologies for North America have found a pronounced maximum in LLJ occurrence over the U.S. Great Plains (Bonner 1968; Whiteman et al. 1997; Walters et al. 2008; Rife et al. 2010, Doubler et al. 2015). Both northerly and southerly LLJs contribute to the maximum in LLJ frequency over the Great Plains, but the southerly LLJ occurs more frequently. For example, southerly LLJs occurred over twice as often as northerly LLJs in the climatology created by Song at al. (2005) at the Atmospheric Boundary Layer Experiments facility in southern Kansas. Because of this, the southerly Great Plains LLJ is often just called the Great Plains LLJ due to its frequency. The southerly LLJ over the Great Plains has a significant diurnal variation in frequency with most LLJs occurring in the early morning hours before sunrise. Lastly, the southerly LLJ also has a seasonal variation with a maximum in frequency during the summer months and minimum in frequently during the winter months. (Bonner 1968; Whiteman et al. 1997; Song et al. 2005; Doubler et al. 2015).

1.1.2 Great Plains LLJ Forcing

Due to the frequency of the nocturnal Great Plains LLJ, many studies have been conducted to determine the cause of this phenomenon. LLJs can occur anytime at

any location as a result of a synoptic scale feature, like upper tropospheric jet streaks and leeside cyclogenesis (Uccellini and Johnson 1979; Uccelini 1980), but these synoptic causes cannot explain the diurnal signal found in LLJ climatologies. Most LLJs are at least partially the result of diurnal boundary layer processes. Blackadar (1957) suggested that nocturnal LLJs are caused by an inertial oscillation of the ageostrophic wind that occurs due to the suddenly reduced frictional force as thermally generated turbulence decays after sunset. During the daytime, the boundary layer winds experience a frictional force due to turbulent mixing, therefore the daytime winds are the result of a balance between the frictional force, Coriolis force, and pressure gradient force. Since the winds are not the result of a simple balance between the Coriolis force and pressure gradient force, an ageostrophic wind must be present during the day. At sunset, the daytime force balance is interrupted as the frictional force decreases as turbulence decays. The result of the force imbalance between the Coriolis force and the pressure gradient force is a clockwise (counterclockwise) oscillation of the ageostrophic wind vector around the geostrophic wind vector in the northern (southern) hemisphere. When the ageostrophic wind aligns with the geostrophic wind, the wind speed is at a maximum.

While the concept of an inertial oscillation was basically correct in Blackadar (1957), the complete neglect of the frictional force at night was an over-simplification. With no frictional force remaining at night, the Blackadar (1957) theory could not produce a jet-like profile. The ageostrophic wind would be greatest at the surface and, therefore, the maximum wind resulting from the oscillation would be at the surface (Shapiro and Fedorovich 2010). Buajitti and Blackadar (1957) and later Shapiro and

Fedorovich (2010) were able to produce jet-like profiles using the Blackadar (1957) concept by including eddy diffusivity, but reducing its value significantly at night.

The Blackadar (1957) mechanism could create an LLJ with a maximum wind speed in any direction, where the direction of the maximum is controlled by the geostrophic wind direction. The Blackadar (1957) mechanism is also capable of producing LLJs at any location where daytime mixing is suddenly reduced. Because of this, the Blackadar mechanism cannot explain why southerly LLJs occur most frequently over the Great Plains. Another mechanism is needed to explain the LLJ maximum over this region.

Holton (1967) showed that diurnal heating and cooling of the Great Plains' eastward sloping terrain creates a diurnally oscillating pressure field that is able to produce southerly nocturnal low-level wind maxima. The Holton mechanism can explain the direction and location of the Great Plains LLJ, but the Holton mechanism is not able to replicate the strength of the LLJs that are typically observed at night over the Great Plains.

Bonner and Paegle (1970) modeled the combined effect of the Blackadar and Holton mechanisms using a prescribed diurnally varying geostrophic wind and eddy diffusivity. The resulting LLJs were stronger than LLJs produced by the Blackadar mechanism alone. This study was expanded upon by Paegle and Rasch (1973) which allowed the modeled LLJs to be horizontally heterogeneous (i.e. by including advection terms). However, to simplify the problem, Paegle and Rasch (1973) assumed that the first order spatial derivatives of the flow field were constant (so second and higher order spatial derivative terms were zero). Similar to Bonner and

Paegle (1970), Paegle and Rasch (1973) found that LLJs were stronger when both eddy diffusivity and the geostrophic wind were diurnally oscillating. Since Paegle and Rasch (1973) allowed for heterogeneity, they were able to assess vertical motions created by the modeled LLJs. They found that the modeled heterogeneous LLJs which were forced by both diurnally varying eddy diffusivity and geostrophic wind had more significant vertical motions than heterogeneous LLJs that were forced with only with diurnally varying eddy diffusivity. This lead Paegle and Rasch (1973) to the conclusion that the sloped terrain was important for creating the convergent features of the Great Plains LLJ. (LLJ convergence and its impacts is discussed in section 1.3.2.)

While Bonner and Paegle (1970) and Paegle and Rasch (1973) were able to model the diurnal variations due to sloping terrain, they did not specifically model the flow over a slope. Shapiro and Fedorovich (2009) found that the buoyancy effects due to the slope augment the inertial oscillation. Positive buoyancy over the slope leads to upslope wind and negative buoyancy results in downslope winds, but upslope winds decrease buoyancy with time and downslope winds increase buoyancy with time. Therefore, motions up and down the slope create a gravity oscillation. Since the inertial oscillation over the slope creates upslope and downslope winds, the LLJs over the slope are actually due to an inertial-gravity oscillation. Using this concept, Shapiro et al. (2016) created a 1-D analytical model with diurnally varying eddy diffusivity and surface buoyancy over a slope which was qualitatively consistent with observed LLJ wind speeds. While this model does not consider heterogeneity, it strongly suggests the Great Plains LLJ is the result of a combination of an inertial-gravity oscillation and diurnally oscillating pressure due to heating of the sloped terrain.

An additional theory for the frequency of the Great Plains LLJ was put forth by Wexler (1961). According to Wexler (1961), the southerly LLJ maximum is due to the blocking of easterly flow on the southern side of the Bermuda high. The southerly flow produced by this blocking would be analogous to the western boundary ocean currents. Wexler (1961) argues that this southerly flow arises from conservation of potential vorticity. Since the Coriolis parameter increases with latitude, anticyclonic shear must develop to conserve potential vorticity which causes the persistent strong southerly flow over the Great Plains. There has been some support for Wexler's theory. Ting and Wang (2006) used a global circulation model to examine the forcing of the mean southerly wind by removing the North American topography in the model, concluding that the blocking of the Bermuda high is the dominant mechanism in producing the mean southerly flow. However, the Wexler (1961) theory has also been called into question as the conditions observed over the Great Plains do not correspond to a blocked flow scenario and instead suggest that thermal forcing is the cause of the mean southerly flow (Parish and Oolman, 2010). Parish (2016) suggested that the mean heating of the sloped terrain during the summer increases the east-west pressure gradient force which creates the mean southerly flow. Even if the Wexler (1961) theory is valid, it cannot explain the diurnal variation in LLJ occurrence and, therefore, the previously discussed diurnal boundary layer forces are likely the key factors in the Great Plains LLJ development.

1.2 Great Plains Nocturnal Convection

The U.S. Great Plains has a nocturnal maximum in precipitation (Wallace 1975). This nocturnal maximum is most pronounced in the summer months of June, July, and August when nighttime precipitation exceeds daytime precipitation by 25% (Higgins et al. 1997). This nocturnal precipitation is primarily caused by thunderstorms which contradicts conventional knowledge of thunderstorm initiation as these storms occur during the development of a stable boundary layer. Due to the surface stability, these nocturnal thunderstorms are often elevated, meaning the storm's updraft does not extend down to the surface. Clusters of these elevated thunderstorms often organize into a mesoscale convective complex (MCC) (Maddox 1980). An MCC is defined to be a long-lived cluster of thunderstorms that satisfies the enhanced infrared (IR) satellite conditions in Table 1 of Maddox (1980). The thunderstorm complex must have cloud tops with a temperature below -32°C that cover over 100,000 km^2 and an interior region with cloud tops that are below -52°C and cover over 50,000 km^2. Also, this IR satellite signature must persist for more than 6 hours. MCCs develop when the cold pools from a group of smaller separate thunderstorms coalesce. In the presence of warm moist inflow (such as an LLJ), the boundary of the now larger cold pool leads to the initiation of additional thunderstorms and the development of an MCC (Maddox 1980).

While progress has been made in identifying the cause of MCC development once convection has initiated, the processes behind the actual initiation of convection at night is poorly understood. While not focused specifically on nocturnal convection initiation, Weckwerth and Parsons (2006) completed an in depth review of the

common features that are capable of initiating convection in the Great Plains region. In addition to low-level convergence, Weckworth and Parsons (2006) discuss how drylines, frontal boundaries, gust fronts, horizontal convective rolls, undular bores, and land surface effects have all been known to initiate convection. Weckworth and Parson (2006) note that the occurrence of these features does not necessarily guarantee the initiation of convection, and convection has been observed to initiate when none of these features are obviously present. The conditional nature of convection initiation (CI) leads to low confidence forecasts for convection. Sensitivity studies of CI in models have shown that a 1 K change in temperature and a 1 g/kg change in specific humidity can make the difference between whether or not convection is initiated (Crook 1996).

Many times convergent boundaries that potentially cause convection can be seen on radar as a fine-line of reflectivity. In a study of convection initiation in Colorado, Wilson and Schreiber (1986) found that 80% of convection was initiated within 10 km of a radar fine line. A study by Wilson and Roberts (2006), however, classified approximately half of the convection initiation episodes during the study as elevated without an obvious association with a front or other surface mesoscale convergence boundary. Two-thirds of the convection initiation episodes that were classified as elevated in the Wilson and Roberts (2006) study were found to occur in elevated convergent regions between 900 and 600 hPa. These convergent features were of large enough scale that they could be resolved on the 10 km Rapid Update Cycle (RUC10) reanalysis. The cause of these elevated convergent regions was not discussed in the study.

Since understanding of much of the convection initiation over the Great Plains is lacking, forecasting for nocturnal elevated thunderstorms and MCCs over the Great Plains is one of the most challenging problems remaining in forecasting. Davis et al. (2003) found that numerical weather prediction does a poor job of forecasting nocturnal convection over the Great Plains. Davis et al. (2003) suggested that the convective parameterizations in the models were to blame for the poor nocturnal convection forecasts. Since the Davis et al. (2003) study, strides have been made in improving the numerical prediction of nocturnal thunderstorms as higher resolution models have been developed. Clark et al. (2007) compared a 5 km convective-allowing Weather Research and Forecasting non-hydrostatic mesoscale model (WRF-NMM) model to a 22 km convective-parameterized WRF-NMM model and found that the 5 km model had significantly more skill in modeling the nocturnal convection. Pinto et al. (2015) analyzed how well the High Resolution Rapid Refresh (HRRR) model predicted thunderstorms over the Great Plains. The HRRR model is considered to be one of the flagship models for predicting convection at short time scales, but Pinto et al. (2015) revealed that the HRRR tends to over-predict thunderstorm initiation over the Great Plains.

1.3 Low-Level Jet Role in Convection Initiation

The Great Plains LLJ plays a central role in the nocturnal precipitation maximum found in this region, as the LLJ facilitates the development of nocturnal thunderstorms, including MCCs, due to its transport of moisture and creation of elevated convergent regions (Maddox 1983; Stensrud 1996).

1.3.1 Moisture Transport

Rasmussen (1967) discovered that there was a well-organized diurnal oscillation of horizontal moisture flux over the Great Plains associated with the frequent nocturnal LLJs in the region. Using reanalysis datasets, Higgins et al. (1997) also identified a significant diurnal cycle for moisture flux over the Great Plains. Specifically, the increased moisture flux was due to an increase in wind speeds at night and not an increase in specific humidity. Due to the increased moisture flux, the nocturnal atmosphere over the Great Plains remains favorable for convection despite the development of a stable boundary layer.

The LLJ can also contribute to the mesoscale transport of moisture. Data from the International H_2O Project (IHOP) reveals that the upper levels of the LLJ have well-defined moisture flux gradients (Tollerud et al. 2008). These mesoscale moisture flux gradients at the top of the LLJ may play a key role in what appears to be the random occurrence of convection during the night. Dropsondes from the IHOP campaign also indicate that there is significant moisture transport across the LLJ axis. This transverse moisture flux could not be examined in detail, however, as the transects taken through the LLJ were west-to-east; thus, the remote sensing instruments could only measure the meridional transport of moisture.

1.3.2 Convergence

In addition to moisture transport, the LLJ can create convergence which causes areas of ascent which further enhances the favorability of nocturnal convection over

the Great Plains. Pitchford and London (1962) discovered that on nights with significant coverage of nocturnal thunderstorms (at least 25% of surface stations in the domain) the storms were associated with convergent regions of the LLJ in 96% of cases. Other studies have found similar results. Paegle and McLawhorn (1973) created a boundary layer model to study the influence of convergence on nocturnal thunderstorms over the Great Plains. They found that model forecasted convergence alone was not able to predict thunderstorm development, but supplementing the forecasted convergence with additional information on stability better predicted the convective regions.

The northern terminus of the LLJ receives the most research attention on the topic of LLJ convergence and nocturnal thunderstorms. Astling et al. (1985) presented a case study of a 5-day period to show that convergence at the northern terminus facilitated thunderstorm development during the time period. The convergence at the northern terminus can also promote frontogenesis, which further enhances lift for nocturnal thunderstorm development. Both Trier et al. (2006) and Tuttle and Davis (2006) have proposed that the combination of convergence and frontogenesis at the terminus of the LLJ explains the existence of heavy rainfall corridors that Corbone et al. (2002) found develop over ~3 day periods in the Great Plains region. These heavy rainfall corridors are often the result of consecutive nights of MCCs that develop at the northern terminus of the LLJ. Trier and Parsons (1993) identified that the intersection of LLJs and frontal boundaries is a favorable region for CI and MCC development. In the set-up described by Trier and Parsons (1993), the LLJ is lifted over a frontal boundary into the cool side of the boundary where the environment is more favorable

for convection. The convergence at the northern edge of the LLJ provides additional lift to initiate convection.

While the northern terminus is often the strongest region of convergence produced by the LLJ, it is not necessarily the only convergent region. In an LLJ airflow configuration study, half of the identified LLJs had a wind direction that changed with height (Walters and Winkler, 2001). This indicates that the convergent regions of these LLJs would change with height as well due to the different wind direction. In fact, Walters and Winkler, (2001) mentions that there tends to be additional convection on the eastern side of LLJs that have winds that change with height due to the more westerly winds at higher elevations. Also, the direction of LLJ convergence is not necessarily constant. The veering of the LLJ with time can cause the convergence regions to shift as the night progresses. This shifting convergence can help to sustain thunderstorms after they move away from the initiation area, but can also can have the opposite effect of suppressing convection if the convergence moves away from the location of the storms and divergence develops (Bonner 1966). Changes in convergent regions with time are most evident on the flanks of the LLJ. Bonner (1966) presented a case study of convergence changing with time on the edges of the LLJ. At 00 UTC the rising motion associated with low-level convergence was present on the west side of the LLJ and sinking motion associated with divergence was present on the east side of the LLJ, but by 12 UTC the pattern changed and the west side of the LLJ was divergent while the east side of the LLJ was convergent.

1.4 Thesis Motivation

1.4.1. Plains Elevated Convection at Night Experiment

The Plains Elevated Convection at Night (PECAN) project was conducted to elucidate the processes contributing to the nocturnal thunderstorm maximum over the Great Plains. The field campaign occurred from 1 June 2015 through 15 July 2015 and focused on four nocturnal phenomena: mesoscale convective systems (MCS, a subset of MCCs), convection initiation (CI), bores, and LLJs. The PECAN observing platforms consisted of 6 fixed-location PECAN Integrated Sounding Arrays (PISA), 5 mobile PISAs, 3 mobile radiosonde launch vehicles, multiple mobile mesonets, 1 fixed radar, 9 mobile radars, and 3 aircraft (Geerts et al. 2016). The PISA network (Fig. 1) was a unique aspect of PECAN as each PISA site provided low-level profiles of, at least, wind, temperature, and water vapor using both in situ and remote sensing observations. The instruments that were used to obtain the profiles at each PISA site is shown in Table 1.

During the field campaign, there were 31 intensive observation periods (IOPs) where mobile units were deployed to collect organized observations. These IOPs were conducted when PECAN forecasters indicated that conditions were favorable for at least one of the targeted phenomenon. The target breakdown for the IOPs was: 13 MCS, 5 CI, 5 bore, 4 LLJ, 3 CI/LLJ, and 1 Dry Run. Observations at the fixed PISAs (except for radiosonde launches) were gathered even if a IOP did not occur. This ensured that even if an IOP was not conducted, there were still some observations if an event of interest were to occur. The fixed PISAs were, therefore, very useful as data sources for CI events as the forecasting uncertainty associated with CI made it difficult

to accurately predict when and where CI was going to occur. For more information on PECAN see Geerts et al. (2016).

1.4.2. Research Questions

As discussed in the previous sections there have been many studies of the LLJ and the nocturnal thunderstorm maximum over the Great Plains, but there are still many unanswered questions. Forecasting CI in regions of the LLJ other than the northern terminus on nights without frontal boundaries remains difficult. This difficulty can be seen in the PECAN forecast discussions where forecasters were often unsure of their CI forecasts. The forecast discussion for 2 June 2015 in particular stands out. The PECAN forecaster mentioned that numerical weather prediction (NWP) models were forecasting for pristine CI in eastern Kansas, but the forecaster was unsure of the mechanism causing the CI. The models appeared to show that the CI was not occurring at the northern terminus of the LLJ and there was no surface or 850 hPa front to initiate convection. Due to the forecasters' uncertainty in the mechanism causing the CI, only low and moderate probabilities of CI were issued even though most models were forecasting for CI to occur. The CI forecasted by the models did occur in a north-south line on the eastern edge of the LLJ right before sunrise (Fig. 2). After radar analysis of the other 45 nights of PECAN, two additional nights were identified where a similar north-south line of CI developed. These nights were 1 June 2015 and 5 July 2015 (Fig. 2). These nights in addition to the night of 2 June 2015 were analyzed to answer the following questions:

1. What role does the Great Plains LLJ play in the initiation of these north-south lines of convection? What ultimately was the initiation source for these north-south lines of convection. Was a mechanism similar to the one discussed in Bonner (1966) involved?

2. What is the sensitivity of the CI to the environment and LLJ and can these north-south lines of convection be accurately forecasted given this sensitivity?

Possible answers to these questions will be presented in this thesis. Chapter 2 covers the analysis of these three nights using a combination of PECAN observations, Rapid Refresh (RAP) forecasts, and RAP analyses. Chapter 3 discusses the simulation and trajectory analysis of these CI events using WRF. In Chapter 4, the forcing for the LLJs on these nights is discussed and a conceptual model for the development of these north-south lines of convection is presented. Lastly, conclusions are stated in Chapter 5.

Chapter 2: Analysis of Selected Convection Initiation Events

2.1. 2 June 2015

The analysis of the 2 June 2015 CI case is presented first as the information gathered from this case led to the identification and aided in the analysis of the other two CI events.

2.1.1. Radar Overview of CI Event

On 2 June 2015 at 00 UTC, radar indicated that scattered thunderstorms were present along the front range of the Rocky Mountains (Fig. 3a). One cluster of storms in the Nebraska panhandle was stronger and more organized than the other scattered convection. By 04 UTC, most of the scattered convection had dissipated, but the storm in the Nebraska panhandle grew upscale into a small MCS with a limited trailing stratiform region (Fig. 3b). This MCS did not persist very long. As the system moved southeast it weakened rapidly and by 09 UTC only a stratiform region of precipitation remained (Fig. 3c). New CI developed in a short north-south line just ahead of the decaying MCS. What appeared to be numerous boundaries were visible on radar at this time. One such boundary was oriented in an east-west direction south of the stratiform rain and another boundary with a northeast-southwest orientation was located to the east of the stratiform rain. CI was occurring on the northern edge of this eastern boundary. Curiously, the north-south line of CI that occurred just to the east of the decaying MCS did not have the typical appearance of being initiated by a boundary as the orientation of the CI was almost orthogonal to the boundaries visible on radar. By 12 UTC almost all remnants of the MCS dissipated (Fig. 3d) and a new

north-south line of convection developed. This line was longer than the first line of CI and also did not have the typical appearance of boundary-initiated CI.

2.1.2. Synoptic Conditions

The Rapid Refresh (RAP) analysis was used to examine the large scale upper air and surface features that were present over the continental United States (CONUS) and, more specifically, the PECAN domain on the night of 2 June 2015. The RAP is an assimilation and model forecast system that provides hourly updated model analysis and forecasts (Benjamin et al., 2016). Every hour, the previous RAP forecast is used as a baseline and observations from platforms such as radiosondes, radar, aircraft, and satellites are assimilated into the RAP forecast to create an analysis. This analysis is then used to initialize the next model forecast. The analysis of the synoptic conditions was done at 00 UTC and 12 UTC to identify how synoptic scale features evolved throughout the night and to determine if these features could have initiated the CI.

At 00 UTC at the 250 hPa a trough which was separated from the main flow was located over the Mississippi Valley region (Fig. 4a). Upstream from this trough a ridge was present over the Great Plains which displaced the jet stream well north into Canada. Winds over Kansas at this height were weak out of the northwest. In the western U.S., there was a jet streak moving in from the coast of California that was still well west of the PECAN domain. At 500 hPa, the trough over the Mississippi Valley was vertically stacked under the 250 hPa trough (Fig. 4b). The ridge axis over the Great Plains at this height was slightly further west than at 250 hPa. The winds

over Kansas were still very weak, but they had a more northerly component. Overall, the 250 hPa and 500 hPa analysis does not indicate that there was upper level synoptic scale forcing for convection over the Great Plains. At the 700 hPa level (Fig. 4c), both the Mississippi Valley trough and the Great Plains ridge had a smaller amplitude, and were less defined. Once again, the winds over Kansas were weak, but at this height the wind direction varied across the state. In western Kansas the winds were out of the southwest, but in eastern Kansas the winds were northwesterly. The RAP analysis also had an area of relatively stronger winds near the location where the small MCS developed. At 850 hPa, the winds over the western Great Plains were southerly (Fig. 4d). These southerly winds extended from central Texas all the way up into Canada. It appears that at 00 UTC the LLJ may have been beginning to develop as the winds in the southerly flow were relatively stronger than the winds elsewhere, as the winds were weak and variable in eastern Kansas and the Mississippi Valley. An east-to-west temperature and moisture gradient was present over Kansas at this height (Fig. 5a), with greater temperature and specific humidity in western Kansas. The temperature gradient is not unusual for this region. The eastward sloping terrain of Kansas causes the 850 hPa level to be much closer to the ground in western Kansas. Since the ground is closer to 850 hPa in western Kansas, the temperature at 850 hPa in western Kansas will be greater than in eastern Kansas. The moisture gradient, however, is quite unusual. Western Kansas is typically dryer due to subsiding air from the Rocky Mountains, which often creates a sharp gradient in moisture called a dryline. In this case, however, it appears the stronger southerly winds in western Kansas advected moisture into this region, while weaker winds in eastern Kansas could not do the same

creating this unusual moisture gradient. Lastly, at the surface, the winds in eastern Kansas were easterly while the winds in western Kansas were faster and southeasterly (Fig. 5b). The temperature and moisture gradient were not as apparent at the surface, but the moisture in western Kansas was still greater than the moisture in eastern Kansas.

There was not much change in the upper levels at 12 UTC. At both 250 hPa (Fig. 6a) and 500 hPa (Fig. 6b) the ridge over the Great Plains developed a positive tilt. This caused the winds at these levels in western Kansas to become westerly, while the winds in eastern Kansas are northerly at 250 hPa and northwesterly at 500 hPa. The nose of the jet streak which was moving into the western U.S. at 00 UTC, weakened slightly and moved northwest, though this feature still did not impact the PECAN domain. The upper levels at 12 UTC remained neutral for convection over the Great Plains. At 700 hPa, the winds over Kansas increased. There appeared to be a perturbation in the isohypses along the Kansas/Colorado border. This region is close to the area the small MCS propagated through earlier in the night. Just to the east of this perturbation was a small southwesterly wind maximum. There was a diffuse wind shift across Kansas with north-northwesterly winds in eastern Kansas. The southwesterly wind maximum caused slight convergence in south-central Nebraska and north-central Kansas, near the location of the first north-south line of CI on this night. At 850 hPa the LLJ was clearly seen over the Great Plains. The winds were approximately 30 kts out of the southwest in the center of the LLJ, which had a defined eastern edge with the winds in eastern Kansas being quite weak at this level. The second north-south line of CI that developed on this night occurred near this sharp gradient in wind speed

where convergence would be present. The temperature gradient at 850 hPa relaxed slightly by 12 UTC. A significant change in moisture from 00 UTC had occurred; the moisture in eastern Kansas increased substantially while in western Kansas moisture decreased. The increase in moisture in eastern Kansas also coincides with the location of the CI that occurred on this night. Finally, at the surface not much changed by 12 UTC. The winds were still out of the west-southwest, though they had weakened, and the temperature and moisture field was more uniform. There was still more moisture at the surface in western Kansas than in eastern Kansas, which suggests that differential moisture advection was occurring.

2.1.3. PECAN Observations

The night of the 2 June 2015 CI event was the first intensive observation period (IOP) of the PECAN field experiment, but since it was the first IOP, the deployment primarily was for practice and had a limited scope. The mobile observing platforms were positioned in northwest Kansas and observations ended at 05 UTC. Due to the location and short duration of the IOP, the mobile observations provided little benefit to the analysis of the CI event. Even though the mobile observations were not useful, the observations from the fixed PISAs can be used for the analysis. Unfortunately, not all of the instruments at the fixed PISA sites were operating on this night as some instruments were not yet deployed. However, all of the fixed PISAs launched a radiosonde at 03 UTC.

At FP-5, profiles from the 03 UTC sounding shows the LLJ was veering with height and specific humidity greater than 10 g/kg extended up to 2.25 km ASL. (Fig.

8). The veering with height LLJ resulted in a maximum u-component of the wind at 2.5 km ASL. The low-level lapse rates at this location were weak, but due to an elevated mixed layer, steep lapse rates were present above 750 hPa (Fig. 9). The 915 MHz wind profiler at FP-5 shows that the LLJ began developing around 02 UTC, but the LLJ was interrupted around 06 UTC (Fig. 10). Radar shows a boundary emanating from the MCS in Nebraska passing over the site around this time. Surface observations reveal that the first boundary was likely an outflow boundary, but around 0730 UTC a temperature spike and pressure jump occurred which is indicative of a bore passage at that time (Fig. 11). The outflow boundary and bore did not initiate any convection in this part of Kansas.

The FP-2 and FP-3 03 UTC soundings are remarkably similar. These two sites had nearly the same longitude so the similarity in the soundings suggests that there was little north-south heterogeneity in both the LLJ and atmospheric stratification. The LLJ at these two sites was veering with height, with a maximum u-component at 2 km ASL. Both soundings had a stronger capping inversion than the sounding at FP-5. The region below the capping inversion around 800 hPa was nearly saturated, but was stable. The mid-level lapse rates at FP-2 and FP-3 were also much smaller than at FP-5. These two fixed PISA sites were near the longitude where the MCS began to dissipate. The reduced mid-level lapse rates likely contributed to the dissipation of the MCS.

Many of the instruments at the FP-2 site were not working on this night, though the Atmospheric Laboratory for Validation, Interagency Collaboration and Education (ALVICE) Raman lidar was available during the IOP. The Raman lidar is

able to provide continuous high vertical and temporal resolution moisture profiles at the FP-2 site (Whiteman et al. 1992). The lidar was turned off shortly after the end of mobile observations on this night, but a slight increase in the height of the moisture at FP-2 can be seen just before the end of observations (Fig. 12).

Like at FP-5, the Doppler lidar at FP-3 captured a late developing LLJ (Fig. 13). The Doppler lidar shows the veering of the LLJ with both height and time. The LLJ at this site was able to be observed in great detail, and one interesting feature is a diagonal striation in the wind speed at the top of the LLJ beginning at 08 UTC. There was also a 449 MHz wind profiler at FP-3 (Fig. 14). The two profiling platforms are in reasonable agreement, but the 449 MHz observed wind speeds are stronger than those observed by the Doppler lidar. The 449 MHz profiler also shows an increase in westerly winds at the top of the LLJ at 06 UTC that the Doppler lidar does not capture, but the profiler is not able to observe the LLJ with the same detail as the Doppler lidar. The FP-3 site also had the water vapor DIAL system for high temporal resolution moisture profiles (Spuler et al. 2015). The DIAL shows an increase in moisture at 1.75 km AGL around 06 UTC (Fig. 15), which is also when a significant westerly component of the LLJ develops at this height, as shown by the 449 MHz wind profiler. The more diffuse water vapor profile after 07 UTC suggests that the moisture was mixed. Radar and surface observations reveal that a bore passed over this site around 0930 UTC (Fig. 16), but the mixing occurred well before this time.

The FP-6 site was the furthest east fixed PISA in the PECAN domain. This site was, therefore, closest to the CI region. Like at the other FP sites, the 03 UTC sounding shows the veering with height LLJ, but the LLJ is weaker at this location.

There is a maximum u-component of the LLJ from 1.5-2.5 km ASL. The boundary layer moisture is lower at this site with a layer of specific humidity greater than 8 g/kg extending up to 2 km ASL. The capping inversion was even stronger at this location than at the other fixed PISAs. The region just below the capping inversion was saturated but stable. Mid-level lapse rates at this location were also unfavorable for convection. Unfortunately, the wind profiling instruments were not available on this night at FP-6, so the evolution of the LLJ at this site was not observed.

While not officially part of the PECAN dataset, the 00 UTC and 12 UTC Topeka soundings provide insight into the thermodynamic profile evolution near the CI region (Fig. 17). The 00 UTC Topeka sounding shows a very strong inversion around 860 hPa and an extremely dry layer was present above this inversion. This inversion is at a lower height than the inversions to the west, as shown by the FP soundings. By 12 UTC, the inversion at 860 hPa was still present, but the former dry region above the inversion was now saturated at 825 hPa with a specific humidity of 11 g/kg. The 03 UTC soundings at the fixed PISA sites to the west showed mixing ratios of 11 g/kg extending up to the 800 hPa level. There was a westerly component to the LLJ at that height evident on the FP soundings. This suggests that the LLJ advected the moisture in western Kansas eastward, above the capping inversion in eastern Kansas, where there was less stability. The RAP analysis shown in the previous section also indicated that convergence was present in this area, which could have lifted the unstable parcels. Data from the FP sites and soundings did not reveal an obvious initiation mechanism for the convection in eastern Kansas, but the observations clearly show that a vertically veering LLJ caused a significant moistening

of the region above the capping inversion at the CI area through differential moisture advection.

2.1.4. RAP Forecast

As discussed in the motivation section of this thesis, the NWP models had a strong signal for CI for this night. In particular, the second episode of CI that occurred near Topeka was predicted reasonably well. The limited PECAN observations revealed that differential moisture advection caused by the LLJ played a key role in destabilizing the CI region, but the evolution and horizontal structure of the LLJ was not well captured by the limited PECAN observations. An analysis of one of the model forecasts for 2 June 2015 was used to help better understand the evolution of the LLJ on this night and to elucidate the role of the LLJ in initiating convection. The 00 UTC RAP forecast (not to be confused with the RAP analysis) was chosen for this purpose. The 00 UTC RAP forecast had an over amplified signal for CI (Fig. 18), so the processes involved in causing the CI should be well represented in the forecast. The RAP forecast was used instead of the RAP analysis for two reasons. First, the RAP forecast allowed for a more complete analysis of the LLJ evolution since the LLJ forecasted in the model would have to obey physical laws such as mass conservation. The hourly analysis might not represent the LLJ evolution accurately due to the hourly data assimilation. The data assimilation, while helping to improve the accuracy of the analysis, could result in an inconsistent representation of the evolution of the LLJ. Second, the 00 UTC RAP forecast failed to predict the MCS that developed in

southwest Nebraska but was still able to predict the CI. This was seen as a benefit as the processes leading to the amplified CI signal would not be influenced by the MCS.

The RAP model has 13 km grid spacing and therefore does not explicitly resolve convection. Typically, a model with this grid spacing would not be used for convective studies, but Wilson and Roberts (2006) found that many of the convergent features associated with elevated CI during IHOP were able to be resolved in the RUC10 analysis which had 10 km grid spacing. This suggests that a model with 13 km grid spacing should be able to resolve these large scale convergent features, such as those that would develop due to the LLJ.

Cross-sections of the 00 UTC RAP forecast over central Kansas were used to examine the vertical and east-west structure of the forecasted LLJ since observations from this night suggested that these dimensions were the most heterogeneous (Fig 19). At 00 UTC, the moisture gradient across Kansas can be clearly seen. The sloping terrain of the Great Plains created a tilted boundary layer as evidenced by the potential temperature field. This tilted boundary layer is similar to the tilted residual layer concept discussed in Shapiro and Fedorovich (2009). The tilted boundary layer caused the moisture gradient to increase at greater heights ASL. The PECAN soundings confirm that this had occurred. At this time, the forecasted LLJ was began to develop in western Kansas. The surface winds in the forecasted LLJ region were southeasterly while near the top of the boundary layer the winds were from the south-southwest. By 04 UTC, the RAP forecasted for the LLJ to continue to develop. The forecasted LLJ became broader, but the most intense region was still in western Kansas. In central Kansas, the forecasted LLJ was shallower and less intense. The eastern edge of the

LLJ also veered more strongly with height. The top of the forecasted LLJ began to advect the moisture in western Kansas toward the east due to the increasing strength of the winds and the veering of the winds with time. The winds in the lower portion of the LLJ still had an easterly component, so the sign of the moisture advection was actually opposite near the surface. At 08 UTC the eastward moisture advection was still occurring at the top of the LLJ, but was also present in the middle levels of the LLJ due to the veering of the winds with time. The isentropes were slightly slanted downward toward the west, indicating that the southwesterly and westerly winds at the top of the forecasted LLJ could be subjected to subtle isentropic lifting. This cannot be confirmed since in order to accurately diagnose isentropic lift, one needs to know how the isentropic surface heights themselves change with time. Using water vapor as a passive tracer, however, does suggest that isentropic lift was occurring. At 12 UTC, the RAP model was predicting for precipitation near 96°W. The cross-section shows the edge of the elevated moisture at this longitude. This moisture had been advected above a stable layer into a more favorable region for convection which agrees with the observed soundings at Topeka, KS.

Model soundings at the CI location were created to evaluate the forecasted evolution of the thermodynamic profile of this region in the model (Fig. 20). The RAP sounding for 00 UTC at the CI region shows a relative dry layer between 850 and 750 hPa. This layer was not as dry as the layer in the 00 UTC Topeka sounding, but the relative dry layer suggests the RAP had the general set-up correct. The model sounding shows that instability at this location was not large, as mid-level lapse rates were not conducive for convection. By 04 UTC significant moisture advection had

already occurred and the former dry layer at the 800 hPa region became a local maximum in moisture. By 08 UTC, the moisture advection had caused the 800 hPa region to become almost saturated and the 900 hPa region was now also experiencing an increase in moisture. The cross-sections showed the middle levels of the LLJ with a westerly component at this time, so a deeper layer of moisture advection is not surprising. Lastly at 12 UTC, the region from 800 hPa down to the surface was saturated due to the enhanced moisture advection and potential isentropic lift that the cross-section showed could occur. While the most-unstable CAPE was not large, the saturation of this layer had resulted in an unstable layer with no CIN.

In order to show that the increase in moisture in eastern Kansas was due to eastward moisture advection across the LLJ axis and not southerly moisture advection, the 800 hPa RAP model forecast is shown for this region (Fig. 20). At 00 UTC a strong east-west moisture gradient was present and by 12 UTC the moisture that was previously in western Kansas had shifted eastward. The 12 UTC forecast also shows the convergence that developed on the eastern edge of the LLJ. The convergence was also present on the 00 UTC analysis, but the winds were weaker and there was limited moisture at this time which prevented CI. The development of the enhanced convergence on the eastern edge of the LLJ at 12 UTC is similar to the LLJ examined by Bonner (1966). The 00 UTC RAP model forecast suggests that increased convergence on the eastern edge of the veering with height and time LLJ, combined with eastward moisture advection and slight isentropic ascent, produced the CI on this night.

2.1.5. Summary of Event

On 2 June 2015, two north-south lines of CI developed in central and eastern Kansas. The overall synoptic pattern for this night was quiescent with no major upper-level features present to initiate convection. There was a substantial east-west moisture gradient present with western Kansas having more moisture than eastern Kansas. Observations from the fixed PISA array showed a late developing, veering with height LLJ occurred in western and central Kansas. Soundings from near the CI area at Topeka revealed that significant moisture advection occurred in the 800 hPa layer, which resulted in a nearly saturated layer by 12 UTC. This moisture advection was caused by the westerly winds at the top of the LLJ. The 00 UTC RAP forecast suggested the tilted boundary layer caused by the sloped terrain and uneven depth of the boundary layer across the slope allowed for the moisture in western Kansas to be advected above the capping inversion in eastern Kansas causing this layer to become unstable. The area where the moisture was advected to was on the eastern edge of the LLJ. Heterogeneity across the jet axis resulted in increased convergence in this region as the LLJ veered with time. This convergence would produce rising motion in this region which, when combined with the moisture advection, caused the CI.

The largest remaining unknown with this event is the role of the numerous outflows and bores that were present on this night. The effect of these features cannot be completely dismissed. In fact, a bore likely played a key role in initiating the first episode of convection in central Kansas, but since the RAP model was able to forecast the CI on this night, particularly the second CI episode, it is unlikely that a small scale feature that cannot be resolved in a 13 km model was the sole cause of the CI on this

night. Even if the outflow and bores were necessary for the convection to occur, the LLJ was responsible for modifying the environment that the outflows and bores propagated through, which enabled convection to develop. Without the top of the LLJ advecting moisture eastward, essentially priming regions for convection, the outflow and bores could not have produced convection by themselves. If the bore itself was forcing convection, then the CI would be expected to occur parallel to the bore, but on this night the CI that developed was oriented with a component normal to the bore. This strongly suggests that these CI events occurred in primed regions of the LLJ caused by heterogeneities in the LLJ structure.

2.2. 1 June 2015

After analysis of the 2 June 2015 CI event, it was discovered that a similar event occurred on the previous night. Many of the same features as those present on 2 June 2015 were also present on 1 June 2015.

2.2.1. Radar Overview of CI Event

Similar to 2 June 2015, radar indicated that at 00 UTC there was convection in eastern Colorado and a larger cluster of storms located along the Colorado/Kansas border (Fig. 22a). Over the rest of the PECAN domain, no storms were present. Four hours later, the convection in eastern Colorado had dissipated. The cluster of thunderstorms that was on the Colorado/Kansas border had organized into a southwest to northeast oriented line of storms and was moving south-southwest into southwestern Kansas and the Oklahoma panhandle (Fig. 22b). At 08 UTC, the line of

thunderstorms in the Oklahoma panhandle had weakened to mostly stratiform precipitation. It was at this time that CI occurred in a north-south line in central Kansas, just to the east of FP-3 (Fig. 22c). The convection drifted toward the southeast, but never became organized. By 12 UTC the convection has moved away from the initiation area and had mostly dissipated (Fig. 22d). A few small cells appeared to initiate behind the remnants of the original convection, but these cells were short lived.

2.2.2. Synoptic Conditions

The RAP analysis was again used to analyze the synoptic-scale features that occurred on 1 June 2015.

At 00 UTC a 250 hPa cutoff low was located on the Oklahoma/Arkansas border (Fig. 23a). The associated trough had a slight positive tilt extending down through Texas. There was a strong ridge over the western US, which extended up into Canada. West of the ridge there was a negatively tilted trough off the coast of California. The overall pattern resembled a weak omega block. The winds over the PECAN domain were 40 kts out of the northwest. At 500 hPa, the trough was broader and did not have the same positive tilt as the 250 hPa trough (Fig. 23b). In general, the overall pattern was not as amplified at this height. The flow over the PECAN domain was 25 kts out of the northwest. Just like on 2 June 2015, the upper levels were not particularly favorable for convection. At 700 hPa, the region where the cutoff low was located was more of an open wave (Fig. 23c). There was little to note at this level; the winds over the PECAN domain are rather weak and there was a small perturbation in

geopotential height on the Kansas/Nebraska border, which caused a small response in the wind direction in the area. At 850 hPa, there was little evidence of the upper level trough (Fig. 23d). Winds at the location where the upper level trough was located were weak and variable. In western Kansas, there was a stronger area of southerly winds. As on 2 June 2015, this line of southerly winds extended up into Canada. The winds in eastern Kansas were light and variable creating a stark contrast across the state. The area of strongest winds was occurring where the terrain slopes were the greatest suggesting that the slope might have been important for causing southerly winds at this height. There was an east-west moisture gradient present across Kansas, albeit this gradient was not as pronounced as on 2 June 2015 (Fig. 24). There was a temperature gradient located in the western part of the state, but as discussed in Section 2.1.2., a temperature gradient is to be expected at 00 UTC at 850 hPa over the Great Plains due to the intersection of that isobaric surface with the sloped terrain. At the surface, there was a rather diffuse temperature gradient across Kansas with a 6°C temperature difference between western and eastern Kansas (Fig. 24). The moisture at the surface is largely confined to the Colorado/Kansas border. The winds are quite varied across Kansas they are easterly in eastern Kansas, but a southerly component is present toward the western part of the state, with the winds in far western Kansas being south-southwesterly. Unsurprisingly, the 00 UTC conditions on 1 June 2015 were quite similar to the conditions on 2 June 2015.

There was very little change in the 250 hPa and 500 hPa levels at 12 UTC (Fig. 25a,b). The prevailing pattern had translated slightly to the east. The RAP analysis did not consider the 500 hPa trough to have a closed circulation at this time. The winds

over Kansas remained northwesterly at both levels and there was not much change in wind speed. At 700 hPa, again, there was minimal change (Fig. 25c). The winds over the PECAN domain weakened and the perturbation in the geopotential height that was on the Kansas/Nebraska border moved northeast. The most notable change at this level was a new wind maximum over central Arizona. Due to this feature's distance from the CI area it was likely unassociated with CI on this night. At 850 hPa, the LLJ extended from the Texas panhandle up into Canada (Fig. 25d), and a relative maximum in the LLJ is located in western Kansas. The winds inside the LLJ had clearly veered throughout the night, and the temperature gradient in western Kansas associated with the sloped terrain relaxed (Fig. 26). Slight eastward moisture advection occurred and the eastern side of the LLJ was a strongly convergent region. These two features were also present on 2 June 2015 and, as previously discussed in Section 2.1., were crucial for the CI on that night. Lastly, at the surface, the narrow strip of enhanced moisture on the Colorado/Kansas border was no longer present (Fig. 26). The temperature field had become more uniform, indicating that western Kansas had cooled off more than eastern Kansas. The upslope flow also weakened, which was to be expected due to the nocturnal surface cooling.

2.2.3. PECAN Observations

The data availability for 2 June 2015 was poor for PECAN standards but the data availability for 1 June 2015 was even worse. 1 June 2015 was the first official night of the PECAN field campaign, so not all of the instruments were available on this night. In addition, there was no IOP on this night, and thus no coordinated

soundings were conducted at the FP sites. Also, due to the narrow LLJ region on this night, the FP sites are not able to capture the spatial structure of the jet as well as 2 June 2015, since the edge of the LLJ was near FP-3. One benefit of this, however, is that the processes that occur on the edge of the LLJ were better observed for this case. Despite the less than ideal density of observations, the upper air wind data from FP-5 and FP-3 provide a glimpse of the LLJ structure and the CI mechanism.

The 915 MHz wind profiler at FP-5 shows a quick developing LLJ (Fig. 27) that has a wind direction that is veering with height, which is similar to the 2 June 2015 LLJ. The LLJ reaches peak intensity around 03 UTC. After this time the LLJ weakens and becomes shallower, but the veering with height wind direction is still present. At FP-3, the Doppler wind lidar shows that the LLJ develops much more slowly (Fig. 28). The LLJ doesn't really start to develop until 04 UTC, and even then the LLJ remains very shallow until 08 UTC when a diagonal striation similar to the one on 2 June 2015 appears. After 10 UTC the LLJ begins to become shallower. The water vapor DIAL shows the depth of the moist layer increasing throughout the night at FP-3 (Fig. 29) This increasing moist layer depth was another key feature of the previously presented 2 June 2015 CI case.

The LLJ at FP-5 was initially deeper than at FP-3, and the winds at the top of the LLJ had an easterly component. The RAP analysis showed that moisture values were higher in the locations near FP-5. This deeper LLJ at FP-5 initially advects moisture eastward at the top of the LLJ, thereby increasing the depth of the moisture at FP-3. Also, the height difference in the LLJ at the two sites would cause convergence on the eastern flank of the LLJ. One might assume that after 03 UTC this eastward

moisture advection and convergence would no longer be present since the LLJ becomes shallower at FP-5 around this time, but this cannot be confirmed this since there are no observations in the ~160 km distance between FP-5 and FP-3. Also, observations at FP-3 suggest that this assumption would be incorrect. To understand why this would not be the case, one has to consider the nonlinear effects of the LLJ, specifically the $u(\partial u/\partial x)$ and $u(\partial v/\partial x)$ terms. Due to nonlinear effects, the deeper portion of the LLJ was advected eastward throughout the night. These non-linear effects would cause the LLJ at FP-5 to become shallower and weaken and there would eventually be an increase in the depth of the LLJ at FP-3. This can be thought of as the westerly winds inside of the LLJ advecting themselves eastward. In fact, this is seen at FP-3, as the diagonal striation in the Doppler lidar profile at 08 UTC is indicative of this occurring. This diagonal striation is expected with a veering with height LLJ. Initially, the top of the LLJ had a westerly component, but the middle of the LLJ is almost purely southerly. This would cause the top of the LLJ to advect itself eastward more quickly than the middle of the LLJ. As the jet matures, the wind direction veers with time, and eventually the middle of the LLJ will develop a westerly component and it will advect itself eastward as well. Therefore, the middle of the LLJ should arrive at the new eastward location after the top of the LLJ. This is also seen at FP-3 at 0900 UTC as the LLJ no longer appears to have a double jet structure. These diagonal striations were also seen at FP-3 on 2 June 2015, but they were not as defined as on 1 June 2015. This is due to FP-3 being on the true edge of the LLJ on 1 June 2015, so the LLJ advection can be clearly seen. On 2 June 2015, FP-3 was in the middle of the

LLJ, so uneven LLJ depth, rather than being on the edge of the LLJ, was responsible for the diagonal striation, making this striation noticeable at only the top of the LLJ.

The CI on this night occurred just to the east of FP-3 around 08 UTC. This further bolsters the hypothesis that the westerly winds at the top of the LLJ were causing convergence, as the CI developed to the east of FP-3 at the same time the diagonal striation appeared on the Doppler lidar at FP-3. This strongly suggests convergence was occurring to the east of the westerly winds in the deeper LLJ. This convergent region would slowly move eastward throughout the night along with the moisture being advected eastward by the top of the LLJ. The initiation of convection by this convergent region would depend on the convergence moving into a region where the upper level thermodynamic profile becomes more favorable for convection.

2.2.4. RAP Forecast

Since the 00 UTC RAP forecast provided insight into the CI mechanism on 2 June 2015, it was decided that the 00 UTC RAP forecast for 1 June 2015 would be used to further examine the evolution of the LLJ and CI mechanism. The 00 UTC RAP forecast on this night had an over amplified signal for CI in a north-south line extending from western Oklahoma up to central Nebraska (Fig. 30). Cross-sections were used to examine the horizontal structure of the LLJ to identify whether a similar mechanism to 2 June 2015 occurred on this night. Ideally these cross-sections would be taken near the FP-5/FP-3 line so they could be compared to observations, but this was not possible due to the RAP forecast predicting precipitation at that latitude too early. Therefore, the cross-sections had to be taken at a lower latitude.

The 00 UTC RAP forecast for 1 June 2015 is remarkably similar to the 00 UTC RAP forecast for 2 June 2015. At 00 UTC, the RAP forecasted for a tilted boundary layer which caused moisture in western Kansas to be at a greater height ASL then in the eastern part of the state (Fig. 31a). At 04 UTC a strongly veering with height LLJ had developed (Fig. 31b). The effect of the veering with height LLJ on the moisture field can already be seen at this time, as the top of the LLJ was beginning to advect moisture eastward. Convergence was clearly present on the eastern edge of the LLJ due to the westerly winds at the top of the LLJ. The advection of the LLJ winds can also be seen at this time near 99°W. At the surface there were moderately strong upslope winds. The winds weakened above this height, but then increased in strength and became westerly. By 08 UTC, the RAP was forecasting for the LLJ to become shallower and the convergence on the eastern edge had actually decreased, but was still present (Fig. 31c). Moisture had been advected further eastward and, like on 2 June 2015, the slightly slanted isentropes suggest isentropic ascent was possible at the top of the LLJ. However, this isentropic ascent would have been weaker than that which occurred on 2 June 2015 as the tilt of the isentropes is not as steep. Finally, at 12 UTC, the narrow LLJ has veered enough so all but the lowest levels have a westerly component (Fig. 31d). Convergence was still present at the top of the LLJ on the eastern edge, and the isentropes were more slanted, indicating stronger isentropic ascent by this time.

RAP forecast soundings at the CI area show a similar evolution as those from 2 June 2015. At 00 UTC, the profile is extremely stable with no CAPE (Fig. 32a). By 04 UTC, the veering with height LLJ was visible and moisture advection at 800 hPa was

beginning to occur (Fig. 32b). There is also an increase in temperature at 800 hPa indicating that parcels are not yet being lifted as they are advected eastward. At 08 UTC the temperature and moisture advection is still occurring, but the layer has not become closer to saturation (Fig 32c). Finally, at 12 UTC the 775 hPa layer is now saturated with no CIN (Fig. 32d). The increased isentropic ascent between 08 and 12 UTC likely contributed to the saturation of this layer in the forecast. The wind barbs at this saturated layer indicate that westerly winds had increased suggesting that increased convergence may have also have played a role.

2.2.5. Summary of Event

The CI event on 1 June 2015 was almost identical to the CI event on 2 June 2015. A north-south line of CI occurred in central Kansas on the eastern edge of a narrow LLJ. Observations on this night were limited, but upper air data showed that a veering with height LLJ developed quickly at FP-5. At FP-3, the LLJ was initially very shallow and slow developing. The stark difference in LLJ heights between FP-5 and FP-3 indicates that convergence was occurring at the top of the LLJ where the winds were westerly. These westerly winds were also advecting moisture eastward toward FP-3 as shown by the increased depth of the water vapor detected by the DIAL. After 04 UTC, the depth of the LLJ at FP-5 began to shrink. Four hours later at 08 UTC, the LLJ depth at FP-3 increased and CI occurred just to the east of the site. The change in LLJ height between the two sites is indicative of the LLJ advecting itself eastward with time. This eastward advection shifted the convergent region east of FP-3. The 00 UTC RAP forecast was consistent with observations that the veering

with height LLJ was advecting moisture eastward at the top of the LLJ and the convergent region east of the LLJ helped force the convection.

2.3. 5 July 2015

The last CI event considered in this study occurred on 5 July 2015. Like the 1 June 2015 CI event, this case was identified after the analysis of the 2 June 2015 CI event.

2.3.1. Radar Overview of CI Event

Just like the other two CI cases, there was convection in eastern Colorado at 00 UTC (Fig. 33a). At this time, there was also a small, rather intense storm located in the southwest corner of Kansas. At 04 UTC, only a few small weak storms remained in Colorado, and new CI was starting to occur in western Kansas, just west of Dodge City (Fig. 33b). This new CI was the beginning of a more vigorous north-south line of CI. By 08 UTC more CI occurred at this longitude, and the broken line of convection extended up to the Kansas/Nebraska border (Fig. 33c). This line of convection remained quasi-stationary, but slowly weakened until only a few remnant showers remained at 12 UTC (Fig. 33d). A weaker, sparser north-south line of CI developed just west of Topeka at that time. More cells developed after 12 UTC on this north/south line and persisted until 16 UTC, well after sunrise.

2.3.2. Synoptic Overview

Even though this event occurred over one month after the 1-2 June 2015 CI events, the synoptic pattern that occurred on this night was similar to those that occurred on the previously presented CI nights.

At 00 UTC at 250 hPa, a trough was located over the Mississippi Valley region (Fig. 34a). Though weaker than the 1-2 June 2015 trough, the location was nearly identical. A negatively tilted ridge was present over the western U.S. and there was a cut-off low off the coast of California. There was a weak jet streak (only 75 kts) with northwesterly winds over western Kansas. At 500 hPa, the trough over the Mississippi Valley was less defined but had a closed contour over western Tennessee (Fig. 34b). The trough had a clear positive tilt. There was also a shortwave with an axis that runs from eastern South Dakota down into eastern Kansas. The region of ascent associated with this shortwave would have been east of the PECAN domain. If anything, the shortwave would have been causing descent over central Kansas. The ridge over the western U.S. was not as strong at this height and the low off the coast of California was completely cut off from the main flow. The winds over western Kansas were weak out of the northwest while the winds in eastern Kansas were easterly. This wind shift across Kansas was caused by the shortwave. The flow at 700 hPa was mainly zonal over the continental U.S. There was no evidence of the upper level ridge over the western U.S. at this height (Fig. 34c). South of the region where the 500 hPa trough was located there was a region of enhanced wind speeds from southwest Oklahoma to off the coast of North Carolina. Of particular interest is the region of higher wind speeds in western Kansas. These winds were southwesterly, while the

winds of the rest of the state were west-northwesterly. The eastern edge of this wind speed maximum was the location where the first line of CI occurred on this night. At 850 hPa, there was a southerly wind speed maximum that extended from Kansas up into Canada (Fig 34d). The winds over the Mississippi Valley were weak and variable. This 850 hPa pattern was found on the other two CI nights, as well. The typical 850 hPa afternoon temperature gradient was present over Kansas (Fig. 35). There was also a diffuse moisture gradient over northeast Kansas, but this gradient was not as defined as the other two cases. At the surface, there was an unorganized temperature gradient from east-to-west across Kansas (Fig. 35). There was no clear moisture gradient at the surface. In western Kansas, there was a small region of higher moisture located in the same region as where the CI occurred on this night. After looking at the RAP analyzed composite reflectivity, it was found that this region of enhanced moisture was associated with an incorrectly analyzed region of precipitation (not shown). Therefore, it is unlikely that this enhanced moisture region was analyzed correctly.

Like the other two cases, not much has changed in the upper levels between 00 and 12 UTC. At 250 hPa, the trough over the Mississippi Valley became disjointed with the northern portions of the trough developing a negative tilt while the other portions acquired a more positive tilt (Fig. 36a). The ridge the western U.S developed a more neutral tilt and increased in strength. The winds over Kansas became more westerly, and the weak jet streak had moved south into Oklahoma. At 500 hPa, the trough became more defined, while the shortwave that was on the eastern edge of the domain propagated southeast (Fig. 36b). The winds over Kansas at this height became more westerly. Overall, like the other two CI events, nothing at the upper levels would

have caused the CI that occurred on this night. There was not much to note at 700 hPa (Fig. 36c). The wind maximum that was in western Kansas was no longer present, and the winds over the state were weak and westerly. At 850 hPa, an LLJ can be seen extending from the Gulf of Mexico into Canada (Fig. 36d). This LLJ had two maximum regions: one near Brownsville, TX and the other in southwest Kansas. While the map shows a continuous LLJ up to Canada, this LLJ was likely two separate LLJ that were formed by different mechanisms. This double maximum LLJ has been identified and discussed by Walters et al. (2008). The temperature gradient over Kansas at 850 hPa weakened (Fig. 37) and there was a gap in the moisture field near the eastern edge of the LLJ. As mentioned earlier, the RAP had difficulties analyzing the moisture field for this night so it is unknown if this moisture gap actually occurred. There did appear to be convergence on the eastern edge of this LLJ. Lastly, at the surface there was very little change (Fig. 37). The temperature over Kansas had decreased and became more uniform, and the surface winds had a weaker upslope component. Northward moisture advection had caused the nose of moisture to move into south-central Kansas.

2.3.3. PECAN Observations

The CI case on 5 July 2015 is the most well-sampled CI event that will be presented, but the initiation mechanism is the most difficult to infer. There was an IOP on this night, but it was focused on bores near North Platte, NE with mobile observations beginning at 02 UTC. Due to the slower than expected development of the MCS and resulting bore, the IOP ended at 0415 UTC. Like on 2 June 2015, these

mobile observations were not particularly useful for analysis of this case due to the deployment location, strategy, and short time duration. The FPs on this night launched radiosondes at 00, 03, and 06 UTC except for FP6 which launched at 03, 0430, and 06 UTC. Some of the radiosonde launches at the FP sites were slightly delayed, but no launch occurred more than 20 minutes after the designated time. The north/south orientation of the two lines of CI on this night suggests that horizontal heterogeneities across the LLJ axis were important, so the conditions at the FPs were compared to attempt to identify these heterogeneities and evaluate how they effected the CI.

The 915 MHz wind profiler at FP-5 shows that a strong, veering with height LLJ developed on this night (Fig. 38). This LLJ was much deeper than the LLJs that occurred on 1-2 June 2015 as this LLJ had wind speeds of 20 ms^{-1} up to 1.5 km a.g.l. After 06 UTC the LLJ at this location began to become shallower like on 1 June 2015, but still maintained its veering with height structure. The soundings from this site indicate that there was a large amount of CAPE (over 3000 J) present at this location, but there was a sturdy cap. This cap increased substantially throughout the night with most unstable CIN increasing to over 309.9 J by 0600 UTC (Fig. 39). This region was rather unfavorable for convection, particularly later in the night.

At FP-2 the environment was quite different than at FP-5. The Doppler lidar at this site shows that the LLJ developed more slowly at this location (Fig. 40), as the LLJ does not begin to intensify until 0600 UTC, after which it continued to steadily increase in strength. The environment at FP-2 was quite unstable at 00 UTC with only -9.0 J of CIN for a surface based parcel (Fig. 41). Between 00 and 03 UTC, the most unstable parcel became elevated and CIN actually decreased to -4.2 J. This decrease in

CIN was due to a very slight increase in moisture (on the order of 1 g kg^{-1}). This moisture increase occurred throughout the entire depth of the boundary layer, so it does not appear to be caused by zonal moisture advection. At 06 UTC, the most unstable CIN increased due to lower levels drying out. The increase in instability at 03 UTC corresponds to the CI that occurred around 04 UTC just to the west of FP-2.

The lidar at FP-3 shows a similar evolution of the LLJ as seen at FP-2 (Fig. 42). The LLJ at FP-3 was initially shallow and slow developing. Near 06 UTC the LLJ began to strengthen. While not as clear as on 1 June 2015, the non-linear effects of the LLJ can be seen at 06 UTC, as the start of a diagonal striation of enhanced wind speeds occurred near 1.5 km. There was a relative minimum in the LLJ between 0.5 km and 1.5 km at this time. This relative minimum began to fill in and by 0730 UTC the jet wind speeds were more continuous. Interestingly, the north/south line of CI expanded toward the north at 07 UTC. This northward extension occurred 50 km to the west of FP-3. The timing of the CI and increased depth of the LLJ is consistent with a convergent region at the top of the LLJ moving slowly through the region. The wind profiles from the radiosondes confirm convergence was likely occurring between these two sites, particularly at 06 UTC (Fig. 43). At that time, there was a clear maximum in the u component of the wind at FP-5 that was approximately 5 ms^{-1} greater than the u component of the wind at a similar height at FP-3. This convergence likely caused the first north/south line of CI on this night.

CI did not occur at FP-3 on this night even though the convergent region likely passed over the site. This was because the thermodynamic environment at FP-3 was initially stable and became more stable as the night progressed (Fig. 44). At 00 UTC,

the surface based parcel was moderately capped. By 03 UTC, the most-unstable parcel had become elevated, but CIN increased, and at 06 UTC the most unstable parcel still had ample CIN to prevent convection. The water vapor DIAL shows that the depth of the high water vapor values actually decreased slightly before a layer of lower water vapor values that extended to greater heights moved in at 06 UTC (Fig. 45). Since there was no moisture advection to increase instability this region remained unfavorable for convection and the slight rising motion caused by the convergence was unable to overcome this stability.

Unfortunately, there are no observations between FP-5 and FP-3 to identify why the regions between the two FP sites was favorable for convection. Since CI occurred in that region, the conditions were obviously more conducive for CI, but it is unknown if this favorable environment is due to dynamical effects, such as stronger convergence or a more favorable thermodynamic environment. The moisture variability between FP-5, FP-3, and FP-2 suggests that the moisture distribution on this night was complex (Fig. 45), and that smaller scale moisture advection was likely playing a role in the CI. This is unlike 1-2 June 2015 where the moisture advection was of a larger scale and could be easily identified by the FPs. This smaller scale moisture advection is not able to be adequately observed by the coarsely spaced FP sites. It is plausible that the region between FP-5 and FP-3 had a thermodynamic profile that was closer to that of FP-2, where the convergence produced at the top of the LLJ would be able to initiate convection.

There was also a second region of CI that occurred around sunrise just east of FP-6. The Doppler lidar at FP-6 indicated that this area was closer to the true eastern

boundary of the LLJ on this night (Fig. 46). The LLJ at this location was weaker than the LLJ at the other FP sites throughout the night. Close to 11 UTC the LLJ actually began to increase in strength. This is unusual since at 11 UTC one would expect the LLJ wind speeds to begin to decrease. This increase in wind speeds actually occurred from the top down, and the winds developed a more westerly component. This is similar to what occurred earlier in the night at FP-3, but at a lower height. This increase in wind speeds suggests that a convergent region on the eastern edge of the LLJ passed over the site. Shortly after this increase in wind speeds at FP-6 the CI occurred east of the site.

2.3.4. RAP Forecast

The 00 UTC RAP forecast for 5 July 2015 was used to further analyze the LLJ on this night. The RAP did not have a good handle on the CI on this night as it was predicting too much precipitation in central Kansas after 06 UTC. The model did briefly predict two small cells of precipitation in the general area of the first CI location (Fig. 47). Like the analysis of the other two CI events, cross-sections across Kansas were used to examine the horizontal structure of the forecasted LLJ.

The first feature to note on the 00 UTC cross-section was the large change in boundary layer depth across the state (Fig. 48a). This non-uniform boundary layer height was crucial for the development of convergent regions at the top eastern edge of the LLJ. Essentially, a deeper boundary layer results in a deeper LLJ, so if the boundary layer heights are variable across the state, then the LLJ depth should also be variable. This effect is discussed in greater detail in Chapter 4. At 04 UTC, the RAP

had forecasted for a very deep, strongly veering with height LLJ in western Kansas where boundary layer depth was greatest (Fig. 48b). This resulted in strong convergence at the top of the eastern edge of this deep portion of the LLJ. The non-linear LLJ transport can be seen at this time at approximately 100°W. There was a clear break in the LLJ wind speeds in this profile due to the top of the LLJ moving eastward faster than the middle layers. Notice that where this convergence was occurring there was minimal moisture, which was likely why there are only two small regions of precipitation forecasted with this convergence. By 08 UTC, the depth of the LLJ had decreased, but there was still convergence at the top of the LLJ (Fig. 48c). The isentropes had a steep tilt, indicating that isentropic ascent could occur with the westerly winds in the LLJ. The lowest levels of the LLJ had intensified toward the east. Lastly, at 12 UTC, the LLJ had shifted toward the east and the wind direction was mostly out of the southwest (Fig. 49d). The forecast shows an elevated moisture plume which appears to be associated with the isentropic ascent in the deep portion of the LLJ. Ultimately, this RAP forecast helps confirm that the CI that occurred between FP-5 and FP-3 was caused by convergence at the top of the LLJ. The forecast cannot, however, clarify the cause of the second region of CI east of FP-6.

2.3.5. Summary of Event

On 5 July 2015, two north-south lines of CI occurred in Kansas. The first, more robust line of CI occurred in western Kansas around 04 UTC with new cells occurring until 06 UTC. The second line of CI had sparse coverage and occurred in eastern Kansas around sunrise. The synoptic conditions on this night were similar to

the other two CI cases that were present previously, and there was little large scale support for convection on this night. Observations revealed that there was a complex moisture field over Kansas which the FP sites could not resolve with enough detail to determine if moisture advection was important for CI on this night. Wind data from the western FP sites suggested that a LLJ with a non-uniform depth developed and caused convergence that produced the first north-south line of CI. These observations were backed up by the 00 UTC RAP forecast, which predicted a similar non-uniform LLJ and convergence. The second line of CI in eastern Kansas was also most likely caused by a convergent region of the LLJ. This is evidenced by the lidar data at FP-6 , which showed a small increase in depth and intensity of the LLJ at a time when the LLJ should be weakening. Shortly after this occurred, CI developed east of the FP site. While this case had some differences from the two previously presented CI cases, the primary mechanism for the CI is the same. East-west heterogeneities in a veering with height LLJ created convergence at the top of the LLJ due to the westerly winds in western Kansas occurring above the LLJ further east. This convergence provided the lift to cause the CI on this night.

Chapter 3: WRF Simulations of Convection Initiation Events

3.1. Background and Model Set-Up

The PECAN observations and the RAP forecasts revealed that differential moisture advection and convergence caused by heterogeneous, veering with height LLJs produced the north-south lines of convection on the nights of 1-2 June 2015 and 5 July 2015. Even though the overall processes leading to the CI were able to be determined using these products, there are details that were not able to be explained with exclusively the PECAN observations and RAP forecasts. Specifically, it is unknown where the parcels that caused the CI originated from and how they were moving through the LLJ on these nights. Were the parcels constantly rising throughout the night or was the rising motion only occurring near the CI region? Having trajectories of the air parcels that feed into the CI area would help diagnose the source region for CI, the movement of the air parcels, and the processes by which these parcels become saturated.

Due to the RAP forecasts being a convective parameterized model with output only every hour, it was deemed unfit for a trajectory analysis. Therefore, the three CI events were modeled using the Weather Research and Forecasting (WRF) model to conduct a back-trajectory analysis of these CI events. An additional benefit of modeling these events with the WRF model is the opportunity to assess the sensitivity of the CI. LLJs modeled by WRF previously were found to be highly dependent on the boundary layer scheme (Storm et al. 2009). Since the LLJ is crucial for the development of CI on these nights, the CI would also be expected to be sensitive to the boundary layer scheme. A lack of CI sensitivity to the boundary layer scheme could

suggest that these CI events are not as strongly dependent on the LLJ as the PECAN observations show.

For these simulations, version 3.8.1 of the Advanced Research WRF was used (Skamarock et al. 2008). The model was run with 4 km grid spacing on a 512x512 horizontal grid with 70 stretched vertical levels. The number of vertical levels was set above the default of 50 so more levels would fall inside the boundary layer to resolve the LLJ. The Global Forecasting System (GFS) analysis was used to initialize the model and update the boundary conditions every six hours. Each model run had a 12-hour spin-up with 10 second time stepping. For radiation, the Rapid Radiative Transfer was used for longwave radiation and the Dudhia scheme was used for shortwave radiation. The PBL schemes used were the Yonsei University scheme (YSU; Hong et al. 2006), the Mellor-Yomada-Janjic scheme (MYJ; Janjic 1990; 1994), the Quasi-Normal Scale Elimination PBL (QNSE; Sukoriansky et al. 2005), and the Mellor-Yamada-Nakanishi and Niino PBL (MYNN; Nakanishi and Niino 2004). Three schemes - MYJ, QNSE, and MYNN - are local PBL schemes, while YSU is a non-local scheme.

Only 2 June 2015 and 5 July 2015 were chosen for the PBL sensitivity test because they represent two separate synoptic environments for the CI cases. There were very few 1 June 2015 observations to compare the model runs to, so the sensitivity tests were not conducted for that case. The performance of the PBL schemes was evaluated on two criteria: the representation of the LLJ and the accuracy of the timing and placement of the CI. From this evaluation, one PBL was chosen for the WRF model runs for the back-trajectory analysis for the three CI cases.

3.2. PBL Sensitivity Tests

3.2.1. 2 June 2015

A comparison of the 1 km simulated reflectivity between the four model runs with different PBL schemes for 2 June 2015 is shown in Figs 49-53, and the actual reflectivity can be seen in Fig. 3. All models at 00 UTC have weak popcorn-like reflectivity areas in the eastern part of the domain. These small reflectivity values disappear quickly in all model runs after 00 UTC. All four runs are showing convection in the western Oklahoma panhandle. This convection is occurring slightly north and east of where it actually occurred in all model runs - and no model run has the more organized line of convection that occurred in the Nebraska panhandle at 00 UTC - but all show signs of convection beginning to develop at that location. At 04 UTC, all model runs have convection along the Colorado/Kansas/Nebraska border which extends further to the south than what radar indicates. This convection is moving almost purely easterly, which deviates from what actually occurred as the MCS on this night moved toward the southeast on this night. The discrepancy in storm motion may be due to the southward propagating bore on this night. The bore would have focused redevelopment of the MCS on its southern periphery, giving the MCS propagation a southerly component. The bore cannot be resolved in the 4 km WRF runs so the southerly propagation never occurs in the model. For the convection in the Texas panhandle, the YSU and MYNN model runs correctly have the convection moving to the southeast and weakening. QNSE and MYJ, however, overdevelop this convection and move it too far east. At 08 UTC, all of the model runs no longer have

an MCS in Nebraska and not even a stratiform region remains. These model runs likely cannot resolve the remaining stratiform region due to the simple microphysics scheme used for the model runs. If the MCS is to be more accurately resolved, then a more complex scheme that includes graupel would need to be used. All of the model runs show an area of low reflectivity in eastern Kansas. Both MYNN and YSU model runs seems to have the best handle on the convection at this time, while the MYJ and QNSE model runs have overdeveloped the convection. Finally, at 12 UTC, all models have a north-south line of convection. The convection in the models is overdone and the maximum in intensity is too far to the south. MYJ and QNSE both have a significant amount of noisy reflectivity regions to the west of the line of convection, while YSU and MYNN have less of the noisy regions. Overall, YSU and MYNN are superior for modeling the convection on this night with YSU slightly beating out MYNN.

The ability of the WRF runs to model the LLJ was assessed using the 03 UTC soundings from FP-3, FP-2, and FP-6. These sites were chosen because at that time they were unaffected by convection in both the model and in actuality. The soundings are also able to show how accurately the thermodynamic environment was modeled by the WRF model

At FP-2, the inaccuracy of all the model runs' water vapor profiles immediately stands out (Fig. 53). The model runs are too moist at this site with QNSE being the worst with a 2 g kg^{-1} error. The models also do not represent the surface inversion accurately and the capping inversion is too strong. Every model run has the maximum v-component of the LLJ at a height above that which occurred, and QNSE,

MYJ, and YSU all have too strong of a v-component maximum. For the u-component, all model runs overestimate the upslope winds near the surface with MYNN being the worst. The westerly wind maximum at the top of the LLJ is above that of the observed maximum for both the MYNN and YSU model runs. No model runs were able to represent the sharpness of the westerly wind maximum at the top of the LLJ.

Many of the problems at FP-2 are also present at FP-3. All of the models have overestimated moisture at lower levels, and are not accurately modeling the surface inversions (Fig. 54). The v-component of the wind is stronger than observed in all model runs at this location, with the QNSE model run being the worst offender. The upslope wind near the surface is better resolved at FP-3 than at FP-2, but the models diverge when resolving the westerly wind maximum at the top of the LLJ. The MYNN and YSU model runs have similar u-component profiles and have the height of the westerly maximum too high, and over-amplified. The MYJ and QNSE models runs have similar profiles to each other and they correctly predict the intensity and height of the maximum.

Finally, at FP-6, low-level moisture is again overestimated and the strong capping inversion at this location is completely smoothed over by all model runs (Fig. 55). The v-component maximum intensity is more accurately represented at this location, but the depth of the maximum is greater than observed. Again, both the MYNN and YSU model runs have similar u-component profiles, but the westerly wind maximum is stronger than what actually occurred. QNSE and MYJ model runs more accurately resolve the less peaked nature of the westerly wind maximum.

In summary, all WRF model runs on this night resolved a north-south line of convection in eastern Kansas in the early morning. The line of convection was overdone in all models, but was most accurately modeled by the YSU model run. The best model run for resolving the correct LLJ structure and thermodynamic environment was not as clear cut. All model runs had too much moisture in the low-levels at all FP locations examined. Capping inversions were also poorly handled by all models. The QNSE model run was the worst at predicting the LLJ intensity as it overestimated the intensity of the LLJ at all locations. Both MYNN and YSU were better at modeling the intensity of the LLJ, but the jets were too deep and the westerly wind maximum at the top of the LLJ tended to be stronger and sometimes higher than what was actually observed. This result created a complex problem for choosing a PBL scheme for the trajectory analysis. The MYNN and YSU model runs were the most accurate at predicting the convection, but overestimated what can be considered the most critical feature of the LLJ for forcing the north-south lines of convection. This result can be explained by the moisture values. The MYNN and YSU runs had the lowest values of moisture even though it was overestimated. Since the CI on this night was dependent on parcels reaching saturation before initiation, these lower moisture values caused less CI to occur and also caused it to occur later. The depth of the moisture is also important. The maximum westerly wind in the MYNN and YSU model runs occurred above the low-level moisture, and therefore, the errors in the maximum westerly winds only produced a minimal increase in the eastward moisture advection at the top of the LLJ. Another factor to consider is the limited temporal verification of the modeled LLJ. The 03 UTC sounding provides verification at a point

in time, but how the models performed after this time cannot be determined by using soundings as a verification source.

3.2.2. 5 July 2015

The WRF model runs for 5 July 2015 were not as successful as the runs for 2 June 2015 at modeling the convection. For reference, Fig. 33 shows the observed reflectivity on this night. At 00 UTC, all models correctly show a storm in the southwest corner of Kansas, and convection that was present in Oklahoma and Arkansas at this time was also predicted by the model runs (Fig. 56). The YSU and MYNN runs appear to have low precipitation supercells in western Nebraska. YSU has two such storms while MYNN has one. The QNSE and MYJ runs also have some convection in this region, but the convection does not have the characteristic shape of a modeled supercell. The storms present at this location in all of the model runs do not verify. All of the convection that actually occurred at this time and latitude occurred further to the west. By 04 UTC, the YSU and MYNN storms have moved south, grown larger, and intensified (Fig. 57). The storms on the QNSE and MYJ runs also have intensified, but have not yet moved into Kansas. All of these storms produced by the model runs failed to occur on this night. These modeled storms persisted and strengthened along the same north-south line where the CI actually occurred on this night. The storms that were incorrectly present at 00 UTC, may have further developed due to the increased elevated convergence along this north-south line. At 08 UTC, the storms in western Kansas weaken in all model runs. Except for QNSE, the location of the remaining precipitation matches up well with the location of the actual

CI on this night (Fig. 58). All four model runs are beginning to develop a north-south line of CI in eastern Kansas. The line is most developed in the MYJ model run, while it is least developed in the YSU run. As mentioned in Chapter 2, a weak north-south line of CI did occur on this night at this location but it occurred closer to 12 UTC. By 12 UTC, YSU, MYJ, and MYNN all had a more developed north-south line of convection (Fig. 59). QNSE has a cluster of storms of storms in southeast Nebraska, but it is not a full line like in the other three model runs. Similar to 2 June 2015, the two PBL schemes that produced the best CI results were YSU and MYNN.

For the evaluation of the LLJ on this night, soundings are again used from FP-2, FP-3, and FP-6, but this time there are multiple soundings at each location. At FP-2 and FP-3 there are soundings at 00 UTC, 03 UTC and 06 UTC, while at FP-6 the soundings are at 03 UTC, 0430 UTC, and 06 UTC.

At 00 UTC at FP-2, the model runs all appear to have a mixed layer which is overdeveloped. The v-component of the wind is much stronger than what was observed above 2 km ASL, and the westerly wind maximum also occurs too high. The QNSE run is an outlier at this time as it had already begun to develop the LLJ. This can be seen by the increased v-component of the wind above 2 km ASL and the stronger upslope component near the surface. In terms of moisture, all of the models are drier than observed below 2.5 km ASL, but are too moist above that height. The potential temperature profiles show that the boundary layer is slightly warmer then observed in the first kilometer, but becomes cooler than observed above the capping inversion due to the mixed-layer being too deep. At 03 UTC at FP-2, the model runs begin to further deviate from observations (Fig. 60). All model runs are dramatically

underestimating moisture in the boundary layer and the boundary layer is warmer then observed. The v-component wind profile, while being the correct shape, is systematically 3-4 m s^{-1} stronger then the v-component measured by the radiosonde. The low-level upslope wind is modeled reasonably well, but the westerly wind maximum at the top of the developing LLJ is too strong. The MYNN model run is particularly troublesome as the maximum occurs 500 m above that of the westerly wind maximum in the other model runs. The moisture above 3 km ASL is also vastly overestimated in the MYNN model run at this time. By 06 UTC many of the same problems are present. The boundary layer is still drier than the observed sounding and the LLJ is too strong above the low-level v-component wind maximum. The model runs seem to diverge the most regarding the westerly wind maximum. This maximum is still higher in the MYNN run than the other models. YSU, however, has a slight negative bias in the u-component profile up to 3 km ASL, but above that height westerly winds become stronger than observed. The moisture associated with these anomalously strong westerly winds in the YSU model run is much greater than the moisture measured by the radiosonde.

At FP-3, the LLJ also tended to be overestimated by all model runs (Fig. 61). At 00 UTC, the v-component wind profiles are systematically biased toward stronger winds, and the u-component wind profile also has the westerly wind maximum above that which was observed and is too strong. The QNSE model run is developing the LLJ early at this location as well. In stark contrast to FP-2, all of the model runs overestimated the boundary layer moisture at FP-3. By 03 UTC, the modeled LLJ is much stronger than what was observed and all model runs significantly overestimated

the moisture above the boundary layer height. The MYNN model run actually has the weakest v-component maximum, but has the deepest LLJ. This is causing large errors in the v-component wind profile. The MYNN run also predicts the westerly maximum wind being a full kilometer higher than the observed maximum. At 06 UTC, convection in the model has contaminated the profiles so no comparisons can be made to the observed soundings

At FP-6 at 03 UTC all of the model runs have reasonable skill at resolving the v-component wind profile (Fig. 62). The low-level upslope flow and the westerly wind maximum are a little too amplified, but the problems are not nearly as bad as at the other two FP sites. All of the model runs struggled with the thermodynamic environment at this location. The problems stem from the model runs being unable to accurately model a correct boundary layer. At 0430 UTC, the models mostly underestimate the v-component of the wind but continue to over-amplify the u-component. The potential temperature profiles show that the well-mixed boundary layer is still too deep, which is causing elevated moisture values that are much larger than observed. At 06 UTC, the sharpness of the v-component wind profile is not resolved by any of the model runs and the u-component profile remains over-amplified. The mid-level moisture continues to be a problem, but the bulge in the moisture profile seen at low levels in observations is actually resolved. The YSU model run in particular seems to handle this feature the best.

Overall, the sensitivity test for this night can be considered disappointing, but informative. All models struggled to accurately forecast the convection that occurred on this night since they overproduced convection earlier in the run which ruined the

environments. Even though the forecasts were unimpressive, YSU and MYNN did the best at forecasting for the convection. For modeling the LLJ, however, all PBL schemes seemed to have a problem. QNSE caused the LLJ to develop to early, MYJ caused the LLJ to be too strong, and YSU and MYNN caused the LLJ to be too deep. The MYNN scheme, particularly, had a problem with the westerly wind maximum at heights much higher than observed. As mentioned in the previous section, the incorrect modeling of the westerly wind maximum is quite troublesome due to its role in causing the CI in these events. The model runs seemed to struggle the most with an accurate portrayal of the boundary layer as evidenced by the potential temperature and moisture profiles. The weak capping inversion on this day may have wreaked havoc on the PBL schemes. Without a well-defined cap, the PBL schemes could have over mixed, causing the boundary layer to be inaccurately modeled.

3.2.3. Discussion

Following the sensitivity tests, it was decided that the YSU PBL scheme would be used for the WRF trajectory analysis. Ultimately, the decision came down to YSU and MYNN, due to their increased skill over the other two schemes at forecasting the CI on these nights. YSU was chosen over MYNN mostly due to the poor performance of the MYNN run at modeling the LLJ on 5 July 2015. The large errors in the westerly wind at the top of the LLJ were deemed too troublesome to use MYNN, especially since the feature is key in producing these CI events.

The sensitivity test also provided some insight into possible reasons why the operational models over forecasted the the CI on these nights. In the WRF runs,

moisture values were found to be 1-2 g kg^{-1} larger than those observed in the boundary layer on these nights, and for the 5 July 2015 case, moisture values were also too large above the boundary layer. The CI mechanism on these nights depends on the parcels becoming saturated before the CI is initiated due to the relatively weak lift. If moisture is biased too high in operational models, more CI would be expected, since saturation can be achieved more easily. Another problem in the WRF runs was inaccurate modeling the of the top of the LLJ. Some boundary layer schemes caused the westerly winds at the top of the LLJ to be higher and stronger than what was observed. This issue was also seen in the 00 UTC RAP forecasts. These higher and stronger winds could lead to both stronger moisture advection and stronger convergence, which could lead to more CI in the models. While two cases is a limited sample to draw model bias conclusions, these factors need to be considered when using NWP to predict these CI events. Improvements in forecasting these CI events can be expected with improvements in PBL schemes and assimilating moisture observations.

3.3. WRF Back-Trajectory Analysis

The WRF back-trajectory analysis was completed using the Read/Interpolate/Plot (RIP) version 4.5 post-processing tool. The output that the WRF trajectories were calculated from had a 15-minute time interval, while the trajectories were output every 5 minutes through interpolation. For each case, multiple back-trajectories originating from different heights were calculated from a point in the line of CI. This allowed for differences in parcel motion with height to be evaluated. The

parcels' relative humidity was calculated along the trajectories to diagnose the saturation of the parcel, since saturation was important for these CI events.

The trajectories for 2 June 2015 are shown in Fig. 63. As expected, the parcels at higher altitudes traveled a greater distance toward the east. The source region for the parcels at the top of the LLJ was western Oklahoma, while the lowest parcel traveled from western Missouri to the CI region. In terms of parcel path, the back-trajectories from the WRF model agree with expectations of a veering with height LLJ. The trajectories also indicate that very subtle mean rising motion was occurring in the upper regions of the LLJ for most of the night. This rising motion was most persistent once the parcel motion acquired a greater eastward component. This result is consistent with the isentropic ascent that the RAP model indicated could possibly occur with a westerly wind. This rising motion is not very significant in terms of strength, as the greatest vertical gain by a parcels was ~700 m. Over 12 hours this indicates that the parcel would have been rising at a mean rate of 1.62 cm s^{-1}. This weak lift did, however, have a significant impact on the saturation of the parcels. The previously mentioned parcel's RH went from 57% at 00 UTC to 95% at 12 UTC. Not all parcels experienced the same change in saturation. The parcels that originated at higher elevations were initially closer to saturation so they did not have to rise as much to become saturated. This caused all trajectories at the top of the LLJ to be saturated or close to saturated by 12 UTC. The saturation of low-level parcels also increases throughout the night. This increase would be due mostly to radiative cooling near the surface, so even though these parcels are saturated they are quite stable. The saturated upper level parcels, however, would be unstable if they were lifted above the

stable capping inversion, which was shown to be occurring in both observations and the RAP model on this night.

The trajectories for 1 June 2015 look similar to those on 2 June 2015 (Fig. 64). It should be noted, however, that the WRF model only produced CI near a previously developed convective storm which complicates the analysis of these trajectories. Ideally, these trajectories should have been calculated at a point further north from the original storm, but the model did not produce CI there, even though it actually did occur in that region. The trajectories that started further to the west were likely influenced by the original storm. Unfortunately, these are the trajectories that are most important due to their elevation and eastward direction. The original storm's effect on the trajectories is apparent in the time/height trajectory plot. The elevated parcels were all lifted abruptly around 06 UTC. This sudden lift likely helped to initiate the convection in the model for this night. Due to the model only producing CI in this region, the information gained from the back-trajectories is limited.

For 5 July 2015, the trajectory analysis was only done for the second episode of CI on this night since the model was not able to accurately resolve the first line of CI. As discussed in the previous section, WRF had difficulties modeling the LLJ on this night so the trajectories must be used with caution. The 5 July 2015 trajectories do not have the same fanning out appearance as the trajectories for 1-2 June 2015 (Fig. 65). Instead, there seems to be two clusters of trajectories. One cluster of trajectories is the low-level parcels which begin southeast of the CI area and track northwestward into the CI area while sinking throughout the night. The other group of trajectories are the parcels in the middle and upper levels of the LLJ where parcels start southwest of

the CI area and move toward the northwest with a persistent rising motion throughout the night. This rising and sinking motion would be expected to occur due to isentropic motion when the isentropes slope toward the west. The parcels at higher elevations would rise due to their westerly component, while the lower parcels would sink due to their easterly component. Around 09 UTC it appears that the parcels were in a downdraft due to the sudden decrease in the height of all middle and upper level parcels. There were multiple small storms that developed in this area in this WRF model run so it is not surprising that the parcels were affected by one of the storms. While this case was different than the 1-2 June 2015 cases, the trajectories indicated that persistent rising throughout the night at the top of the LLJ was a common feature. This rising motion was important for bringing the air parcels closer to saturation and increasing their instability, while also ensuring they were transported to a region with less stability.

Chapter 4: Heterogeneous Low-Level Jet Theory and Convection Initiation Conceptual Model

4.1. Heterogeneous LLJs

4.1.1. Buoyancy Gradients

In previous chapters, it was identified that heterogeneous, veering with height LLJs were capable of causing nocturnal elevated CI. The forcing behind these heterogeneous LLJs, however, has not yet been explained. As discussed in Chapter 1, much of our knowledge of LLJs forcing and development comes from highly idealized analytical studies that assume the environment in which the LLJ develops is horizontally uniform. The most complete analytical model of Great Plains LLJs was developed by Shapiro et al. (2016). Since this model assumes along-slope homogeneity, it is not able to accurately model the LLJs on these nights. The framework used to develop the analytical model can be applied, however, to obtain a qualitative understanding of the additional forcings that must be present to produce the LLJs seen on this night.

The Shapiro et al. (2016) analytical model uses a slope following coordinate system. In this coordinate system the 1-D Boussinesq approximated equations of motion and thermal energy become:

$$\frac{\partial u}{\partial t} = fv - \frac{\partial \Pi}{\partial x} - b\sin\alpha + K\frac{\partial^2 u}{\partial z^2}, \tag{1}$$

$$\frac{\partial v}{\partial t} = -fu + K\frac{\partial^2 v}{\partial z^2}, \tag{2}$$

$$0 = -\frac{\partial \Pi}{\partial z} + b\cos\alpha, \tag{3}$$

$$\frac{\partial b}{\partial t} = uN^2\sin\alpha + K\frac{\partial^2 b}{\partial z^2}. \tag{4}$$

where u is the along-slope component of the wind (with the x axis pointing down the slope), v is the cross-slope component and α is the slope angle. f is the Coriolis parameter where the small deviation in the parameter due to the slightly sloped surface is ignored. b is buoyancy which is defined as

$$b = g\frac{\theta-\theta_e}{\theta_0}, \tag{5}$$

where θ is potential temperature, θ_e is the environmental potential temperature (considered to vary linearly with height z^* and θ_0 is a constant reference value of potential temperature. Perturbation pressure is defined as $\Pi = \frac{p-P(z^*)}{\rho_0}$ where p is pressure, $P(z^*)$ is the environmental pressure profile at a fixed location x^* and ρ_0 is a constant value of density. The Brunt-Viasala frequency (also known as buoyancy frequency) is defined as $N = \sqrt{\frac{g}{\theta_0}\frac{d\theta_e}{dz^*}}$ where g is gravity. Lastly, K is eddy diffusivity which is considered spatially constant and the same for both heat and momentum.

While for this thesis the system of equations need not be solved, boundary conditions will still be considered as they create important constraints for the qualitative analysis. At the surface, the no slip condition is applied,

$$u(0) = 0 \text{ and } v(0) = 0, \tag{6}$$

and far above the slope buoyancy disappears,

$$\lim_{z\to\infty} b = 0, \tag{7}$$

and the wind is equal to the free atmosphere geostrophic wind,

$$\lim_{z\to\infty} v = v_{g\infty} = \frac{1}{f}\left(\frac{\partial \Pi}{\partial x}\right)_{\infty}. \tag{8}$$

An important but limiting assumption used by Shapiro et al. (2016) is that buoyancy does not change along the slope. From this assumption, Shapiro et al. (2016) shows

that the environmental geostrophic wind, v_g, must be spatially and temporally constant. Taking $\partial/\partial x$ of (3) under this constant along-slope buoyancy assumption and re-ordering the differentiation yields,

$$\frac{\partial}{\partial z}\frac{\partial \Pi}{\partial x} = 0. \tag{9}$$

Integrate (8) with respect to z to obtain

$$\frac{\partial \Pi}{\partial x} = f(x,t) \tag{10}$$

where $f(x,t)$ is a function of integration (at most a function of x and t). Due to (8), this function of integration cannot be a function of x and t so $\frac{\partial \Pi}{\partial x}$ is constant everywhere, which means the environmental geostrophic wind is constant everywhere.

The Shapiro et al. (2016) analytical solution accounts for both the inertial oscillation and the buoyancy effects. The buoyancy effects essentially enhance the geostrophic wind (not to be confused with the environmental geostrophic wind), which, in Appendix A of Shapiro et al. (2016), is defined as:

$$V_g = v_g + \frac{1}{f} b \sin\alpha. \tag{11}$$

From (11), one can see that the geostrophic wind depends on the constant free atmosphere geostrophic wind and also buoyancy. Since the maximum wind speed in an inertial oscillation depends on the strength of the geostrophic wind, one would expect a stronger LLJ when the free atmosphere geostrophic wind is large and the buoyancy is positive at sunset when the inertial oscillation begins. Obviously, there are other factors that affect LLJ strength, but at the most basic level, the geostrophic wind strength has the most control on the LLJ maximum wind speed.

The LLJs on the nights of the CI events do not follow the constant along-slope buoyancy restriction of the analytical model. The RAP analysis for these nights shows that winds at the upper levels were northerly on all three nights. These upper level winds can be used as a proxy for the free atmosphere geostrophic wind. With a northerly free atmosphere geostrophic wind, the only way a southerly LLJ could occur with homogeneous conditions would be if there was very large positive buoyancy present in the boundary layer on these nights. The sounding FP-3 on 2 June 2015 shows that this is not the case, however. By extrapolating the free atmosphere potential temperature profile down to the surface and subtracting the surface temperature from the extrapolated potential temperature, one sees that the buoyancy is actually negative on 2 June 2015. Clearly the LLJs on these nights do not conform to the homogenous environment LLJs considered in the analytical model.

How do moderate to strong southerly LLJs develop on these nights when one dimensional forcings all favor a northerly LLJ? Let's consider the the differentiation of (3) with respect to *x* when buoyancy varies along the slope. Under these conditions the resulting equation is:

$$\frac{\partial}{\partial z}\frac{\partial \Pi}{\partial x} = \frac{\partial b}{\partial x}\cos\alpha. \tag{12}$$

Divided this equation by f to obtain:

$$\frac{\partial v_g}{\partial z} = \frac{1}{f}\frac{\partial b}{\partial x}\cos\alpha. \tag{13}$$

Equation (12) shows that if there is a negative buoyancy gradient (i.e buoyancy decreasing down the slope) then the environmental geostrophic wind must decrease with height. A thermal wind must be present. Therefore, southerly geostrophic winds at low levels could have occurred on the nights of the CI events if a negative buoyancy

gradient was present. With a buoyancy gradient, the strongest southerly geostrophic winds would occur at the ground and they would weaken with height and eventually change sign.

In order to determine if buoyancy gradients were driving the forcing of the LLJ on this night, a method is needed to measure the buoyancy gradients. Obtaining exact values of buoyancy from soundings can be quite subjective since they require estimates of free atmosphere static stability, a correct identification of the capping inversion, and proper interpolation of the free atmosphere static stability. Large errors could occur if soundings were used to estimate buoyancy gradients directly. Luckily, buoyancy gradients can be evaluated through potential temperature gradients with minimal assumptions.

The only assumption needed to estimate buoyancy gradients is that the buoyancy frequency, N, is constant everywhere. Under this assumption the environmental potential temperature is controlled by

$$\theta_e = const + \frac{\theta_0}{g} N^2 z^*. \tag{14}$$

The constant in this equation can be considered to be the environmental potential temperature at sea level. Take $\partial/\partial x$ of (5) and (14) to obtain:

$$\frac{\partial b}{\partial x} = \frac{g}{\theta_0}\frac{\partial \theta}{\partial x} - \frac{g}{\theta_0}\frac{\partial \theta_e}{\partial x}, \tag{15}$$

$$\frac{\partial \theta_e}{\partial x} = -\frac{\theta_0}{g} N^2 \sin\alpha. \tag{16}$$

Finally, plug (16) into (15),

$$\frac{\partial b}{\partial x} = \frac{g}{\theta_0}\frac{\partial \theta}{\partial x} + N^2 \sin\alpha. \tag{17}$$

From (17) the buoyancy gradient at any height above the slope can be determined if an estimate of the static stability can be obtained and the potential temperature gradient across the slope is known. Using the surface data from FP-3 and FP-5 the buoyancy gradients for all three CI nights were calculated for a standard N value of 0.01 s^{-1}. Table 2 shows that a negative buoyancy gradient was present on all three nights with 2 June 2015 having the strongest gradient. This confirms that buoyancy gradients were responsible for creating a northerly shear of the geostrophic wind which is consistent with the northerly wind in the free atmosphere during these nights.

Since the environmental geostrophic wind must decrease with height when a negative buoyancy gradient is present, the LLJs on these nights would have larger vertical shear than nights when buoyancy gradients do not occur. This is again due to the fact that the inertial oscillation strength is dependent on the geostrophic wind, and the geostrophic wind changes with height when a buoyancy gradient is present. The presence of a buoyancy gradient also implies that horizontal gradients in the geostrophic wind could exist. Taking $\partial/\partial x$ of (11) yields

$$\frac{\partial V_g}{\partial x} = \frac{\partial v_g}{\partial x} + \frac{1}{f}\frac{\partial b}{\partial x}\sin\alpha. \tag{18}$$

This expression shows that the change in the geostrophic wind depends on the change in the free atmosphere geostrophic wind with respect to x and also the change in buoyancy with respect to x. Table 2 also shows the along-slope geostrophic wind shear implied by just the buoyancy gradient term. The buoyancy gradients on these nights would tend to cause the southerly geostrophic wind to decrease toward the east. As previously mentioned, the resulting wind speeds from the inertial oscillation is

dependent on the geostrophic wind strength so the LLJ on these nights would be expected to be strongest in western Kansas and weaken toward the east. Observations and models confirm that this occurred on all three nights.

These buoyancy gradients would tend to occur in the region between an upstream ridge and downstream trough. The trough is typically associated with cooler air and as this cooler air moves eastward, warmer air associated with the ridge would fill in to the west. This enhances the temperature gradient over the Great Plains, which in turn, creates buoyancy gradients. In fact, on all three CI nights this pattern was located over the Great Plains. In addition to the synoptic creation of buoyancy gradients, the long-term soil moisture gradient that is present over the region would also create buoyancy gradients (Fig 66). Soil moisture tends to be higher in eastern Kansas and lower in western Kansas. Therefore, daytime heating would cause western Kansas to warm faster than eastern Kansas as the latent heat flux would be smaller in western Kansas. This uneven heating of the slope creates a buoyancy gradient and can enhance an existing gradient due to the synoptic pattern.

4.1.2. LLJ Depth

Ultimately, east-west LLJ depth variations arise from east-west variations in the depth of the daytime convective boundary layer. In a deeper boundary layer, the effects of the surface friction are felt at higher elevations than for a shallower boundary layer. When turbulent mixing decreases at sunset, the LLJ in the region with a deeper boundary will therefore be deeper than the LLJ in the shallower boundary layer.

What could cause east-west variations in boundary layer height? The mixed layer depth is controlled by

$$\frac{dz_i}{dt} = w_e + w_i, \tag{19}$$

where $z_i$is the mixed layer depth, w_e is the entrainment velocity, and w_i is the large scale vertical velocity (Wallace and Hobbs, 2006). The large scale vertical velocity is controlled by the convergence and divergence in the boundary layer, with convergence increasing boundary layer heights and divergence decreasing boundary layer heights. It was shown that in the presence of a negative buoyancy gradient, a southerly geostrophic wind must decrease toward the east. The buoyancy gradient should also be at a maximum magnitude over central and eastern Kansas due to the soil moisture gradient typically present (see Fig. 66). During the daytime, frictional drag causes the winds in the boundary layer to develop a cross-isobar component, which would be easterly for a southerly geostrophic wind. Due to the gradient in the geostrophic wind, this upslope component to the boundary layer winds will cause the flow to become divergent. This divergence produces large scale sinking motion, which would act to decrease the boundary layer height with time. However, this divergence would be maximized in central and eastern Kansas due to the stronger buoyancy gradient in that location. Therefore, central and eastern Kansas would have stronger sinking motion, which contributes to the uneven boundary layer depth seen across the slope.

In addition to the enhanced sinking motion in eastern and central Kansas, differences in the entrainment velocity across the state would also exist due to buoyancy and soil moisture gradients. Entrainment velocity can be approximated by

$$w_e = \frac{AF_{HS}}{\Delta\theta}, \tag{20}$$

where A is the entrainment heat flux ratio normally set to a value of 0.2 for shear-free boundary layers but in the presence of shear, values can be greater than 0.2 (Conzemius and Fedorovich, 2006), F_{HS} is the surface heat flux, and $\Delta\theta$ is the capping inversion strength (Wallace and Hobbs, 2006). The surface heat flux can then be approximated using the bulk aerodynamic method,

$$F_H = C_H|V|(T_s - T_{air}), \tag{21}$$

where C_H is the bulk transfer coefficient for heat, $|V|$ is the wind speed, T_s is surface temperature and T_{air} is air temperature. (21) shows that the surface heat flux is dependent on the wind speed over the surface and also the temperature of the surface. Since wind speeds and surface temperatures in western Kansas are greater due to the buoyancy gradient and soil moisture gradient, the surface heat flux would also be greater. This larger surface heat flux would lead to a stronger entrainment velocity in western Kansas, which further enhances the uneven depth of the boundary layer across the slope.

4.2. CI Conceptual Model

Using the knowledge gained from the PECAN observations, RAP analysis and model, WRF trajectories, and analytical models, a conceptual model for elevated north-south lines of nocturnal CI can be created.

These north-south lines of CI would tend to occur behind a trough exiting the Great Plains. This pattern is preferred for this CI as it helps to create a buoyancy gradient across the state. As the trough exits, warmer, moister air moves into the western portion of Kansas while colder, drier air remains in the eastern part of Kansas.

The buoyancy gradient that is created due to this synoptic pattern is then enhanced in central and eastern Kansas due to the soil moisture gradient present in that region. Due to the buoyancy gradient created by this set-up, the daytime development of the boundary layer is non-uniform. The larger buoyancy in western Kansas causes wind speeds in western Kansas to be faster than those in eastern Kansas and the lower soil moisture causes the surface temperature to be higher than in eastern Kansas. Both of these features enhances surface heat fluxes in the west. Divergence is also enhanced in eastern and central Kansas as frictional effects turn the boundary layer winds up the slope. The enhanced surface heat fluxes in western Kansas and the enhanced divergence in eastern and central Kansas cause a non-uniform boundary layer across Kansas with the boundary layer in western Kansas being deeper, so at sunset an east-west cross-section of Kansas would look like Fig. 67. Above the boundary layer on these days, the free atmosphere winds tend to be north-northwesterly. This is due to the buoyancy gradient along the slope creating a free atmosphere thermal wind which causes the maximum meridional component of the the free atmosphere geostrophic wind to be at the surface. Fig. 66 also shows the expected wind distribution across Kansas due to the buoyancy gradient.

After sunset, the LLJ begins to develop. The LLJ is stronger and deeper in western Kansas while the LLJ in eastern Kansas is weaker and more shallow. As the LLJ veers with time, the upper regions of the LLJ acquire a westerly component. Due to the east-west difference in LLJ strength and depth, convergence occurs at the top of the LLJ (Fig. 68). The westerly component of the wind at the top of the LLJ also begins to advect moisture toward the east. The initially non-uniform boundary layer

heights cause this moisture to be advected from a stable region below a capping inversion in western Kansas, to a region above the capping inversion in the east where there is less CIN. Along with this eastward moisture advection, there is slight lift (potentially isentropic lift, but the exact cause is unknown), which causes the air to become saturated as it moves eastward. The convergence from the winds at the top of the LLJ and the saturated air in this convergence zone essentially primes a north-south line of the LLJ for convection. This primed region for CI slowly moves to the east throughout the night due to the LLJ advecting itself eastward. With this slow progression eastward, convection can be initiated if this convergence line moves into a region where the upper-level thermodynamic environment is more favorable. In some cases, the convergence alone is enough to initiate the convection, but outflow boundaries and bores can also cause initiation to occur in the primed region. In these cases, the CI only develops in the north-south line that has been primed for convection and nowhere else along the disturbance. If the disturbance comes from the north, the line of CI will appear orthogonal to the disturbance.

Chapter 5: Summary and Future Work

5.1. Summary

Two of the goals of PECAN were to elucidate the processes causing elevated nocturnal CI over the Great Plains, and further study the nocturnal LLJ. For this thesis, three cases of CI that occurred during the PECAN field experiment were analyzed from observational, modeling, and analytical perspectives. The three cases chosen for analysis all had similar north-south lines of CI. The cause of these north-south lines of CI was not previously discussed before this thesis. These lines of CI occurred on the eastern edge of the LLJ, while most of the attention for CI is on the northern terminus of the LLJ. In fact, the forecasters for the PECAN experiment were perplexed as to why NWP was forecasting for these north-south lines of CI to occur when they were displaced far from the northern terminus of the LLJ.

Before this analysis it was hypothesized that a mechanism similar to the one discussed in Bonner (1966) was causing these north-south lines of CI to occur on the eastern edge of the LLJ. Bonner (1966) found in one case study that convergence increased on the eastern edge of the LLJ as the LLJ wind direction veered. While Bonner (1966) did not explicitly identify the cause of this convergence, a heterogeneous LLJ would be capable of causing the convergence found in that study. This led to the following research questions, which can now be answered:

1. What role does the Great Plains LLJ play in the initiation of these north-south lines of convection? What ultimately was the initiation source for these north-south lines of convection. Was a mechanism similar to the one discussed in Bonner (1966) involved?

The Great Plains LLJ was the primary driver in initiating these north-south lines of CI. The LLJs on these nights veered with height and were horizontally heterogeneous, which created convergence zones parallel to the primary LLJ axis. The LLJs became horizontally heterogeneous due to a large-scale buoyancy gradient that was present across the Great Plains region. The convergence zones were created as the LLJ veered with time, causing the winds at the top of the LLJ to become more westerly. Since the wind speeds decreased to the east, the westerly winds at the top of the LLJ created north-south lines of convergence. Buoyancy gradients also indirectly affected the depth of the LLJ across the state by augmenting the daytime boundary layer growth across the slope. This variation in LLJ strength across the state helped to enhance the north-south oriented convergent regions of the LLJ. In addition to the convergence, the top of the LLJ also advected moisture eastward which helped to destabilize the CI region. The uneven depth of the LLJ caused the LLJ to advect this moisture above the capping inversion in eastern Kansas where there was less CIN.

Ultimately, the initiation source for the CI was convergence at the top of the LLJ owing to a heterogeneous LLJ in a region with little CIN for a saturated parcel. On 1-2 June 2015, outflow/bores could have also contributed to the initiation of the convection, but the CI that occurred near these features was only located in the region where the LLJ convergence was present. This suggests that the bores/outflow by themselves were insufficient for initiating convection, but instead assisted in initiating the convection in the convergent regions.

The CI mechanism on these nights had some similarities to features discussed in Bonner (1966), but there are some noticeable differences. In Bonner (1966) only

one level of the LLJ was considered when identifying the convergent regions. In the cases presented for this work, the LLJ increased with height due to the uneven boundary layer depth, which caused the convergence to be strongest at a height above that of the maximum LLJ wind speed. In addition, in Bonner (1966) the convergence was shown to shift across a relatively symmetric LLJ. The LLJs on the nights presented in this thesis were not necessarily symmetric. The fastest wind speeds occurred in the western part of the state and decreased in intensity toward the east. Multiple convergent zones also appeared to develop on these nights. The uneven LLJ depth created one convergence zone, but the second convergence zone occurred at the true edge of the LLJ. The first type of convergence zone was not seen in Bonner (1966), but the second convergence zone is similar to what was found in Bonner (1966). The overall concept that the veering with time of a horizontally heterogeneous LLJ would cause convergence is confirmed by these cases, but the complexities in creating the convergence are understated by Bonner (1966).

This thesis also addressed the predictability of the north-south lines of CI. The predictability of CI in general is quite low, which is why this topic was one of the focuses of PECAN. For the three events presented in this thesis, NWP tended to overpredict the amount of CI that occurred on these nights. This led to the following question:

2. What is the sensitivity of the CI to the environment and LLJ and can these north-south lines of convection be accurately forecasted given this sensitivity?

The WRF sensitivity analysis was primarily used to answer this question. The CI forecasts from WRF were found to be highly sensitive to the initial conditions and

PBL used. The sensitivity of these forecasts, however, trended toward an overproduction of CI. The boundary layer schemes were biased toward over-convecting on these nights. This suggests that the primary forecasting problem for these events is inferring the correct CI signal from the noise. It does not appear that the models (at least WRF and RAP) have a problem with identifying when these events are going to occur. For the WRF runs, the over-convected forecasts were connected to the models being too moist and incorrectly forecasting the depth of the LLJ. Therefore, in order to improve forecast skill, improvements in PBL schemes and model data assimilation would be necessary for the correction of problems seen in the WRF runs. An important consideration, however, is that the cases used for this analysis were identified primarily by the robustness of the north-south lines of CI that occurred. It is possible that this CI mechanism could be occurring on other nights where the CI forcing is not as strong, and that these events may be harder to model, and therefore forecast.

A conceptual model was created to be used as an aid for forecasting these CI events. The conceptual model identifies that these events occur behind a trough with a buoyancy gradient along the slope. The buoyancy gradient is the key feature for these CI events as this gradient causes the inhomogeneous conditions that initiate the convection. Therefore, this conceptual model can be used in conjunction with a large-scale NWP forecast, such as the GFS, to identify nights where this type of CI may occur days before the event.

5.2. Future Work

The analysis of these CI events led to several additional questions about CI and the LLJ. The first remaining problem is the subtle large-scale lift that is occurring within the LLJ on these nights. The analysis of these cases suggests that the lift is isentropic, but because the LLJ is on the edge of synoptic scale, using an isentropic framework can be dubious. More work is need to identify why this lift is occurring and whether or not this lift is a common feature of Great Plains LLJs.

Additional observational work is also needed to examine these north-south oriented convergent regions of the LLJ. The FP-data from PECAN was quite coarse and the organization of the network was not optimal for examining such convergence. Observations from the LLJ IOPs from PECAN have also captured sudden increases in vertical motion and increases in LLJ depth, which are consistent with a non-uniform LLJ creating convergence as it advects itself eastward, but there was no convection that occurred on these nights. Are these north-south lines of convergence common in Great Plains LLJs and what determines whether or not convection is associated with this convergence?

Finally, the effect of buoyancy gradients on the LLJ needs to be further explored. In work unrelated to this thesis, the author has found that along-slope buoyancy gradients are present in the majority of southerly LLJ events over the Great Plains. This suggests that these buoyancy gradients are an important factor in most of the LLJs that occur over this region. This thesis was able to qualitatively explain how a buoyancy gradient would affect the LLJ, but a more robust analysis on the effects of buoyancy gradients on the LLJ is needed.

References

Anderson, C. J. and R. W. Arritt, 2001: Representation of summertime low-level jets in the central United States by the NCEP-NCAR reanalysis. *J. Climate*, **14**, 234-247.

Astling, E. G., J. Paegle, E. Miller, and C. J. O'Brien, 1985: Boundary layer control of nocturnal convection associated with a synoptic scale system. *Mon. Wea. Rev.*, **113**, 540-552.

Benjamin, S. G., S. S. Weygandt, J. M. Brown, M. Hu, C. R. Alexander, T. G. Smirnova, J. B. Olson, E. P. James, D. C. Dowell, G. A. Grell, H. Lin, S. E. Peckham, T. L. Smith, W. R. Moninger, and J. S. Kenyon, 2016: A North American hourly assimilation and model forecast cycle: The Rapid Refresh. *Mon. Wea. Rev.*, **144**, 1669-1694.

Bonner, W. D., 1966: Case study of thunderstorm activity in relation to the low-level jet. *Mon. Wea. Rev.*, **3**, 167-178.

Bonner, W. D., 1968: Climatology of the low level jet. *Mon. Wea. Rev.*, **96**, 833-850.

Bonner, W. D., and J. Paegle, 1970: Diurnal variations in boundary layer winds over the south-central United States in summer. *Mon. Wea. Rev.*, **98**, 735-744.

Blackadar, A. K., 1957: Boundary layer wind maxima and their significance for the growth of nocturnal inversions. *Bull. Amer. Meteor. Soc.*, **38**, 283-290.

Buajitti, K. and A. K. Blackadar, 1957: Theoretical studies of diurnal wind-structure variations in the planetary boundary layer. *Quart. J. Roy. Meteor. Soc.*, **83**, 486-500.

Carbone, R. E., J. D. Tuttle, D. A. Ahijevych, and S. B. Trier, 2002: Inferences of predictability associated with warm season precipitation episode. *J. Atmos. Sci.*, **59**, 2033-2056.

Clark, A. J., W. A. Gallas, and T. Chen, 2007: Comparison of diurnal precipitation in convective-resolving and non-convective-resolving mesoscale models. *Mon. Wea. Rev.*, **135**, 3456-3473.

Clark, R., 2016: FP3 Ellis, KS radiosonde data, Version 2.0. https://doi.org/10.5065/D6GM85DZ. Accessed 5 Oct 2016.

Cohen, A. E., S. M. Cavallo, M. C. Coniglio, and H. E. Brooks, 2015: A review of planetary boundary layer schemes and their sensitivity in simulating southeastern US cold season severe weather environments. *Wea. Forecasting*, **30**, 591-612.

Conzemius, R. J. and E. Fedorovich, 2006: Dynamics of sheared convective boundary layer entrainment. Part I: Methodological background and large-eddy simulations. *J. Atmos. Sci.*, **63**, 1151-1178.

Crook, N. A., 1996: Sensitivity of moist convection forced by boundary layer processes to low-level thermodynamic fields. *Mon. Wea. Rev.*, **124**, 1767-1785.

Davis, C. A., K. W. Manning, R. E. Carbone, S. B. Trier, and J. D. Tuttle: 2003: Coherence of warm-season continental rainfall in numerical weather prediction models. *Mon. Wea. Rev.*, **131**, 2667-2679.

Delgado, R., Carroll, B., and Demoz, B., 2016: FP2 UMBC Doppler lidar line of sight wind data. Version 1.1. https://doi.org/10.5065/D6Q81B4H. Accessed 30 Jan 2017.

Doubler, D., J. Winxler, X. Bian, C. Walters, and S. Zhong, 2015: An NARR-derived climatology of southerly and northerly low-level jets over North America and coastal environs. *J. Appl. Meteor. Climatol.*, **54**, 1596-1619.

Geerts, B., D. Parsons, C. L. Ziegler, T. M. Weckworth, D. D. Turner, J. Wurman, K. Kosiba, R. R. Rauber, G. M. McFarquhar, M. D. Parker, R. S. Schumacher, M. C. Coniglio, K. Haghi, M. I. Biggerstaff, P. M. Klein, W. A. Gallas, B. B. Demoz, K. R. Knupp, R. A. Ferrare, A. R. Nehrir, R. D. Clark, X. Wang, J. M. Hanesiak, J. O. Pinto, and J. A. Moore, 2016: The 2015 Plains Elevated Convection at Night (PECAN) field project. *Bull. Amer. Meteor. Soc.* doi:10.1175/BAMS-D-15-00257.1, in press.

Hanesiak, J., Turner, D. 2016. FP3 University of Manitoba Doppler Lidar Wind Profile Data. Version 1.0. https://doi.org/10.5065/D60863P5. Accessed 30 Jan 2017.

Higgins, R., Y. Yao, E. Yarosh, J. Janowiak, and K. Mo, 1997: Influence of the Great Plains low-level jet on summertime precipitation and moisture transport over the central United States. *J. Climate*, **10**, 481-507.

Holdridge, D. and D. Turner, 2015: FP6 Hesston, KS radiosonde data, Version 1.0, https://doi.org/10.5065/D6765CD0. Accessed 5 Mar 2016.

Holton, J. R., 1967: The diurnal boundary layer wind oscillation above sloping terrain. *Tellus*, **19**, 199-205.

Hong, S.-Y., S. Y. Noh, and J. Dudhia, 2006: A new vertical diffusion package with an explicit treatment of entrainment processes. *Mon. Wea. Rev.*, **134**, 2318-2341.

Janjic, Z. I., 1990: The step-mountain coordinate: Physical package. *Mon. Wea. Rev.*, **118**, 1429-1443.

Janijic, Z. I., 1994: The step-mountain eta coordinate model: Further developments of the convection, viscous sublayer, and turbulence closer schemes. *Mon. Wea. Rev.*, **122,** 927-945.

Maddox, R. A., 1980: Mesoscale convective complexes. *Bull. Amer. Meteor. Soc.*, **61**, 1374-1387.

Maddox, R. A., 1983: Large-scale meteorological conditions associated with midlatitude, mesoscale convective complexes. *Mon. Wea. Rev.*, **111**, 1475-1493.

Mitchell, M. J., R. W. Arritt, and K. Labas, 1995: A climatology of the warm season Great Plains low-level jet using wind profiler observations. *Wea. Forecasting*, **10**, 576-591.

Nakanishi, M. and H. Niino, 2004: An improved Mellor-Yamada level-3 model with condensation physics: Its design and verification. *Bound.-Layer Meteor.*, **112**, 1-31.

Paegle, J. and D. W. McLawhorn, 1973: Correlation of nocturnal thunderstorms and boundary-layer convergence. *Mon. Wea. Rev.*, **101**, 866-883.

Paegle, J. and G. Rasch, 1973: Three-dimensional characteristics of diurnally varying boundary-layer flows. *Mon. Wea. Rev.*, **101**, 746-756.

Parish, T. R., 2016: A comparative study of 3 June 2015 Great Plains low-level jet. *Mon. Wea. Rev.* **144**, 2963-2979.

Parish, T. R. and L. Oolman, 2010: On the role of sloping terrain in the forcing of the Great Plains low-level jet. *J. Atmos. Sci.*, **67**, 2690-2699.

Pinto, J. O., J. A. Grim, and M. Steiner, 2015: Assessment of the High-Resolution Rapid Refresh model's ability to predict mesoscale convective systems using object-based evaluation. *Wea. Forecasting*, **30**, 892-913.

Pitchford, K. L. and J. London, 1962: The low-level jet as related to nocturnal thunderstorms over midwest United States. *J. Appl. Meteor.*, **1**, 43-47.

Rasmusson, E. M., 1967: Atmospheric water vapor transport and the water balance of North America. Part I: Characteristics of the water vapor flux field. *Mon. Wea. Rev.*, **95**, 403-426.

Rife, D. L., J. O. Pinto, A. J. Monaghan, and C. A. Davis, 2010: Global distribution and characteristic of diurnally varying low-level jets. *J. Climate*, **23**, 5041-5063.

Song. J., K. Liao, R. L. Coulter, and B. M. Lesht, 2005: Climatology of the low-level jet at the Southern Great Plains Atmospheric Boundary Layer Experiments site. *J. Appl. Meteor.*, **44**, 1593-1606.

Shapiro, A. and E. Fedorovich, 2009: Nocturnal low-level jets over a shallow slope. *Acta Geophys.*, **57**, 950-980.

Shapiro, A. and E. Fedorovich, 2010: Analytical description of a nocturnal low-level jet. *Quart. J. Roy. Meteorol. Soc.*, **136**, 1255-1262.

Shapiro, A., E. Fedorovich, and S. Rahimi, 2016: A unified theory for the Great Plains nocturnal low-level jet. *J. Atmos. Sci.*, **73**, 3037-3057.

Spuler, S. M., K. S. Repasky, B. Morely, D. Moen, M. Haymen, and A. R. Nehrir, 2015: Field-deployable diode-laser-based differential absorption (DIAL) for profiling water vapor. *Atmos. Meas. Tech.*, **8**, 1073-1087.

Skamarock, W. C., J. B. Klemp, J. Dudhia, D. O. Gill, D. M. Barker, M. G. Duda, X.-Y. Huang, W. Wang, and J. G. Powers, 2008: A description of the Advanced Research WRF Version 3. *NCAR Tech. Note NCAR/TN-475+STR,* 113 pp.

Stensrud, D., 1996: Importance of low-level jets to climate: A review. *J. Climate*, **9**, 1698-1711.

Storm, B., J. Dudhia, S. Basu, A. Swift, and I. Giammanco, 2009: Evaluation of the WRF model on forecasting low-level jets: Implications for wind energy. *Wind Energy*, **12**, 81-90.

Sukoriansky, S., B. Galperin, and V. Perov, 2005: Application of a new spectral theory of stably stratified turbulence to the atmospheric boundary layer over sea ice. *Bound.-Layer Meteor.*, **117**, 231-257.

Ting, M. and H. Wang, 2006: The role of the North American topography on the maintenance of the Great Plains summer low-level jet. *J. Atmos. Sci.*, **63**, 1056-1068.

Tollerud, E. I., F. Caracena, S. E. Koch, B. D. Jamison, R. M. Hardesty, B. J. McCarty, C. Kiemle, R. S. Collander, D. L. Bartels, S. Albers, B. Shaw, D. L. Birkenheuer, and W. A. Brewer, 2008: Mesoscale moisture transport by the low-level-jet during the IHOP field experiment. *Mon. Wea. Rev.*, **136**, 3781-3795.

Trier, S. B., and D. B. Parsons, 1993: Evolution of environmental conditions preceding the development of a nocturnal mesoscale convective complex. *Mon. Wea. Rev.*, **121**, 1078-1098.

Trier, S. B., C. A. Davis, D. A. Ahijevych, M. L. Weisman, and G. H. Bryan, 2006: Mechanisms supporting long-lived episodes of propagating nocturnal convection within a 7-day WRF model simulation. *J. Atmos. Sci.*, **63**, 2437-2461.

Tuttle, J. D. and C. A. Davis, 2006: Corridors of warm season precipitation in the central United States. *Mon. Wea. Rev.*, **134**, 2297-2317.

UCAR/NCAR – Earth Observing Laboratory, 2015: FP3 NCAR/EOL 449 MHz Profiler 30 minute Winds Data, Version 0.1 [PRELIMINARY], http://data.eol.ucar.edu/dataset/485.022. Accessed 11 July 2016.

UCAR/NCAR Earth Observing Laboratory, 2016: FP3 FP4 FP5 QC 5 min surface data, tilt corrected, Version 1.0, https://doi.org/10.5065/D6BZ645V. Accessed 30 Jan 2017.

UCAR/NCAR Earth Observing Laboratory, 2016: FP5 NCAR/EOL ISS QC 915 MHz profiler 30-minute consensus winds and moments, Version 1.0, http://dx.doi.org/10.5065/D6RVOKXH. Accessed 11 July 2016.

UCAR/NCAR Earth Observing Laboratory, 2016: FP5 QC radiosonde data, Version 2.0, https://doi.org/10.5065/D6ZG6QF7. Accessed 5 Oct 2016.

Uccellini, L. W., 1980: On the role of upper tropospheric jet streaks and leeside cyclogenesis in the development of low-level jets in the Great Plains. *Mon. Wea. Rev.*, **108**, 1689-1696.

Uccellini, L. W. and D. R. Johnson, 1979: The coupling of upper and lower tropospheric jet streaks and implications for the development of severe convective storms. *Mon. Wea. Rev.*, **107**, 682-703.

Vermeesch, K., 2015: FP2 Greensburg, KS radiosonde data, Version 1.0, https://doi.org/10.5065/D6FQ9TPH. 18 Apr 2016.

Wallace, J. M., 1975: Diurnal variations in precipitation and thunderstorm frequency over the continuous United States. *Mon. Wea. Rev.*, **103**, 406-419.

Wallace, J. M., and P.V. Hobbs, 2006: *Atmospheric Science: An Introductory Survey*. Elsevier Academic Press, 488 pp.

Walters, C. K., J. A. Winkler, 2001: Airflow configurations of warm season southerly low-level wind maxima in the Great Plains. Part I: Spatial and temporal characteristics and relationship to convection. *Wea. Forecasting*, **16**, 513-530.

Walters, C. K., J. A. Winkler, R. P. Shadbolt, J. van Ravensway, and G. D. Bierly, 2008: A long-term climatology of southerly and northerly low-level jets for the central United States. *Ann. Assos. Amer. Geogr.*, **98**, 521-552.

Walters, C., J. Winkler, S. Husseini, R. Keeling, J. Nikolic, and S. Zhong, 2014: Low-level jets in the North American Regional Reanalyis (NARR): A comparison with rawinsonde observations. *J. Appl. Meteor. Climatol.*, **53**, 2093-2113.

Weckwerth, T. M. and D. B. Parsons, 2006: A review of convection initiation and motivation for IHOP_2002. *Mon. Wea. Rev.*, **134**, 5-22.

Wexler, H., 1961: A boundary layer interpretation of the low-level jet. *Tellus*, **13**, 368-378.

Whiteman, C. D., X. Bian, and S. Zhong, 1997: Low-level jet climatology from enhanced rawinsonde observations at a site in the southern Great Plains. *J. Appl. Meteor.*, **36**, 1363-1376.

Whiteman, D., 2016: FP2 NASA/GSFC ALVICE Raman lidar data and imagery, Version 1.0, https://doi.org/10.5065/D63X8525. Accessed 31 Jan 2017.

Whiteman, D. N., S. H. Melfi, and R. A. Ferrare, 1992: Raman lidar system for the measurements of water vapor and aerosols in the Earth's atmosphere. *Appl. Opt.*, **31**, 3068-3082.

Wilczak, J. M., R. G. Strauch, F. M. Ralph, B. L. Weber, D. A. Merritt, J. R. Jordan, D. E. Wolfe, L. K. Lewis, D. B. Wuertz, J. E. Gaynor, S. A. McLaughlin, R. R. Rogers, A. C. Riddle, and T. S. Dye, 1995: Contamination of wind profiler data by migrating birds: Characteristics of corrupted data and potential solutions. *J. Atmos. Oceanic Technol*., **12**, 449-467.

Wilson, J. W. and W. E. Schreiber, 1986: Initiation of convective storms at radar-observed boundary-layer convergence lines. *Mon. Wea. Rev.*, **114**, 2516-2536.

Wilson, J. W. and R. D. Roberts, 2006: Summary of convective storm initiation and evolution during IHOP: Observational and modeling perspective. *Mon. Wea. Rev.*, **134**, 23-47.

Appendix A: Tables and Figures

Table 1. List of fixed PISA locations and instruments. Table adapted from Geerts et al. (2016).

ID	Location	Instrument Source	Instruments
FP1	Lamont, OK	DOE/ARM	Doppler lidar, Raman lidar, AERI, MWR, surface station with fluxes, radiosondes, four 915 MHz wind profilers, C-band scanning radar
FP2	Greensburg, KS	Naval Postgraduate School	Multi-level mean and flux tower (up to 16 m AGL), tethersonde, ceilometer, radiosonde, sodar
		Howard University	Dopplar lidar
		Univ. Maryland-Baltimore County	Doppler lidar, baskscatter lidar, MWR, radiosonde, surface station
		DOE/ARM	AERI
		NASA/GSFC	Raman lidar, Doppler lidar, X-band profiling radar, GPS ground-station for PWV
FP3	Ellis, KS	NCAR/EOL	915 MHz wind profiler, radiosonde, ceilometer, surface station with fluxes, GPS ground-station for PWV
		Millersville University	Tethersonde, surface station with fluxes, backscatter lidar, radiosonde, sodar with radio acoustic sounding system
		Univ. Manitoba	MWR and Doppler lidar
		DOE/ARM	AERI
FP4	Minden, NE	NCAR/EOL	915 MHz wind profiler, radiosonde, ceilometer, surface station with fluxes, GPS ground-station for PWV
		DOE/ARM	AERI
FP5	Brewster, KS	NCAR/EOL	915 MHz wind profiler, radiosonde, ceilometer, surface station with fluxes, GPS ground-station for PWV
		DOE/ARM	AERI
FP6	Hesston, KS	Univ. Manitoba	MWR, wind lidar
		DOE/ARM	AERI, radiosonde, surface station

Table 2. The 00 UTC observed buoyancy gradients between FP-3 and FP-5 with N=0.01 for the three CI cases. The implied free atmosphere thermal wind and implied horizontal geostrophic wind shear are calculated from the observed buoyancy gradient.

	Buoyancy Gradient (s^{-2})	**Implied Free Atmosphere Thermal Wind ($m\ s^{-1}\ km^{-1}$)**	**Implied Horizontal Geostrophic Wind Shear ($m\ s^{-1} 100km^{-1}$)**
1 June 2015	-3.45×10^{-7}	-3.79	-0.99
2 June 2015	-9.00×10^{-7}	-9.89	-2.59
5 July 2015	-7.33×10^{-7}	-8.05	-2.11

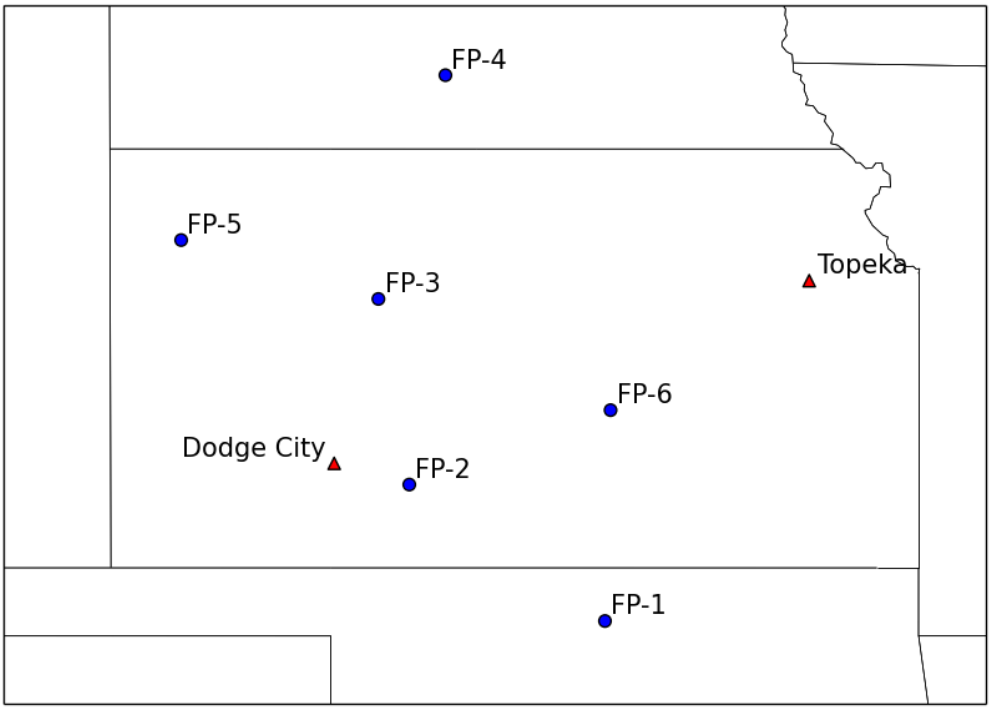

Figure 1. Locations of the fixed PISAs and NWS sounding stations.

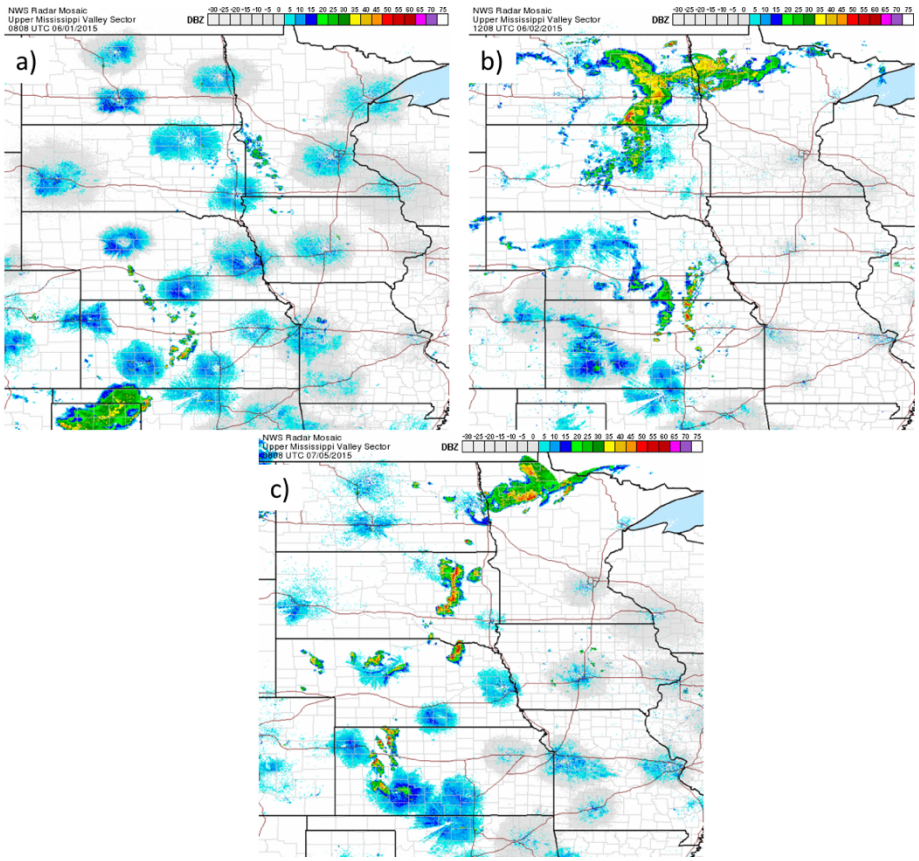

Figure 2. Mosaic 1 km radar reflectivity for a) 0808 UTC on 1 June 2015, b) 1208 UTC on 2 June 2015, c) 0808 UTC on 5 July 2015.

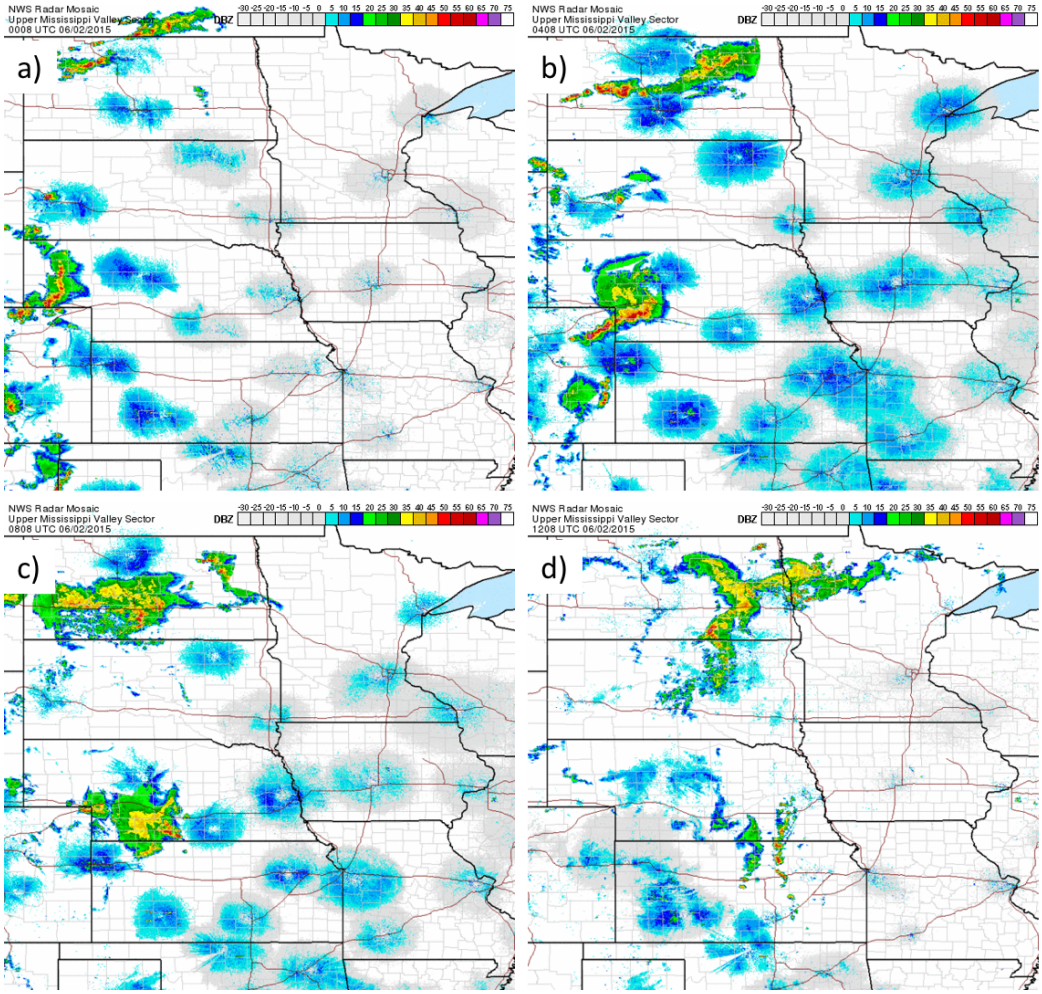

Figure 3. Mosaic 1 km radar reflectivity on 2 June 2015 at: a) 0008 UTC, b) 0408 UTC 2015, c) 0808 UTC, d) 1208 UTC.

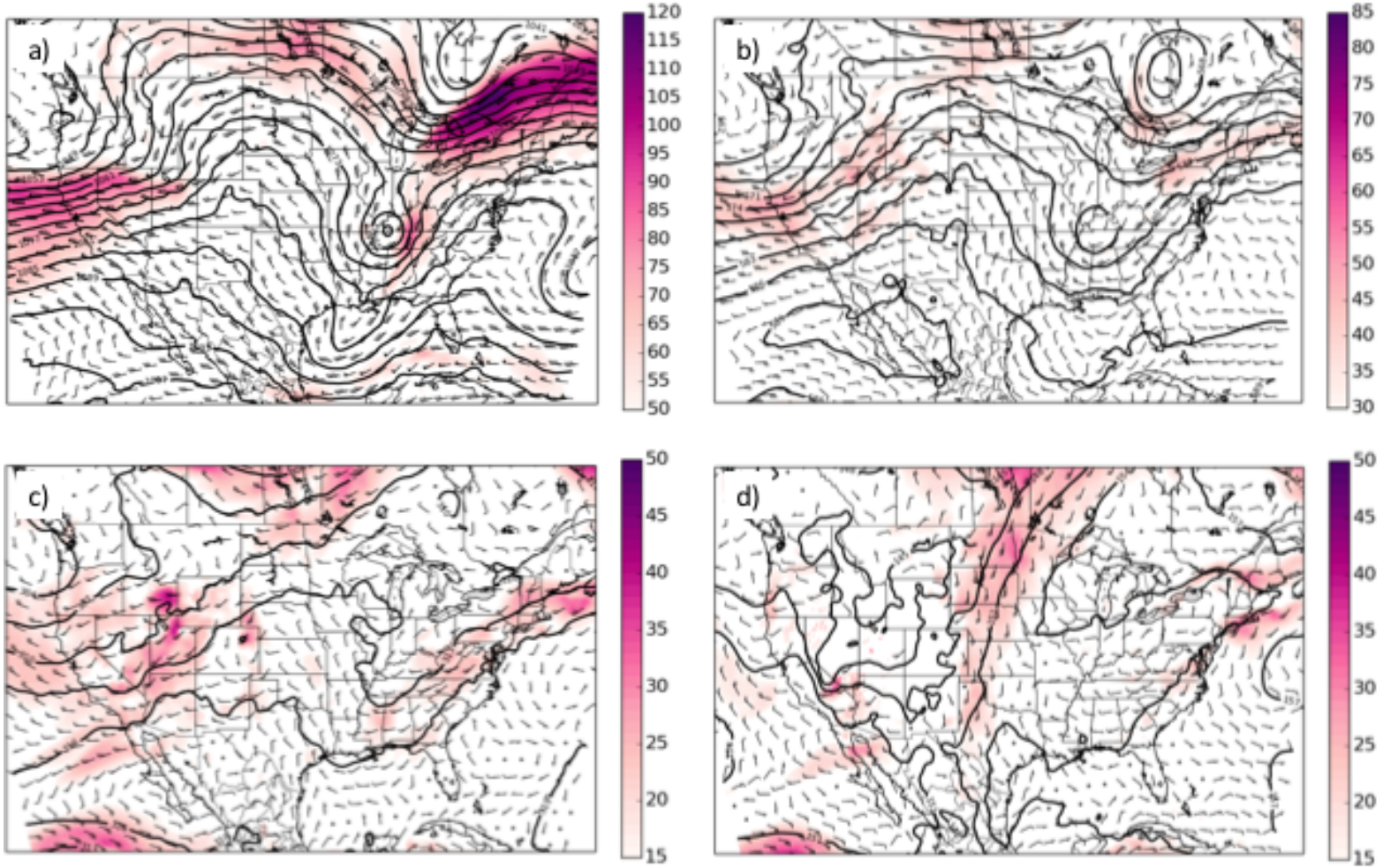

Figure 4. RAP analysis upper air maps from 00 UTC 2 June 2015 at the following pressure levels: a) 250 hPa, b) 500 hPa, c) 700 hPa, d) 850 hPa. Geopotential height (dam) is contoured in black. Wind speed (kts) is shaded.

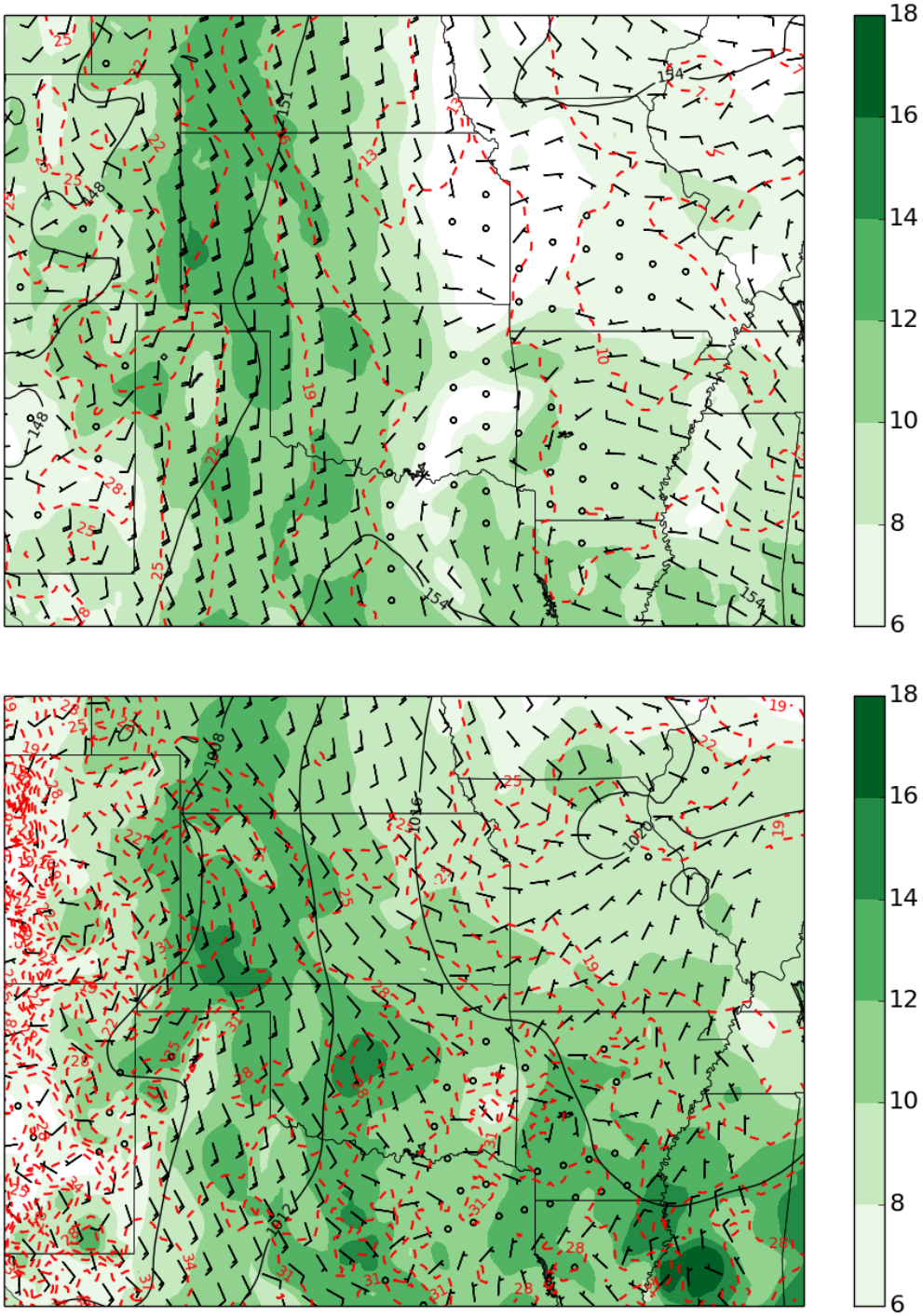

Figure 5. Temperature (°C, red dashed), specific humidity greater than 6 g/kg (green filled contour) and geopotential height (top, black contour) or mean sea level pressure (bottom, black contour) for 850 hPa (top) and the surface (bottom) over the Great Plains region from the 00 UTC RAP analysis on 2 June 2015.

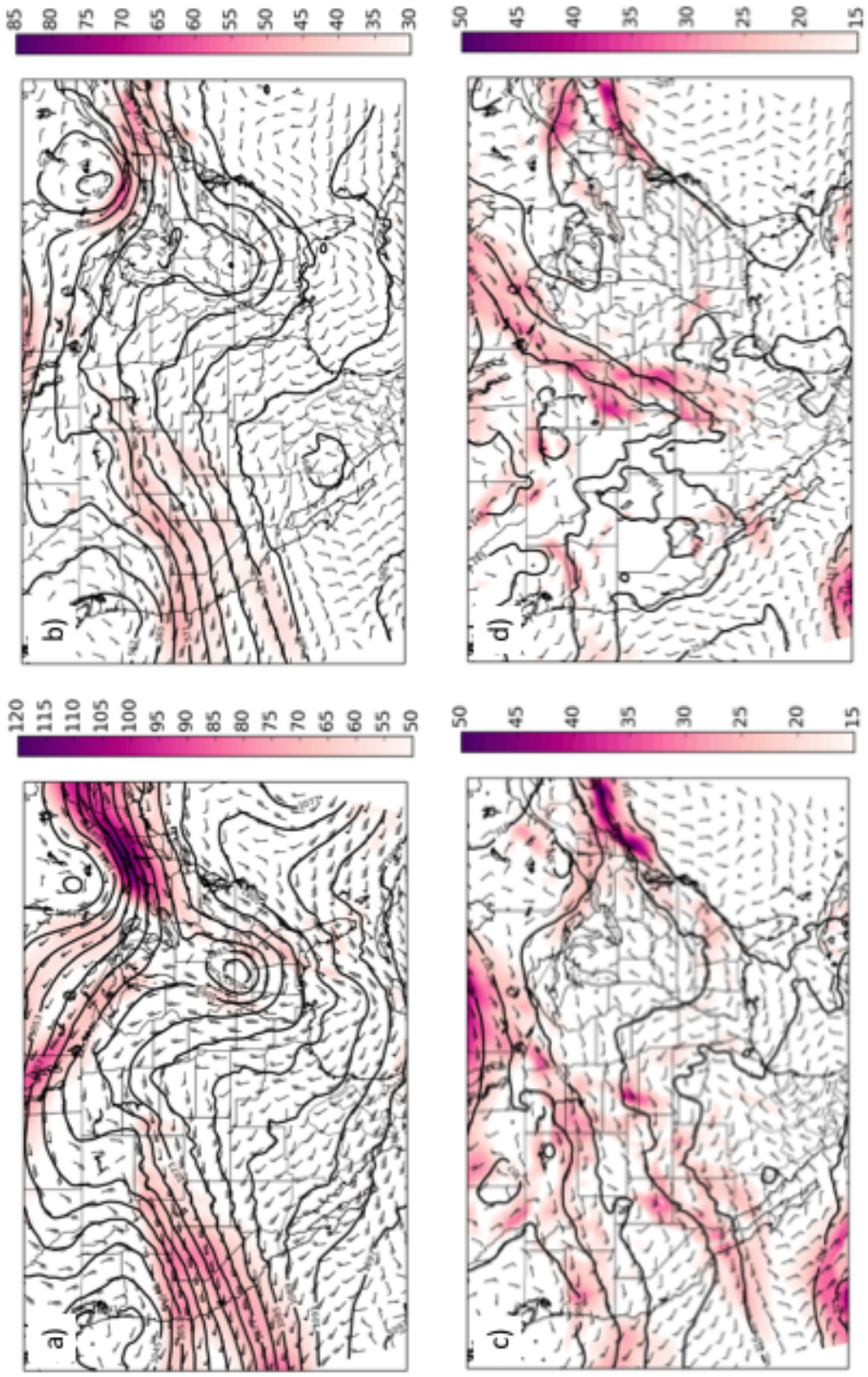

Figure 6. Same as Fig. 4, but for 12 UTC.

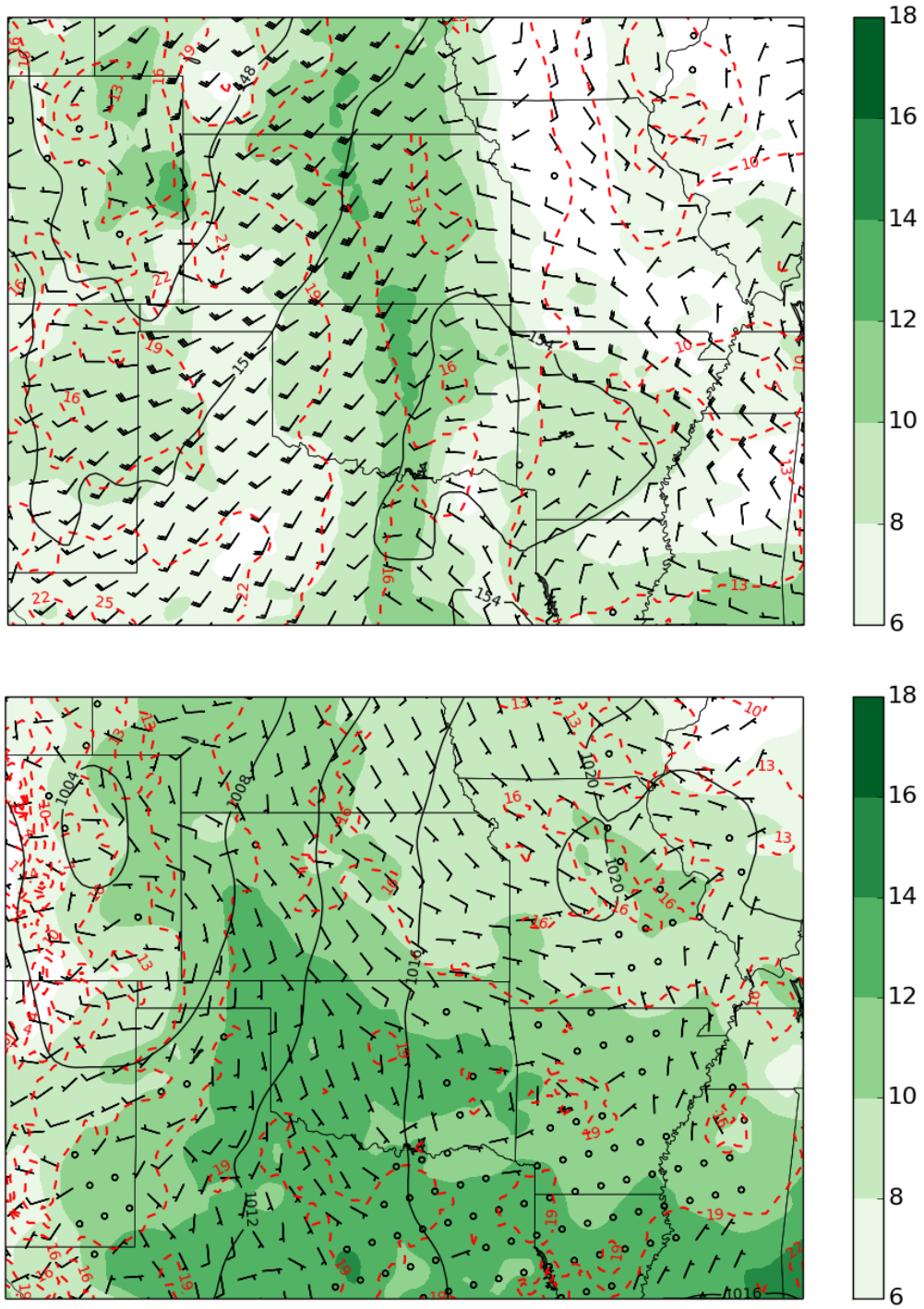

Figure 7. Same as Fig. 5, but for 12 UTC.

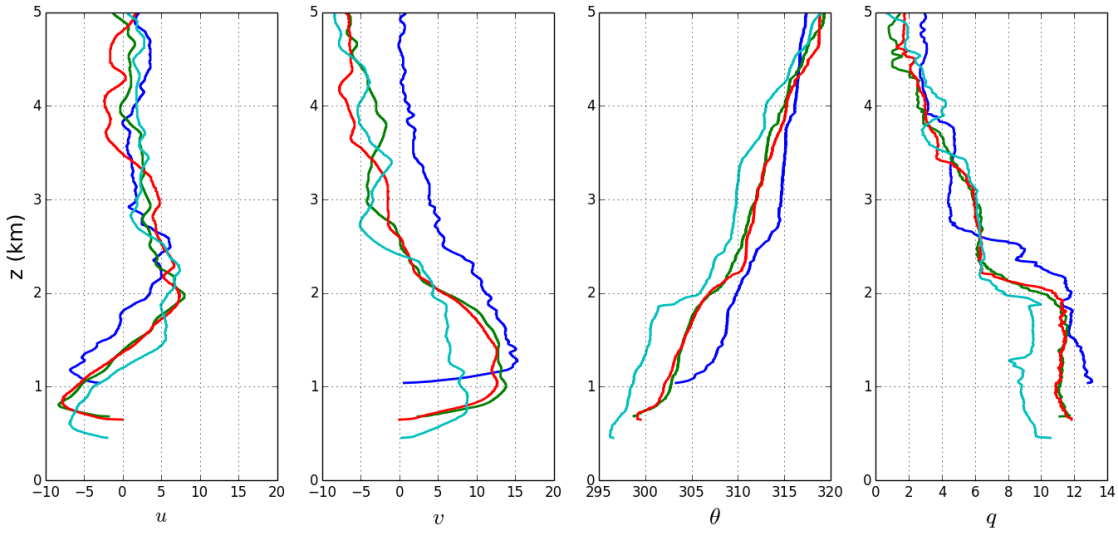

Figure 8. Profiles of *U*, *V*, potential temperature, and specific humidity, from the 0300 UTC soundings at FP-5 (blue), FP-2 (green), FP-3 (red), and FP-6 (teal). The heights are heights ASL.

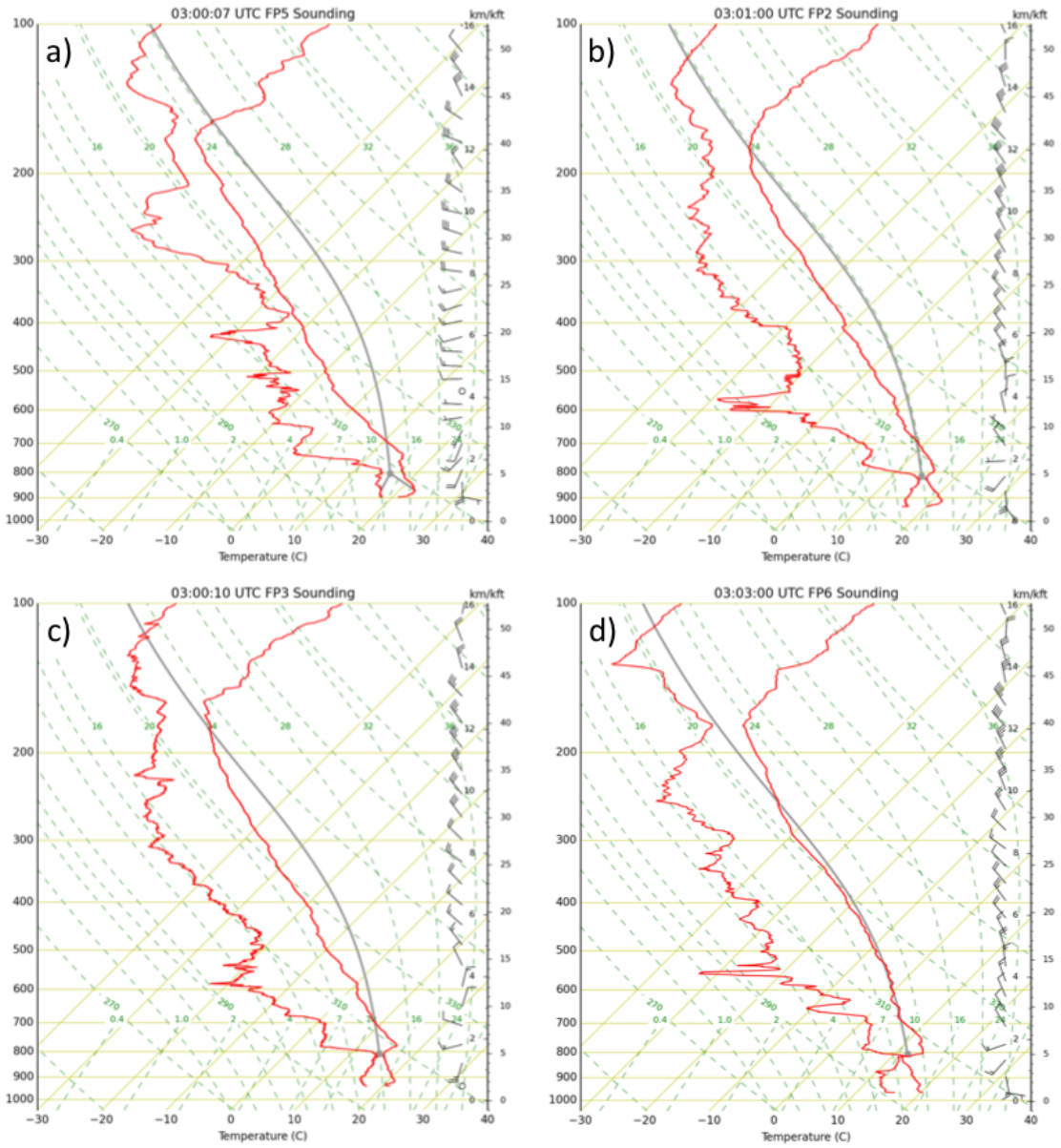

Figure 9. Skew-T diagrams for the 0300 UTC soundings on 2 June 2015 at a) FP-5, b) FP-2, c) FP-3, d) FP-6. The gray line represents the most unstable parcel.

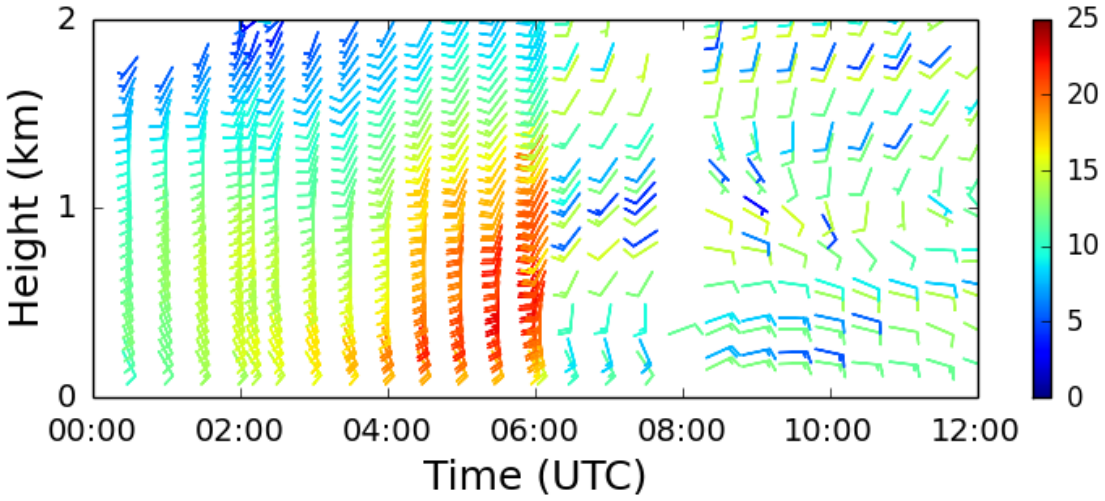

Figure 10. Wind profile time series for 2 June 2015 from the 915 MHz wind profiler at FP-5. Wind speeds are in m s^{-1}.

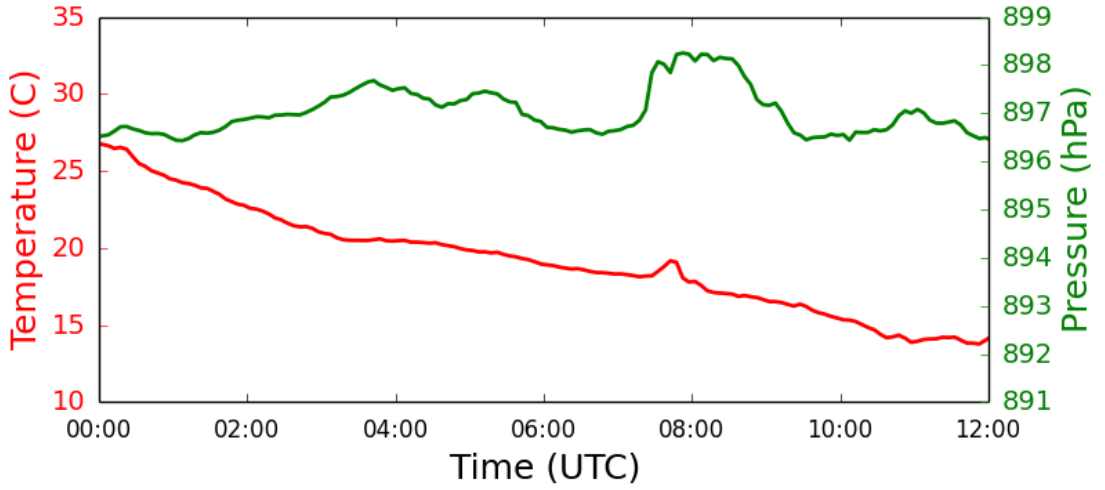

Figure 11. FP-5 surface temperature (red) and surface pressure (green) for 2 June 2015.

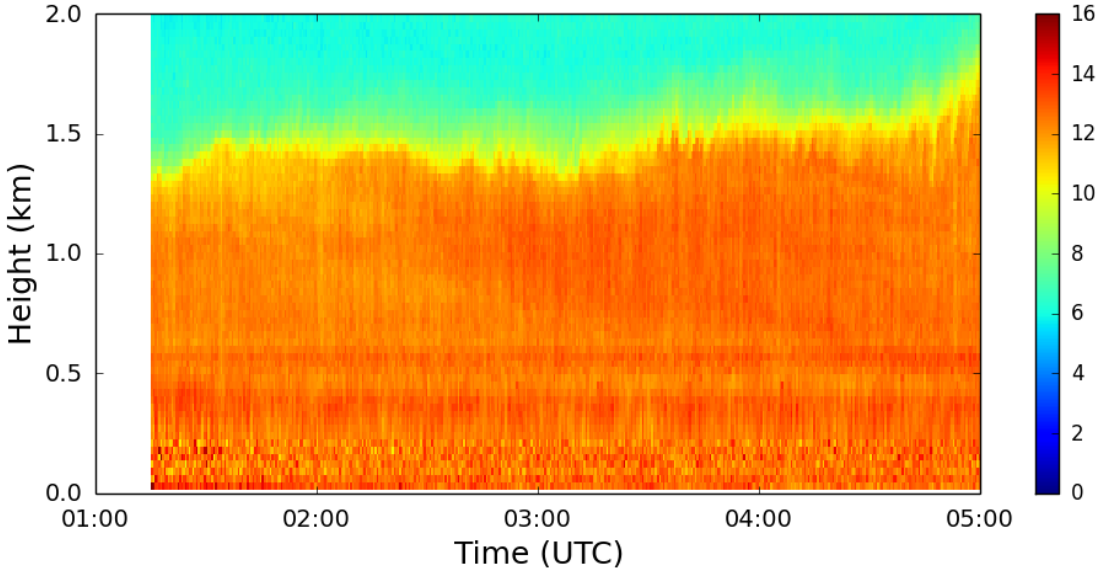

Figure 12. Water vapor mixing ratio (g/kg) time series on 2 June 2015 from the ALVICE Ramen lidar at FP-2.

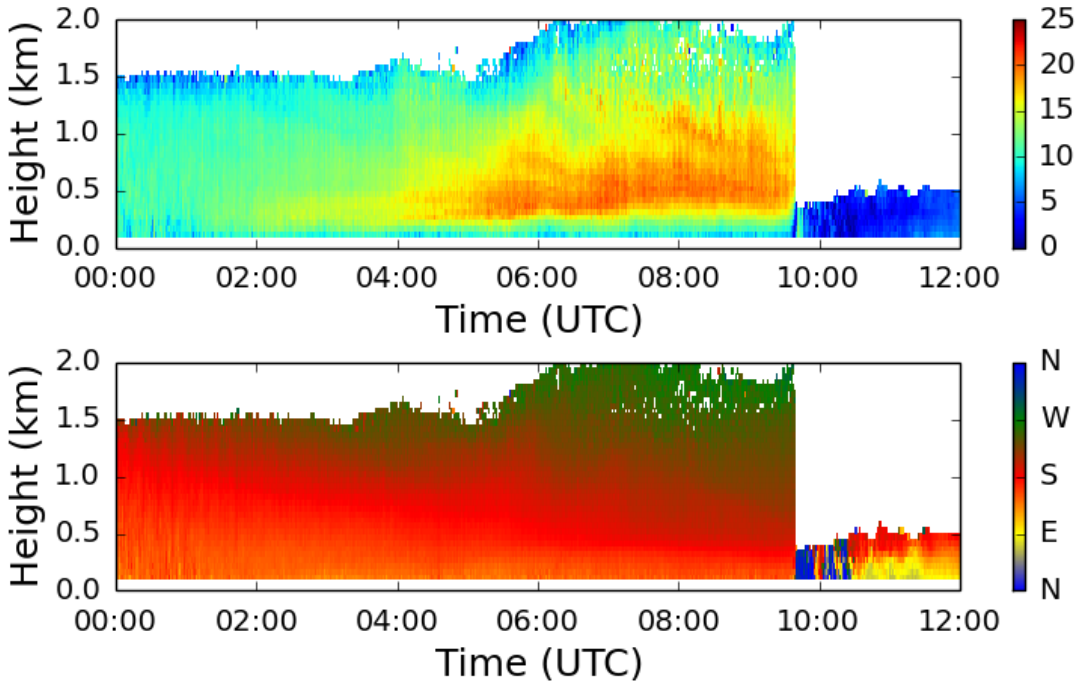

Figure 13. Wind profile time series for 2 June 2015 from the Doppler lidar at FP3. Top panel is wind speed in m s^{-1} and bottom panel is wind direction.

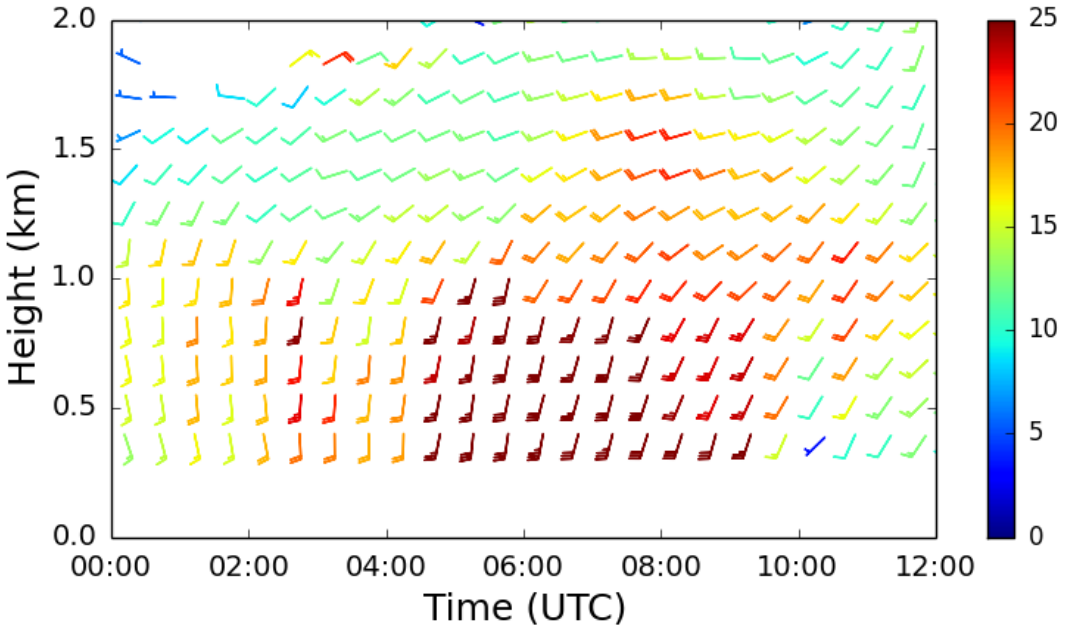

Figure 14. Wind profile time series from the 449 MHz wind profiler at FP-3. Wind speeds are in m s^{-1}.

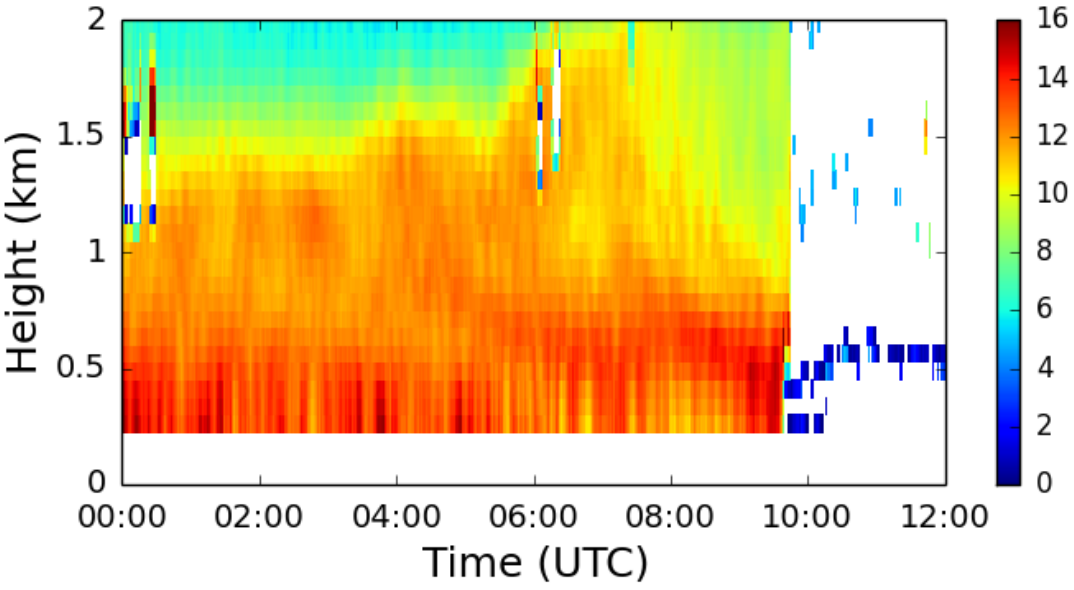

Figure 15. Water vapor profile time series from the water vapor DIAL at FP-3 for 2 June 2015. Values are g m^{-3}.

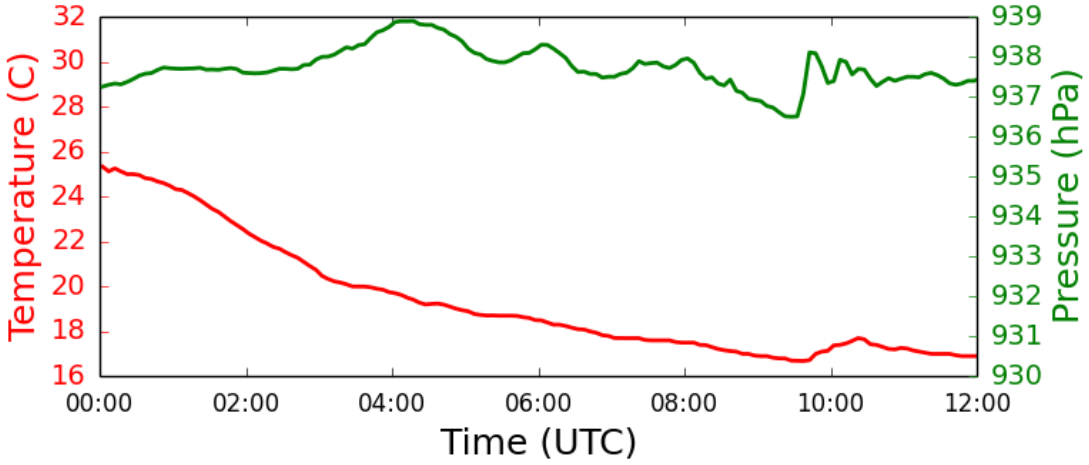

Figure 16. Same as Fig. 11, but for FP-3.

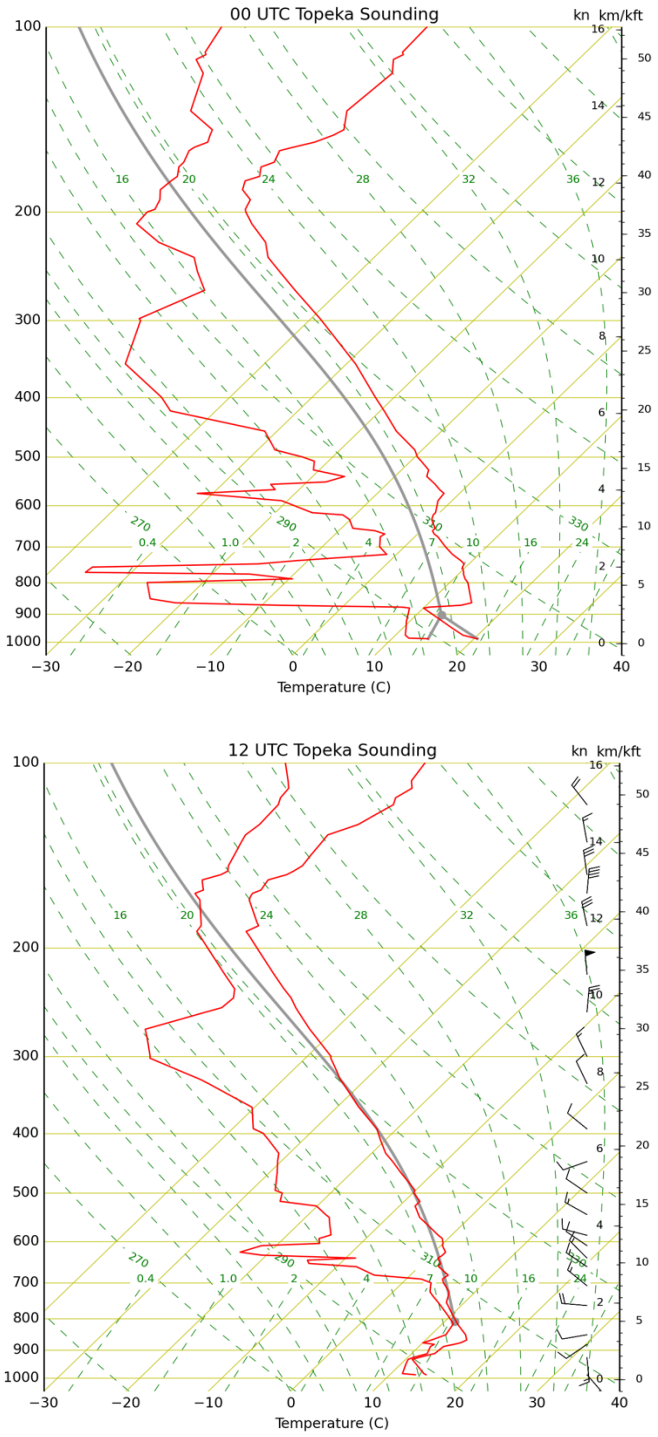

Figure 17. The 00 (top) and 12 (bottom) UTC soundings for 2 June 2015 at Topeka, KS. The gray line represents the most unstable parcel.

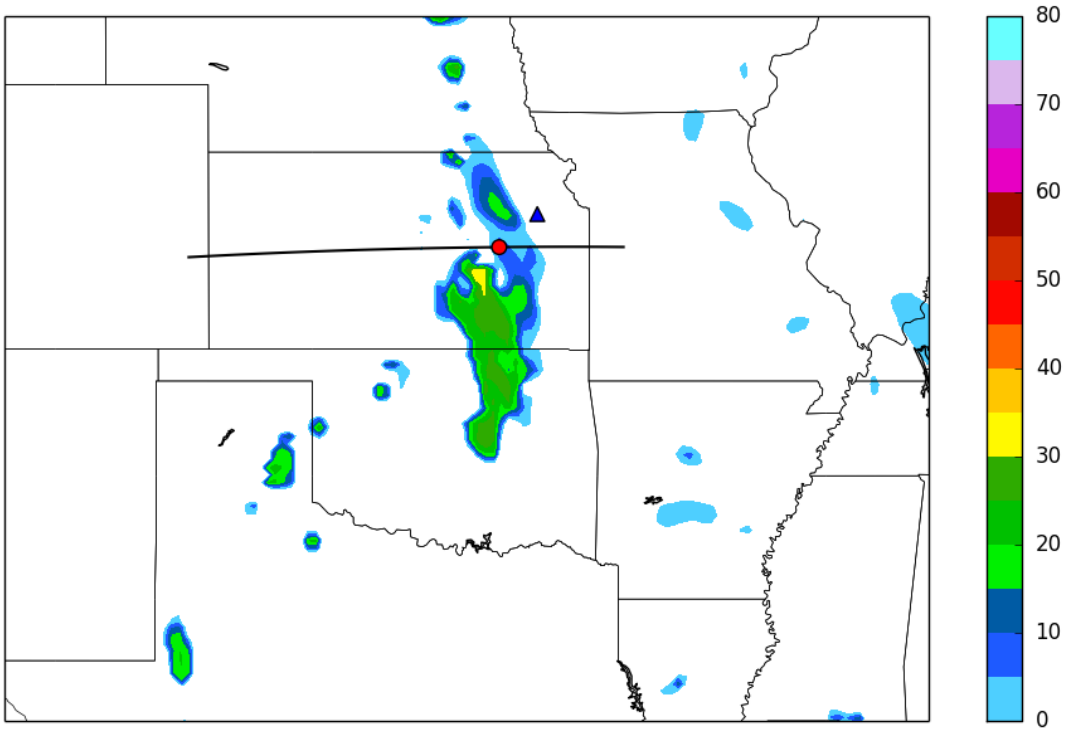

Figure 18. Simulated composite reflectivity valid for 12 UTC on 2 June 2015 from the 00 UTC RAP forecast. The black line indicates where the cross-sections were taken. The red circle is the location where the model soundings were taken from. The blue triangle shows the location of Topeka, KS.

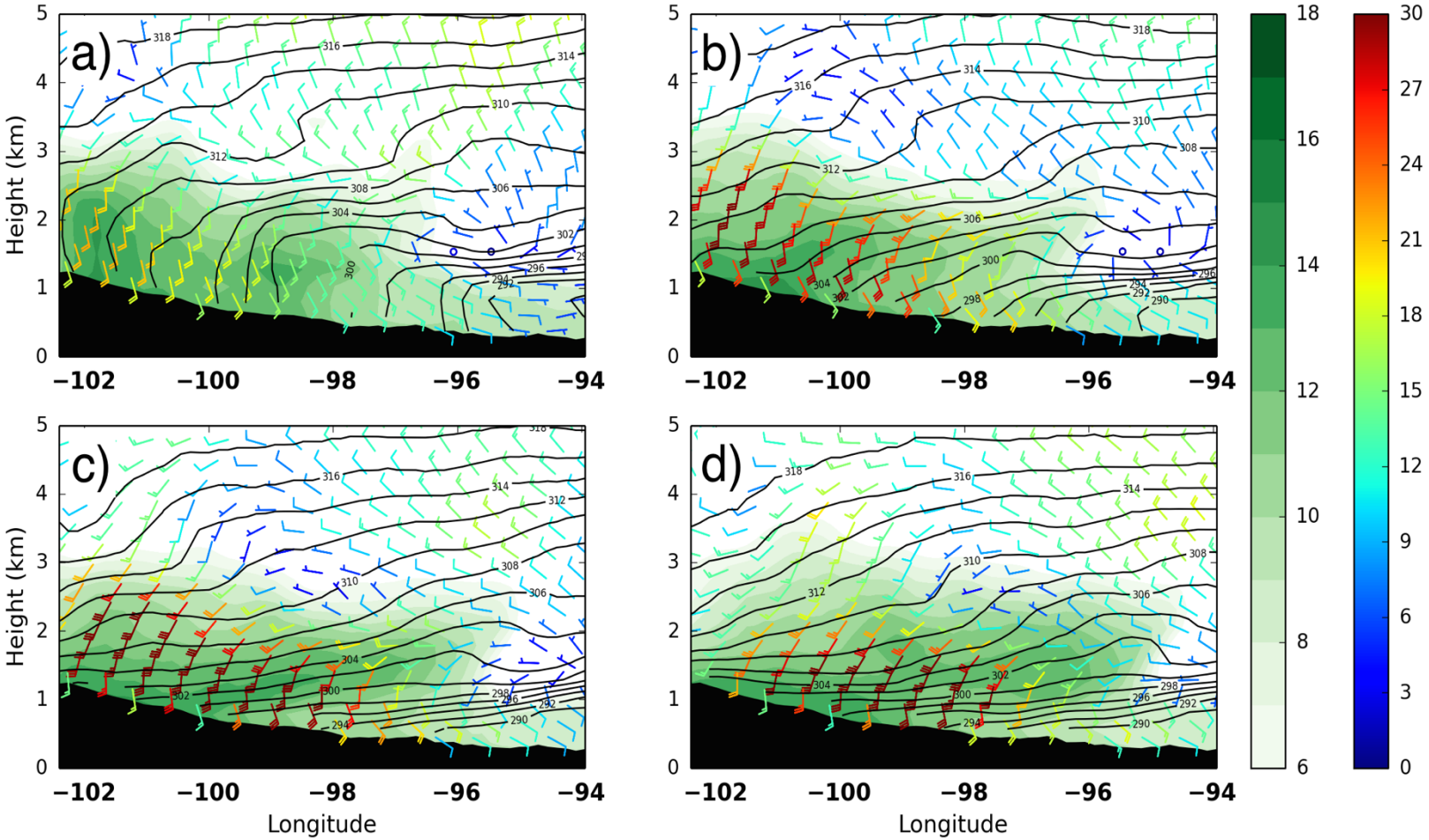

Figure 19. Cross-sections of the 2 June 2015, 00 UTC RAP forecast valid for a) 00, b) 04, c) 06, and d) 12 UTC. Potential temperature (K) is contoured in black. Specific humidity greater than 6 g kg^{-1} is shaded in green. Wind speeds are in knots.

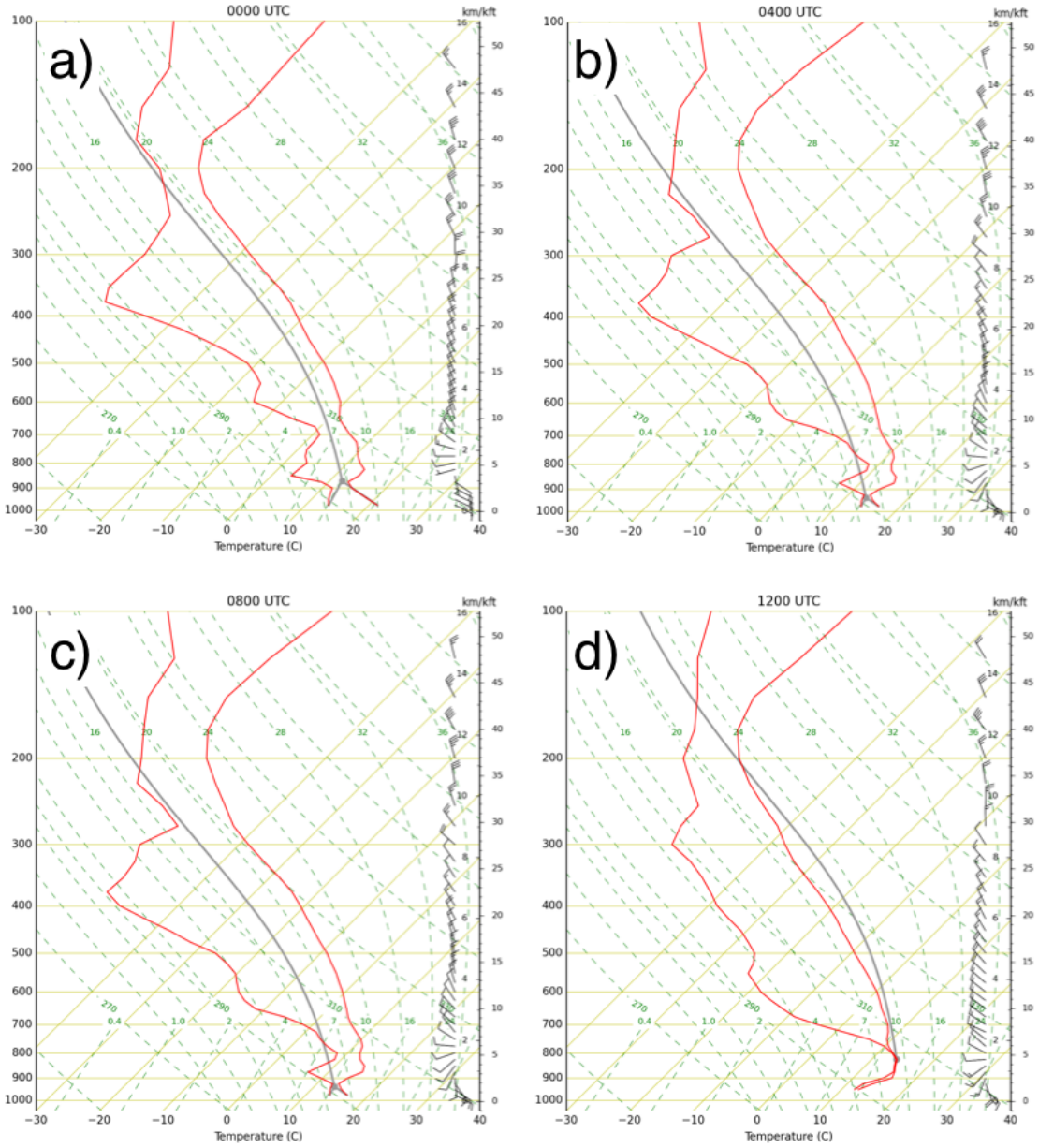

Figure 20. 00 UTC RAP forecast soundings valid for 2 June 2015 valid for a) 00, b) 04, c) 08, and d) 12 UTC. The gray line represents the most unstable parcel.

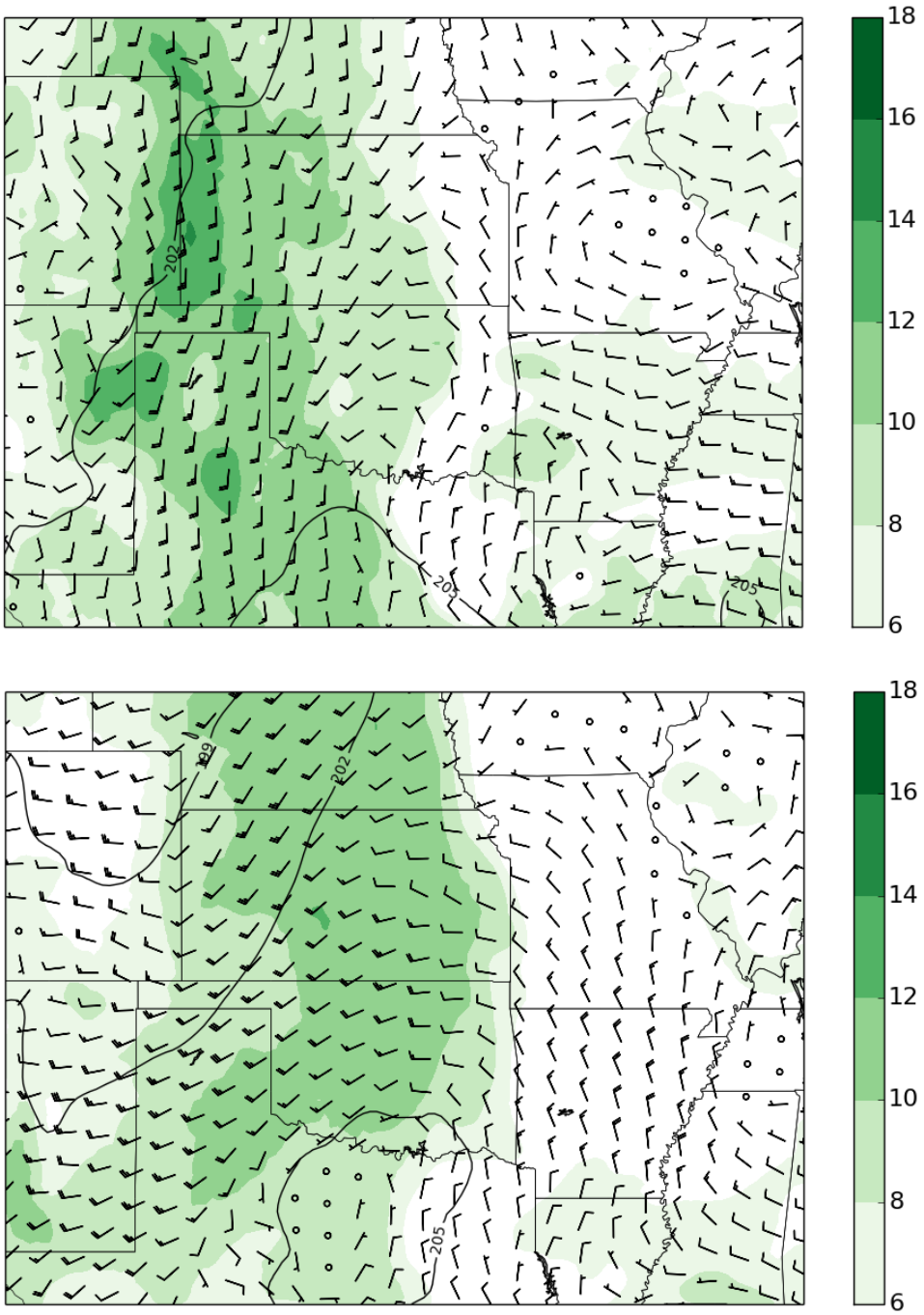

Figure 21. The 00 UTC RAP 800 hPa forecast for 2 June 2015 valid for 00 (top) and 12 (bottom) UTC. Geopotential height is contoured in black. Specific humidity greater than 6 g kg^{-1} is shaded green. Wind speeds are in knots.

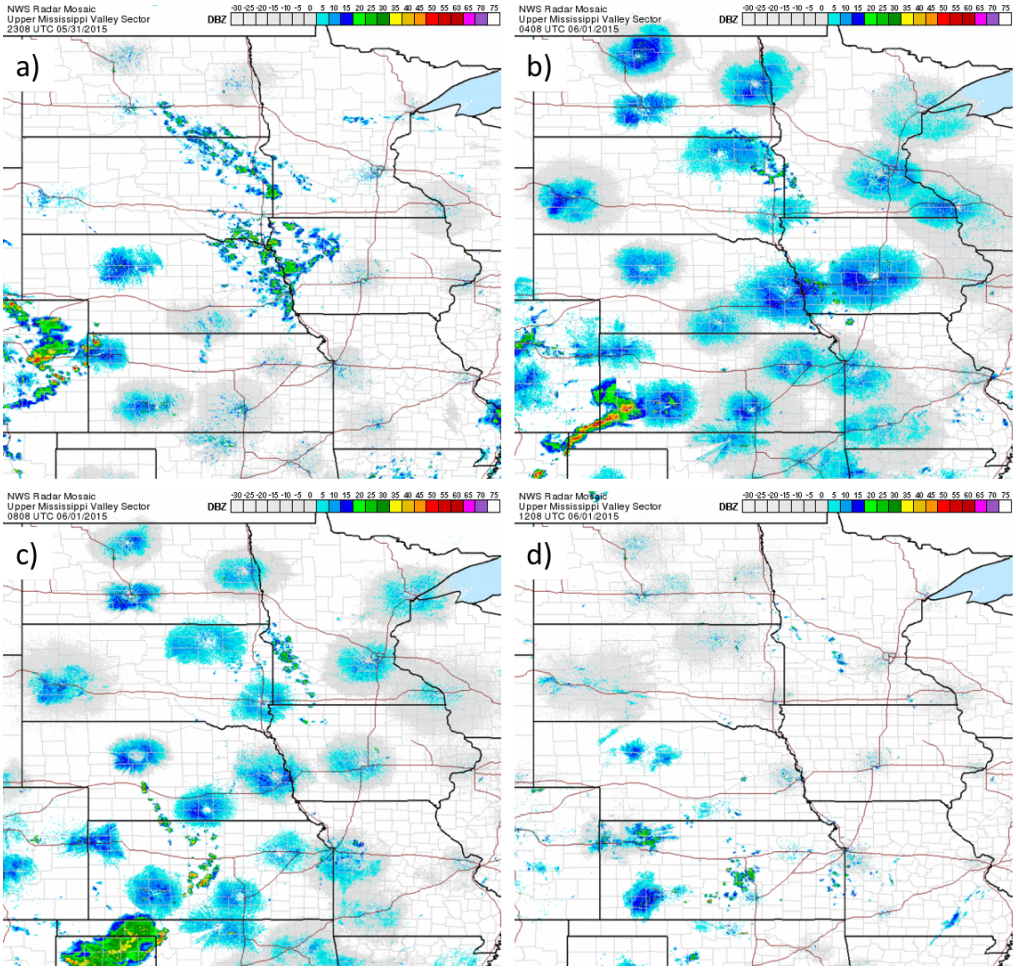

Figure 22. Mosaic 1 km radar reflectivity on 1 June 2015 at: a) 0008 UTC, b) 0408 UTC, c) 0808 UTC, d) 1208 UTC.

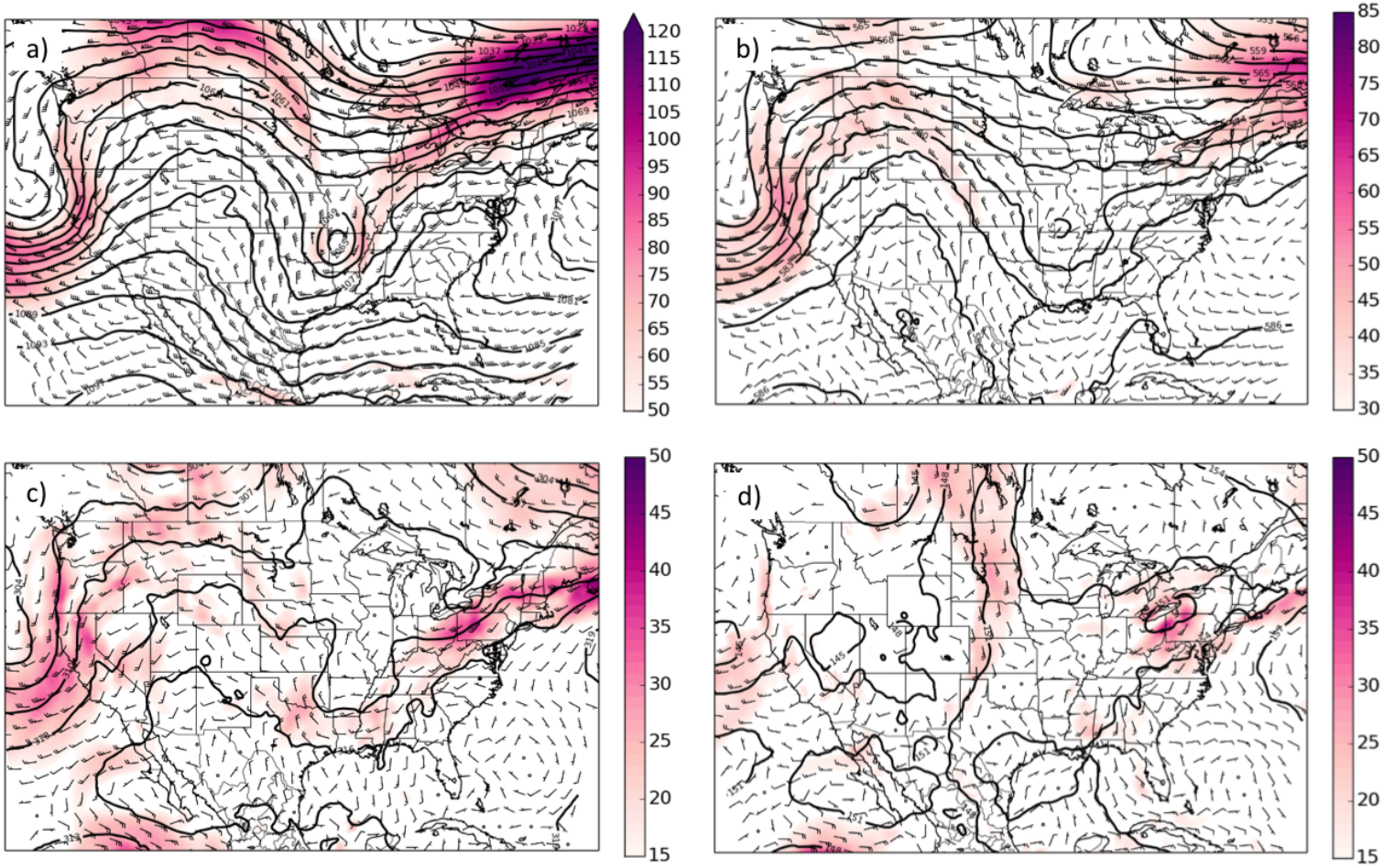

Figure 23. Same as Fig. 4, but for 1 June 2015 at 00 UTC.

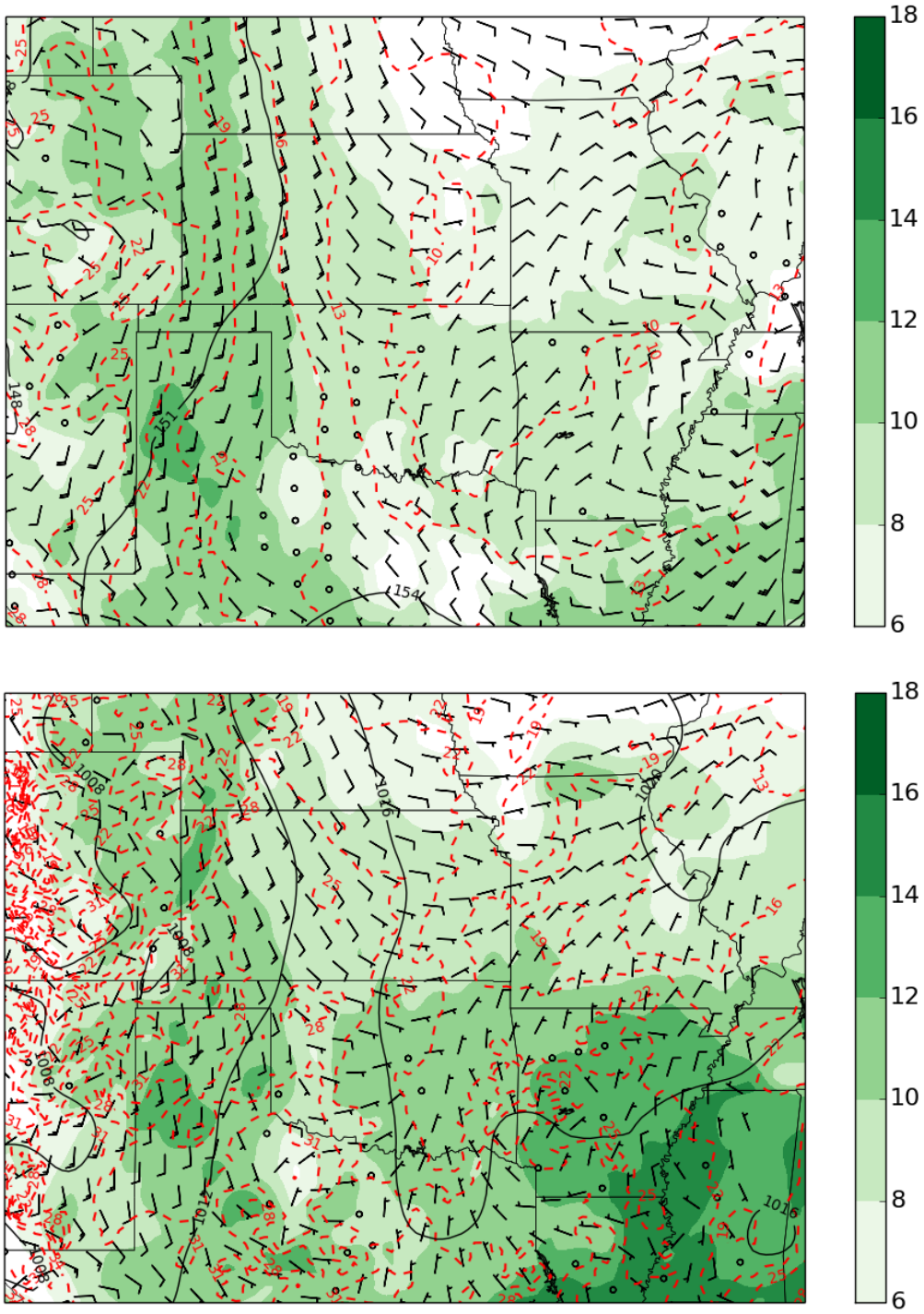

Figure 24. Same as Fig. 5, but for 00 UTC on 1 June 2015.

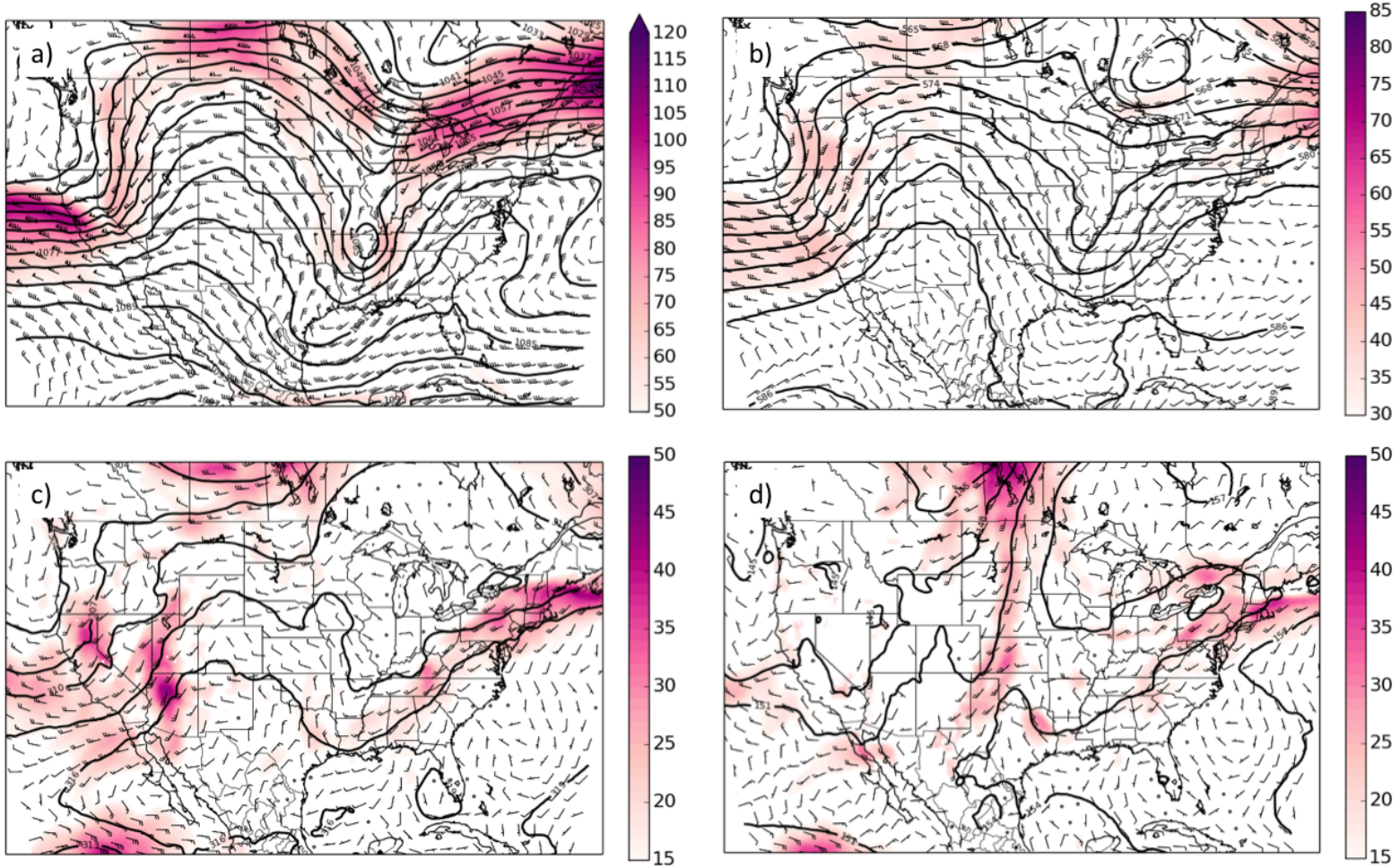

Figure 25. Same as Fig. 4, but for 1 June 2015 at 12 UTC.

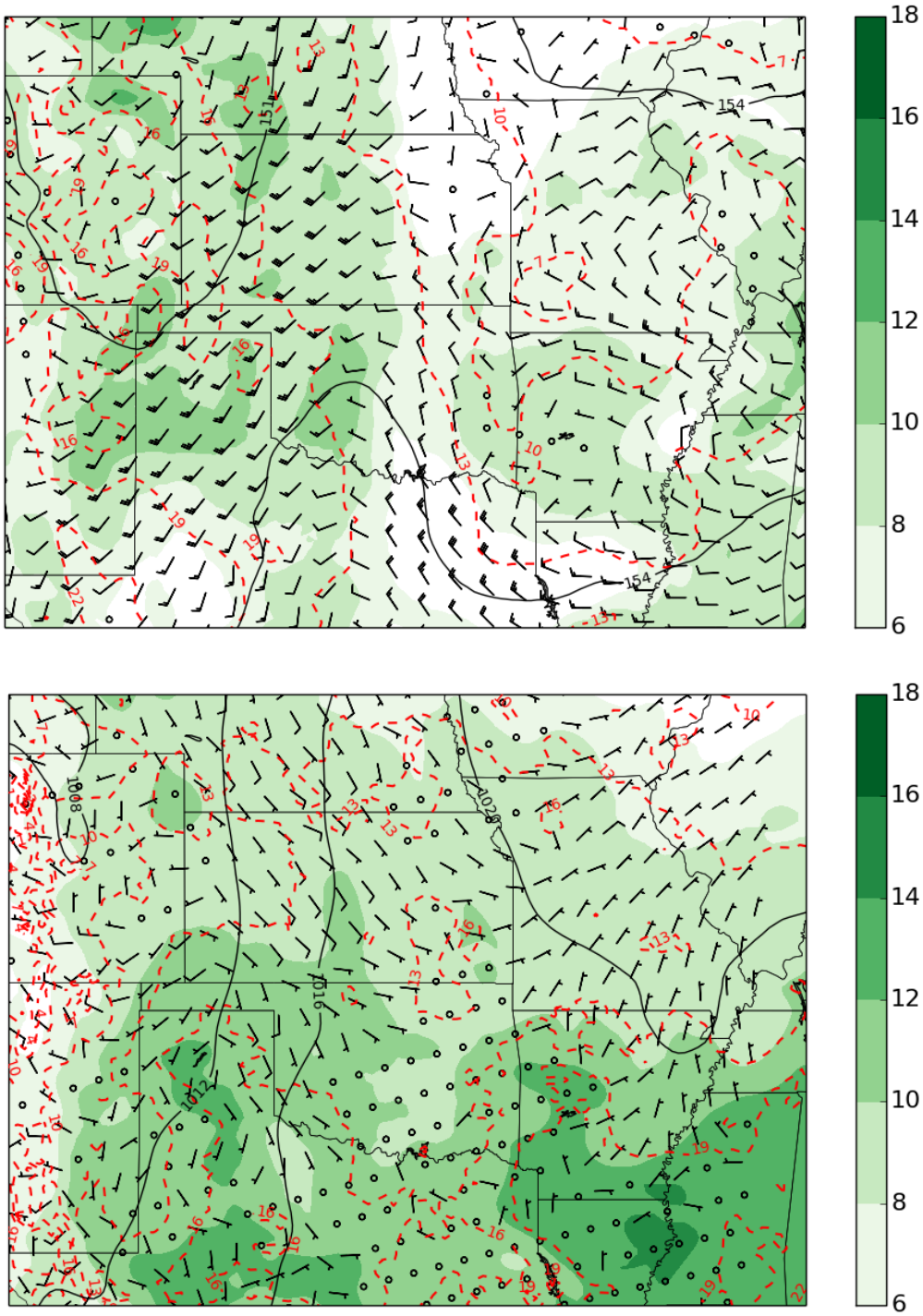

Figure 26. Same as Fig. 5, but for 12 UTC on 1 June 2015.

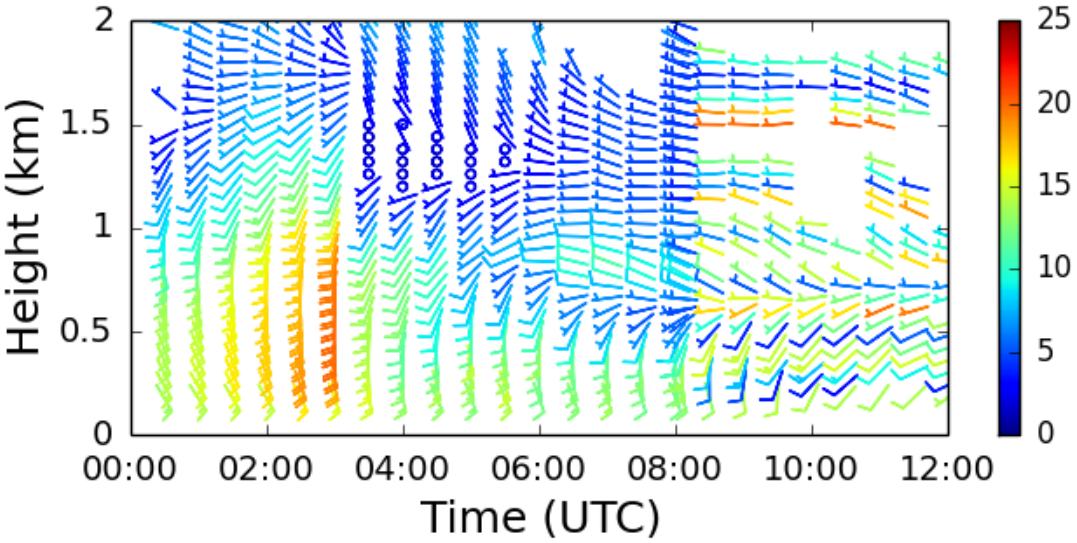

Figure 27. Wind profile time series for 1 June 2015 from the 915 MHz wind profiler at FP-5. Wind speeds are in m s^{-1}.

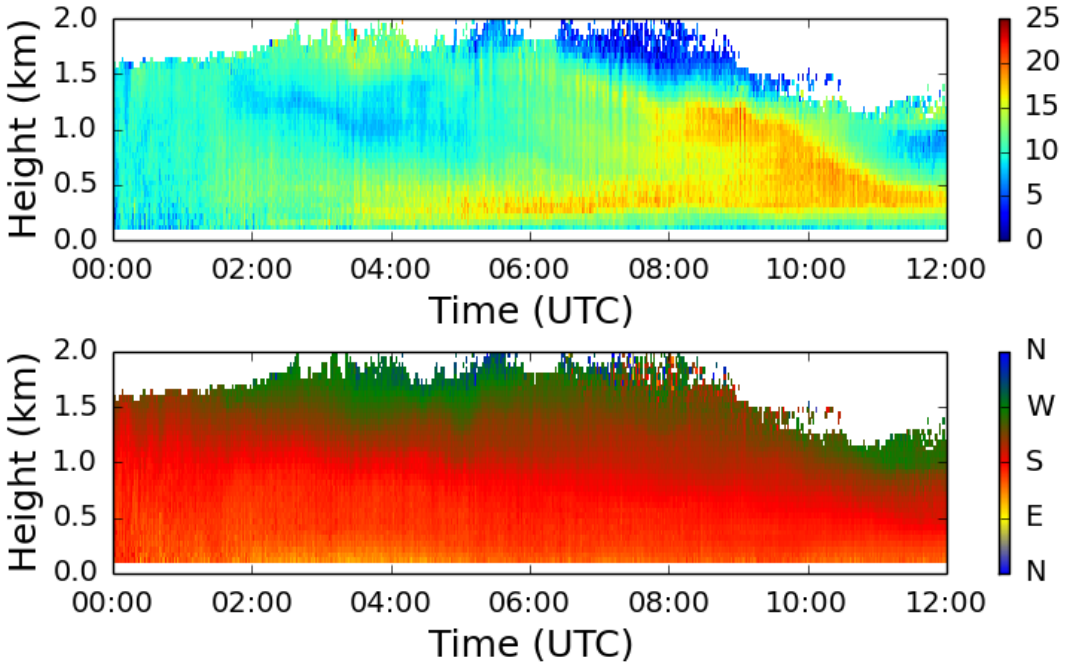

Figure 28. Wind profile time series for 1 June 2015 from the Doppler lidar at FP3. Top panel is wind speed in m s^{-1} and bottom panel is wind direction.

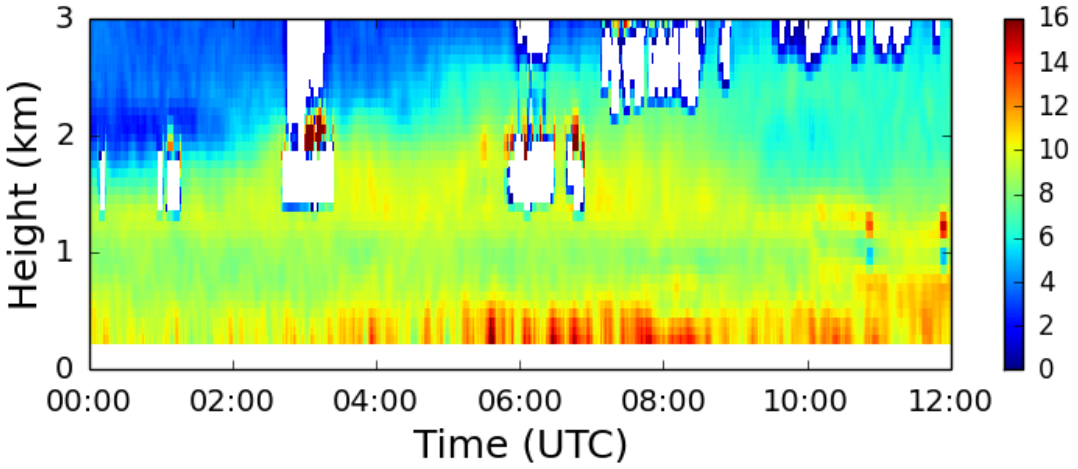

Figure 29. Water vapor profile time series from the water vapor DIAL at FP-3 for 1 June 2015. Values are g m^{-3}.

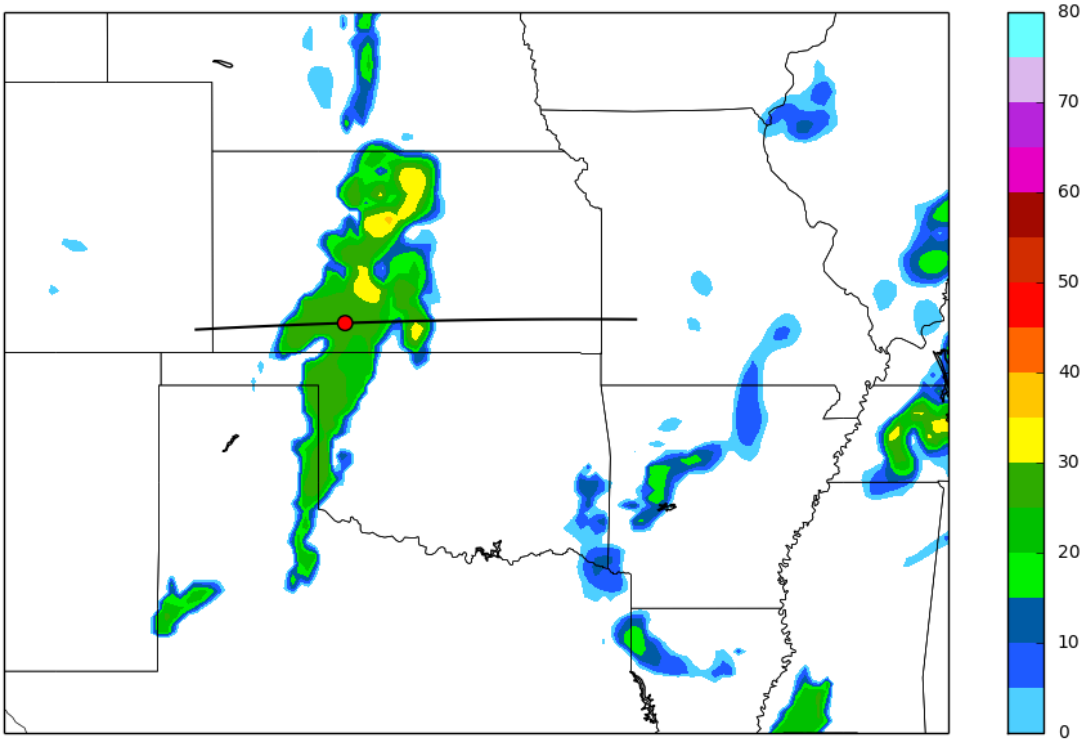

Figure 30. Simulated composite reflectivity valid for 12 UTC on 1 June 2015 from the 00 UTC RAP forecast. The black line indicates where the cross-sections were taken. The red circle is the location where the model soundings were taken from.

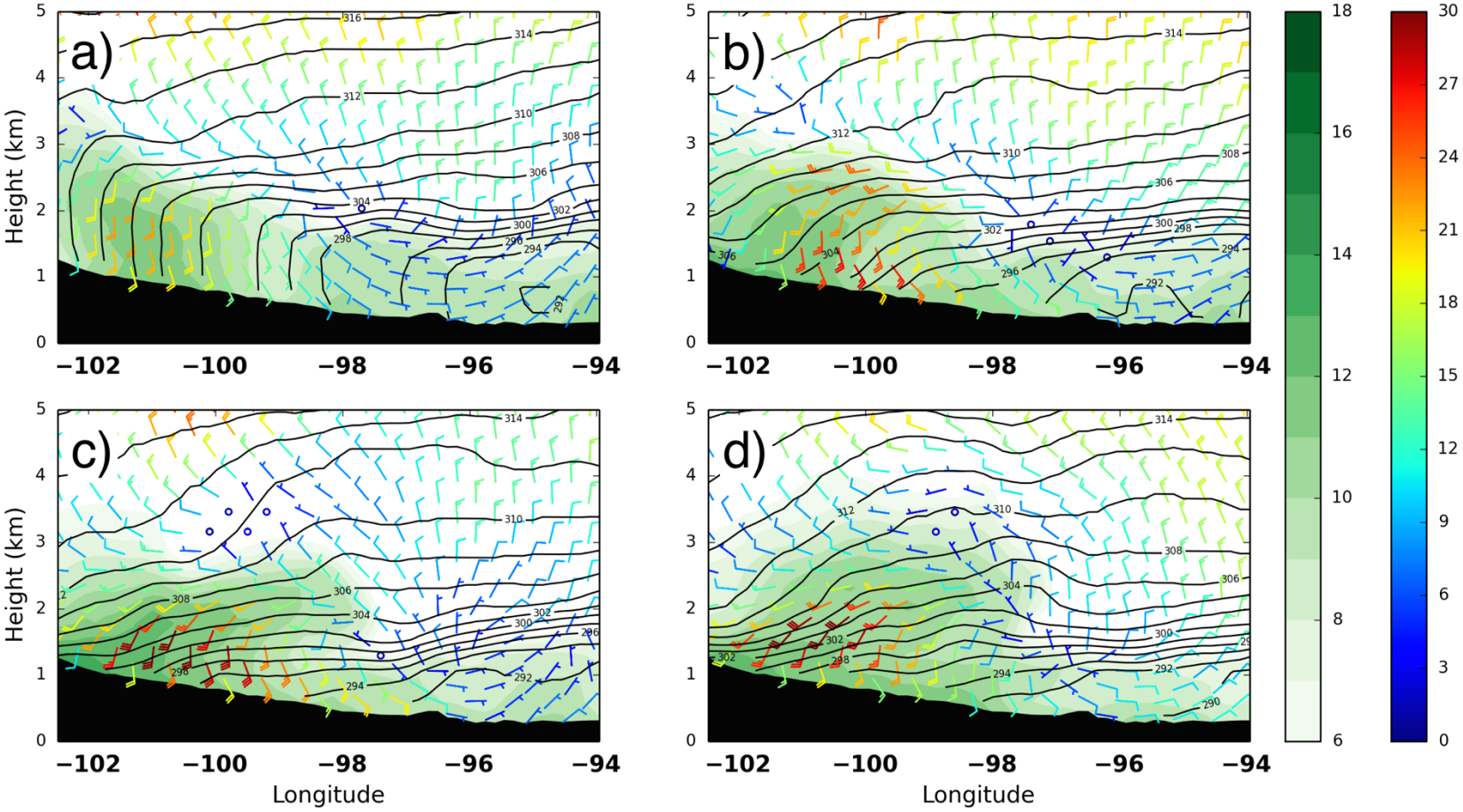

Figure 31. Cross-sections of the 01 June 2015, 00 UTC RAP forecast valid for a) 00, b) 04, c) 06, and d) 12 UTC. Potential temperature (K) is contoured in black. Specific humidity greater than 6 g kg^{-1} is shaded in green. Wind speeds are in knots.

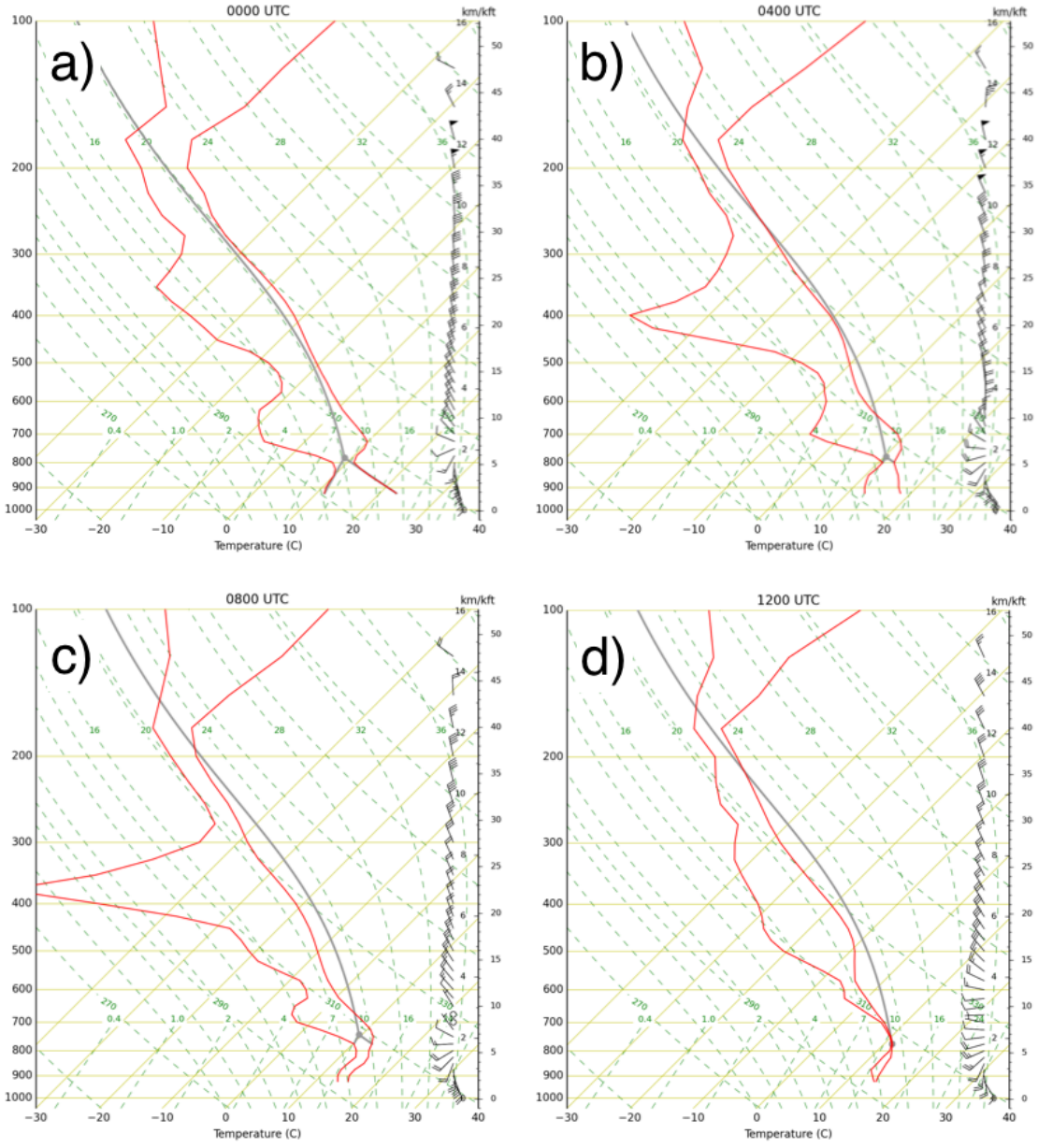

Figure 32. 00 UTC RAP forecast soundings valid for 1 June 2015 valid for a) 00, b) 04, c) 08, and d) 12 UTC. The gray line represents the most unstable parcel.

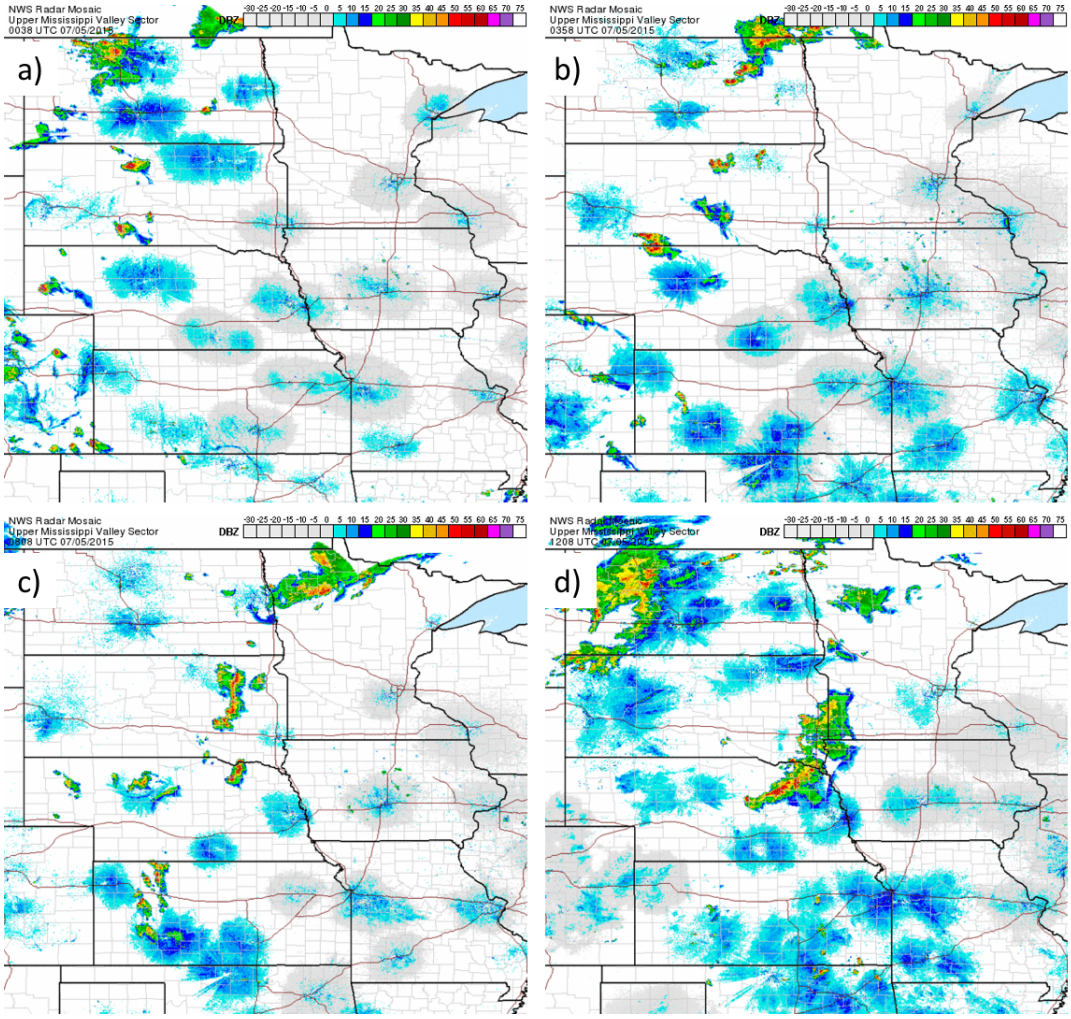

Figure 33. Mosaic 1 km radar reflectivity on 5 July 2015 for: a) 0008 UTC b) 0408 UTC, c) 0808 UTC, d) 1208 UTC.

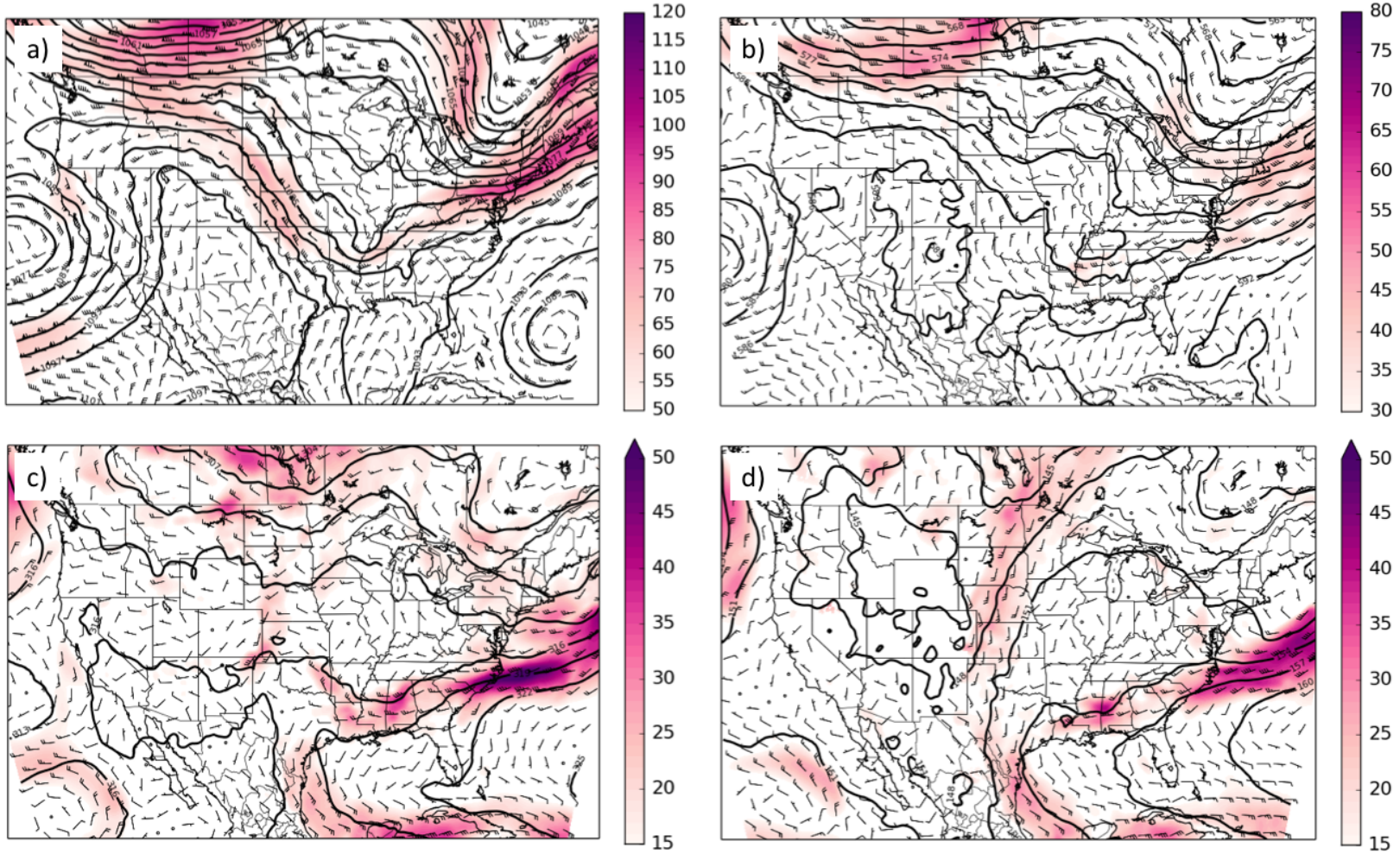

Figure 34. Same as Fig. 4, but for 5 July 2015 at 00 UTC.

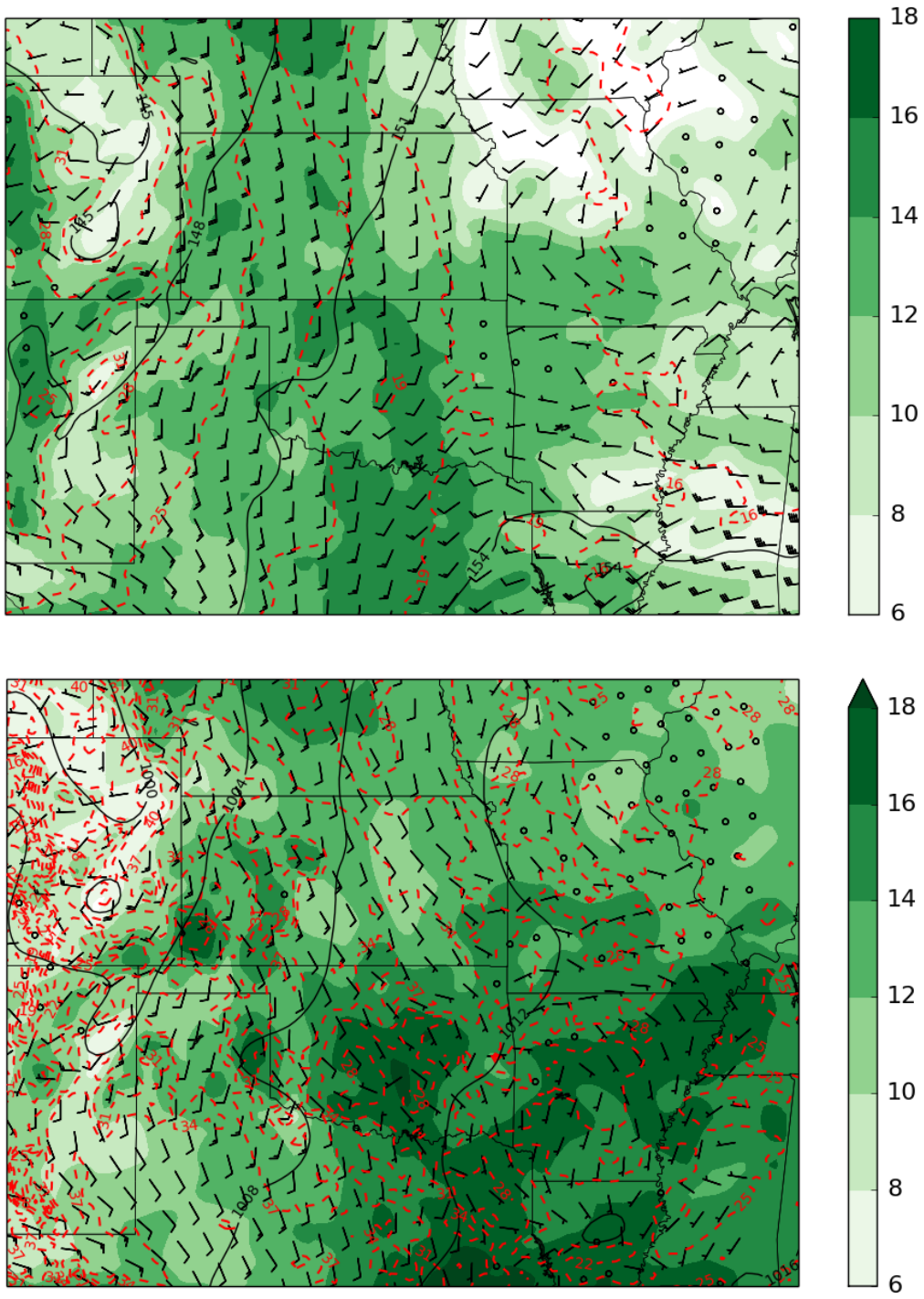

Figure 35. Same as Fig. 5, but for 00 UTC on 5 July 2015.

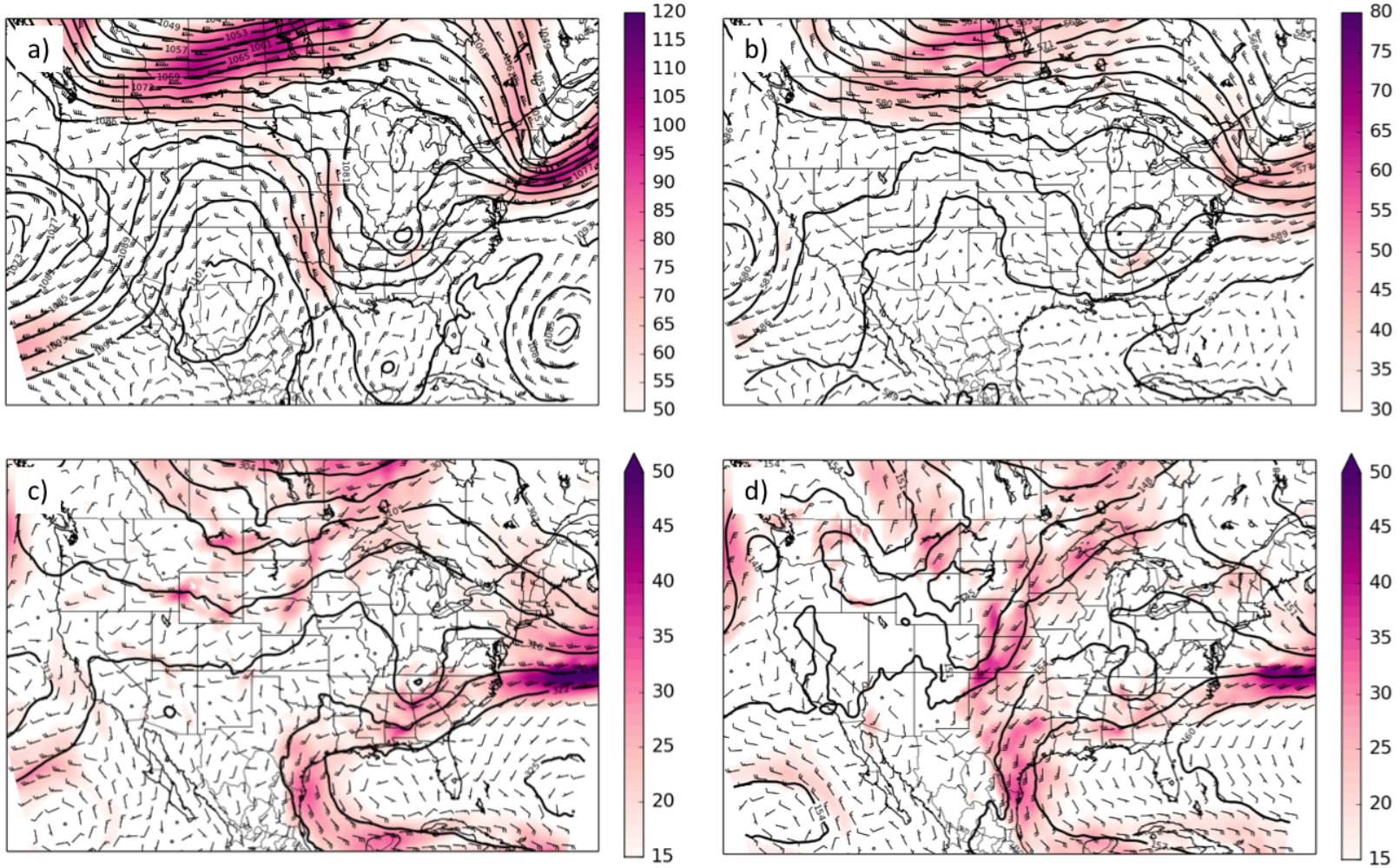

Figure 36. Same as Fig. 4, but for 5 July 2015 at 12 UTC.

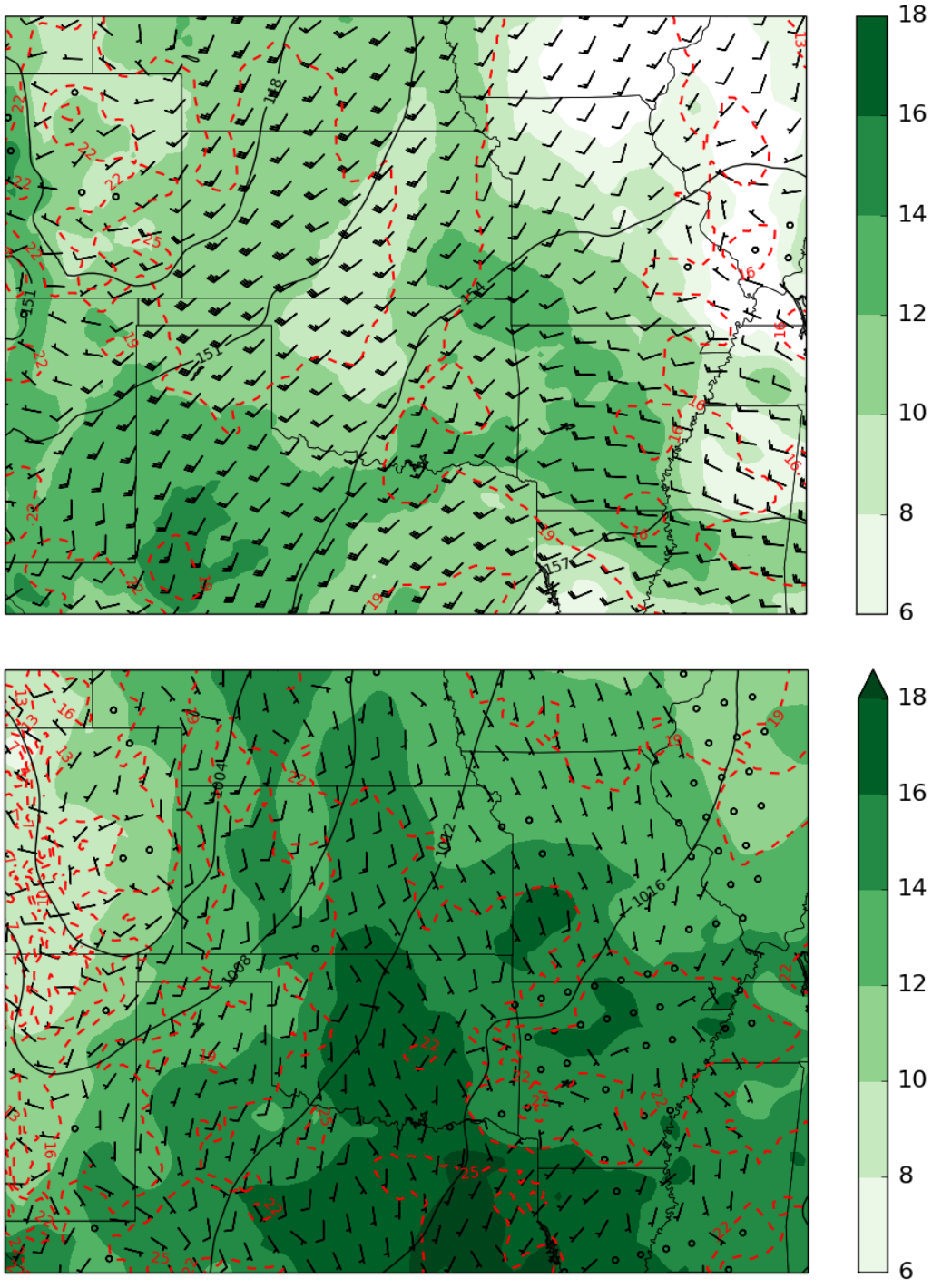

Figure 37. Same as Fig. 5, but for 12 UTC on 5 July 2015.

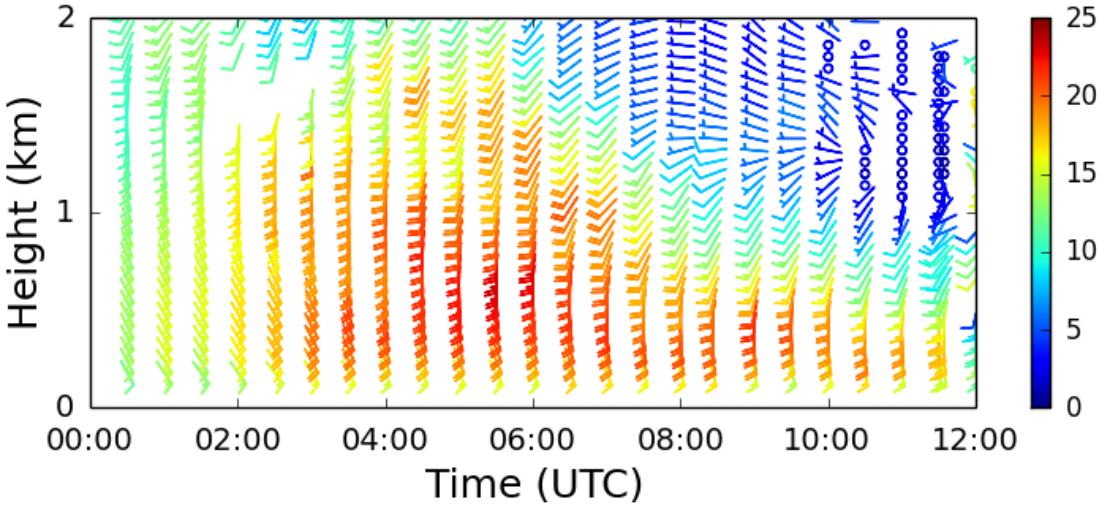

Figure 38. Wind profile time series for 5 July 2015 from the 915 MHz wind profiler at FP-5. Wind speeds are in m s^{-1}.

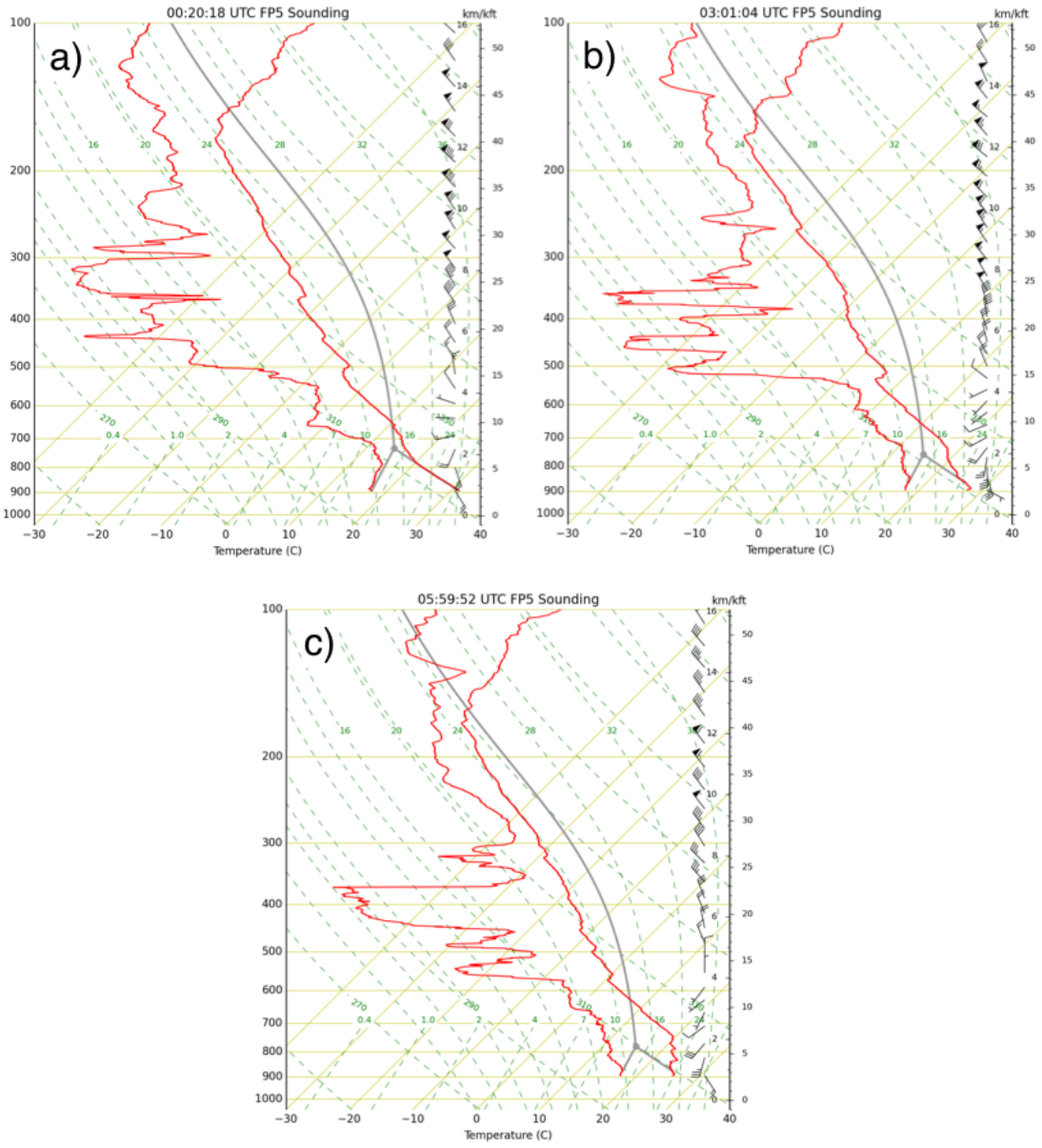

Figure 39. Soundings from FP-5 on 5 July 2015 at a) 0020 UTC, b) 0301 UTC, and c) 0559 UTC. The grey line represents the most unstable parcel.

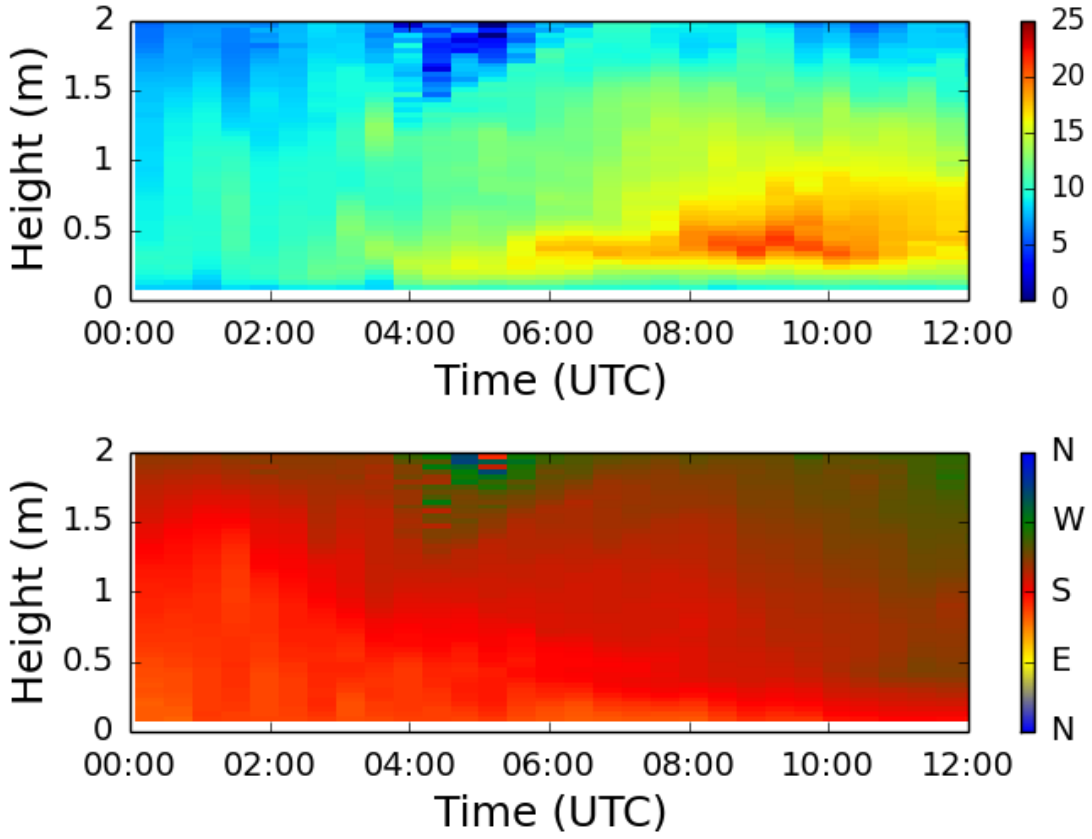

Figure 40. Wind profile time series for 5 July 2015 from the Doppler lidar at FP2. Top panel is wind speed in m s^{-1} and bottom panel is wind direction.

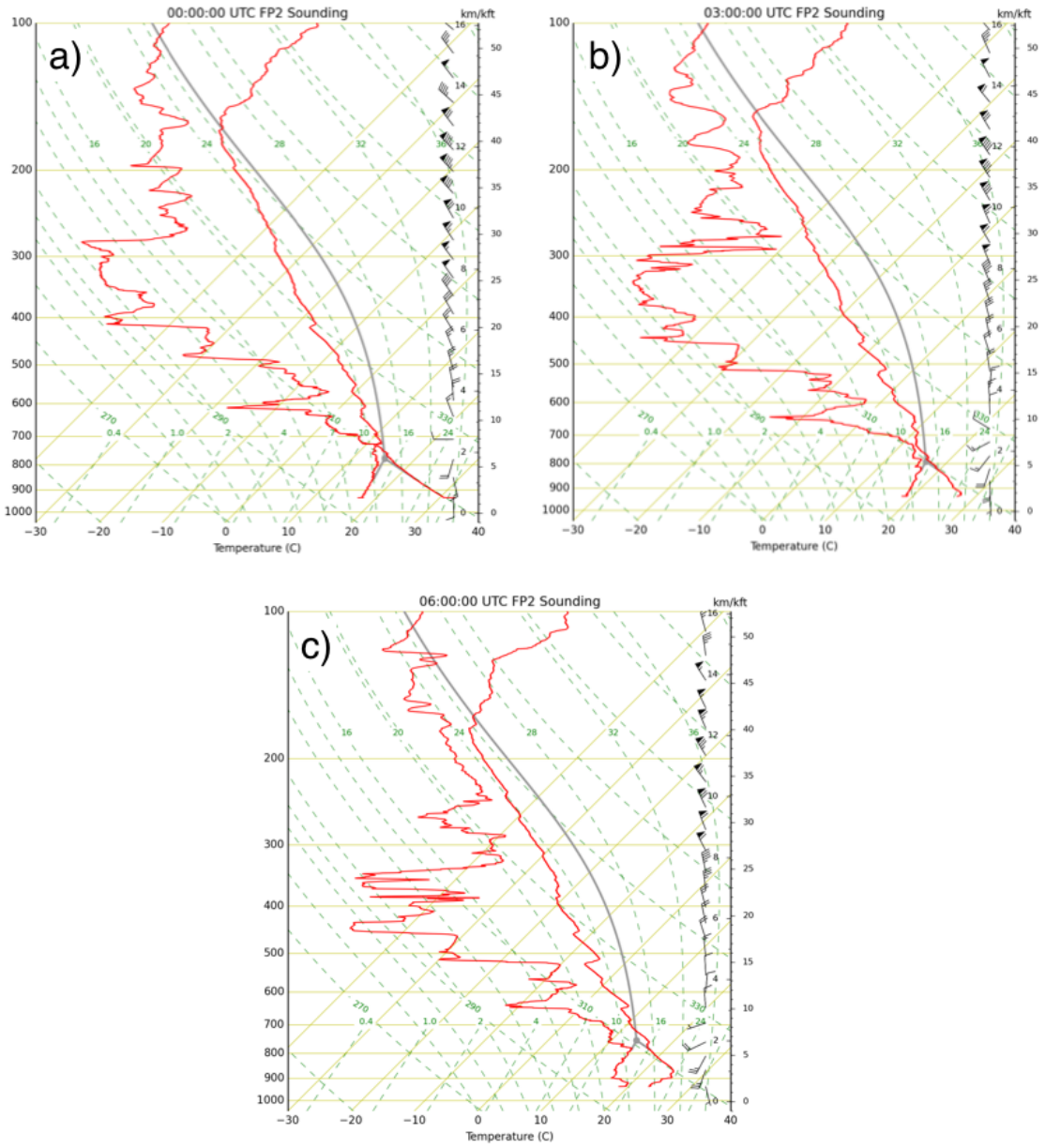

Figure 41. Soundings from FP-2 on 5 July 2015 at a) 0000 UTC, b) 0300 UTC, and c) 0600 UTC. The grey line represents the most unstable parcel.

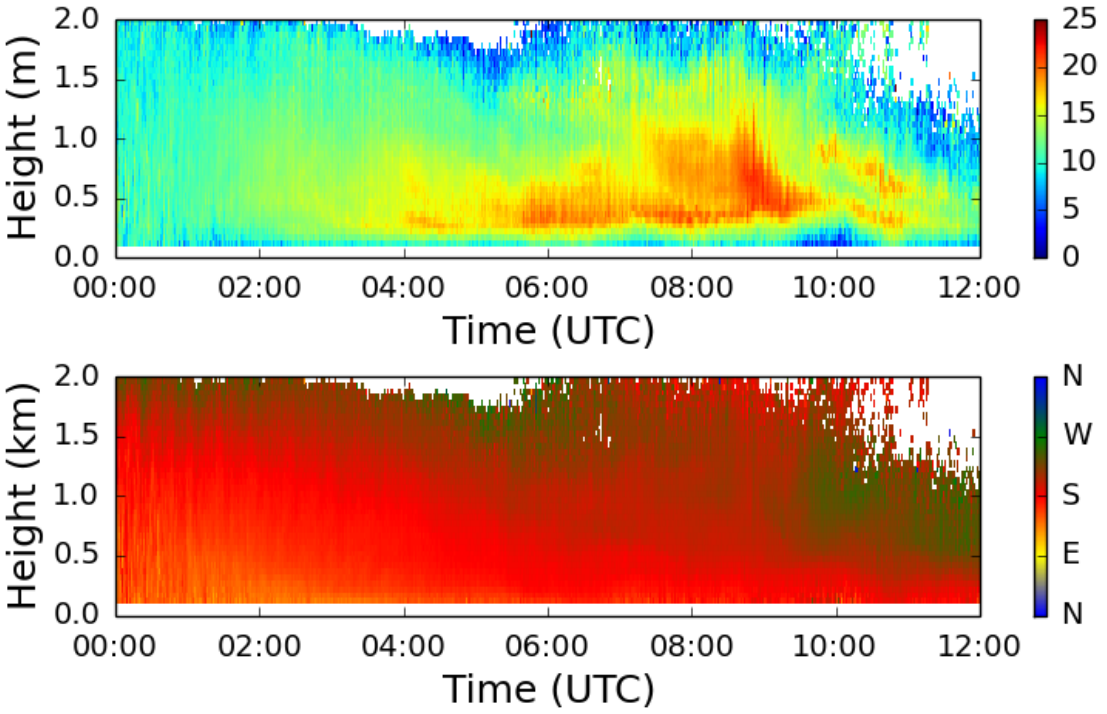

Figure 42. Wind profile time series for 5 July 2015 from the Doppler lidar at FP3. Top panel is wind speed in m s^{-1} and bottom panel is wind direction.

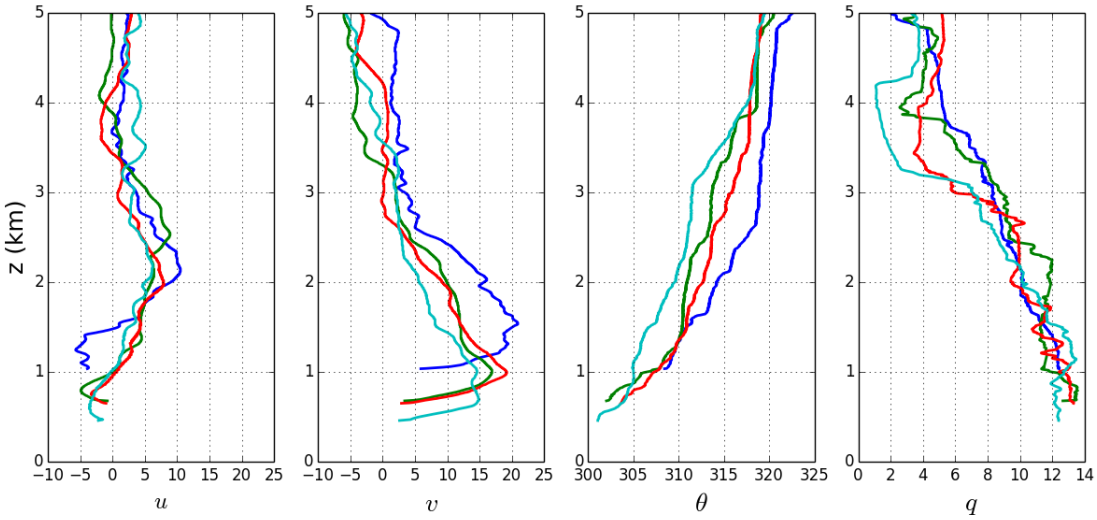

Figure 43. Profiles of *U*, *V*, potential temperature, and specific humidity, from the 5 July 2015 0600 UTC soundings at FP-5 (blue), FP-2 (green), FP-3 (red), and FP-6 (teal). The vertical coordinate is height above sea level.

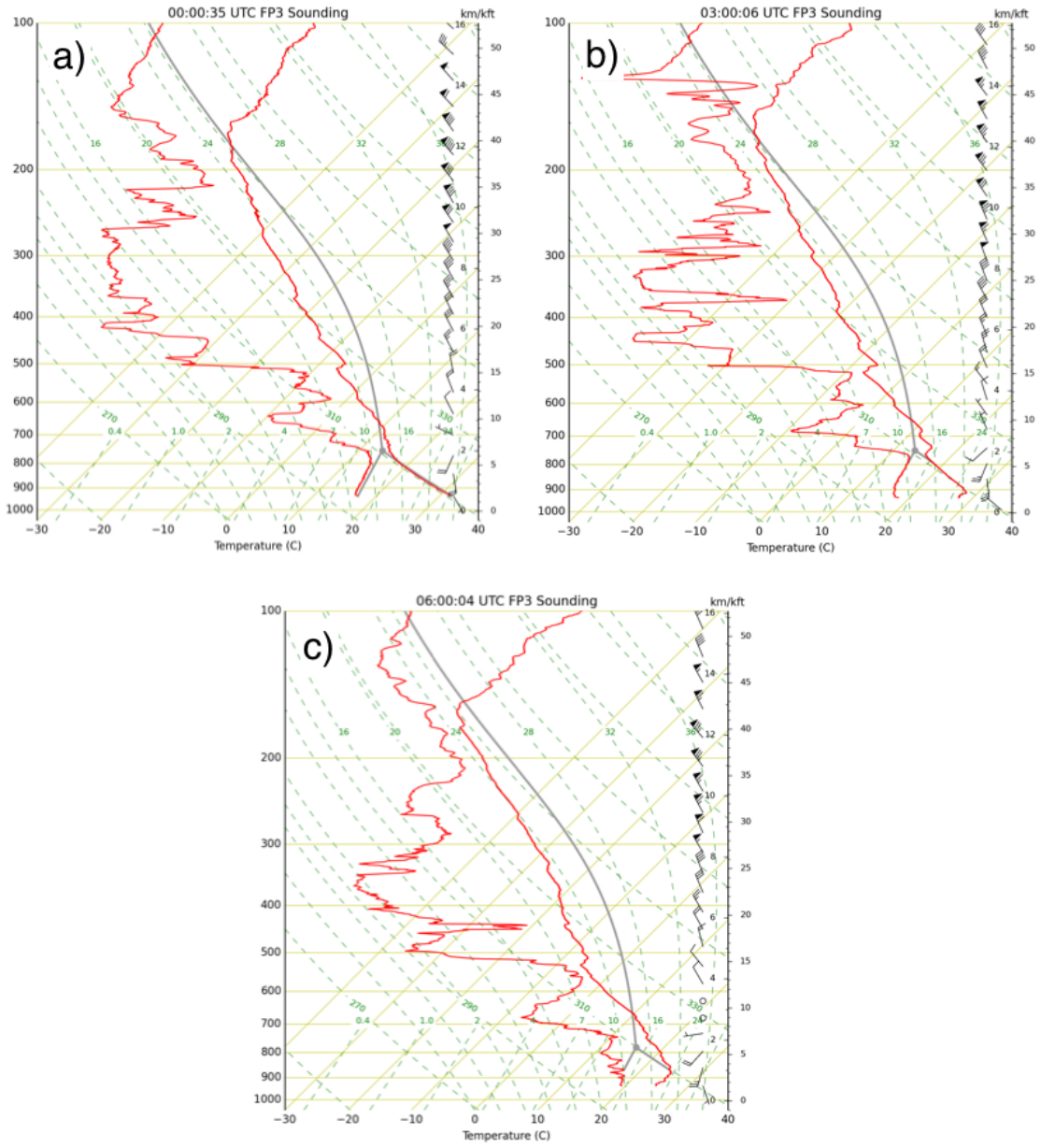

Figure 44. Soundings from FP-3 on 5 July 2015 at a) 0000 UTC, b) 0300 UTC, and c) 0600 UTC. The grey line represents the most unstable parcel.

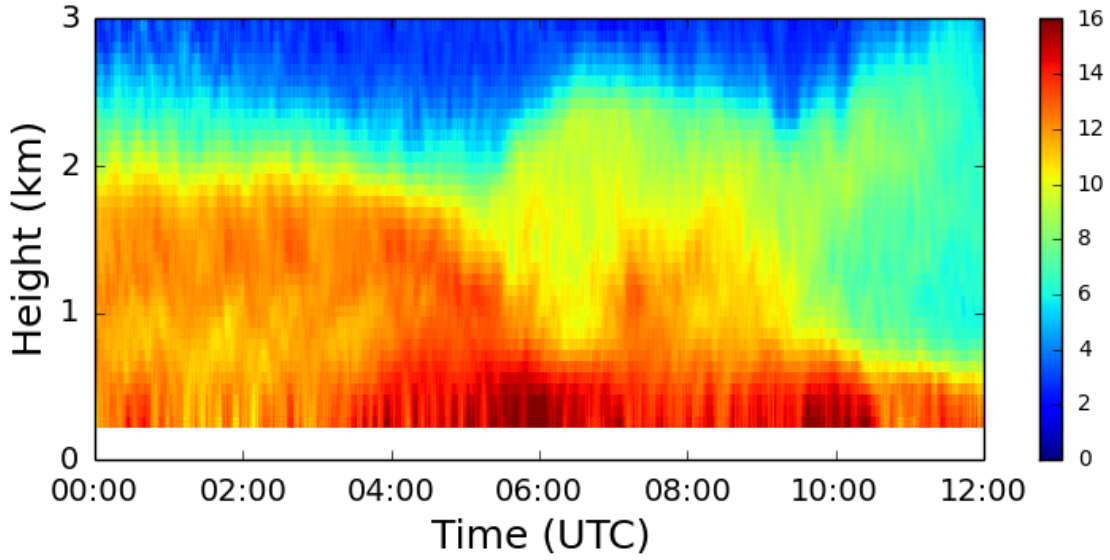

Figure 45. Water vapor profile time series from the water vapor DIAL at FP-3 for 5 July 2015. Values are g m^{-3}.

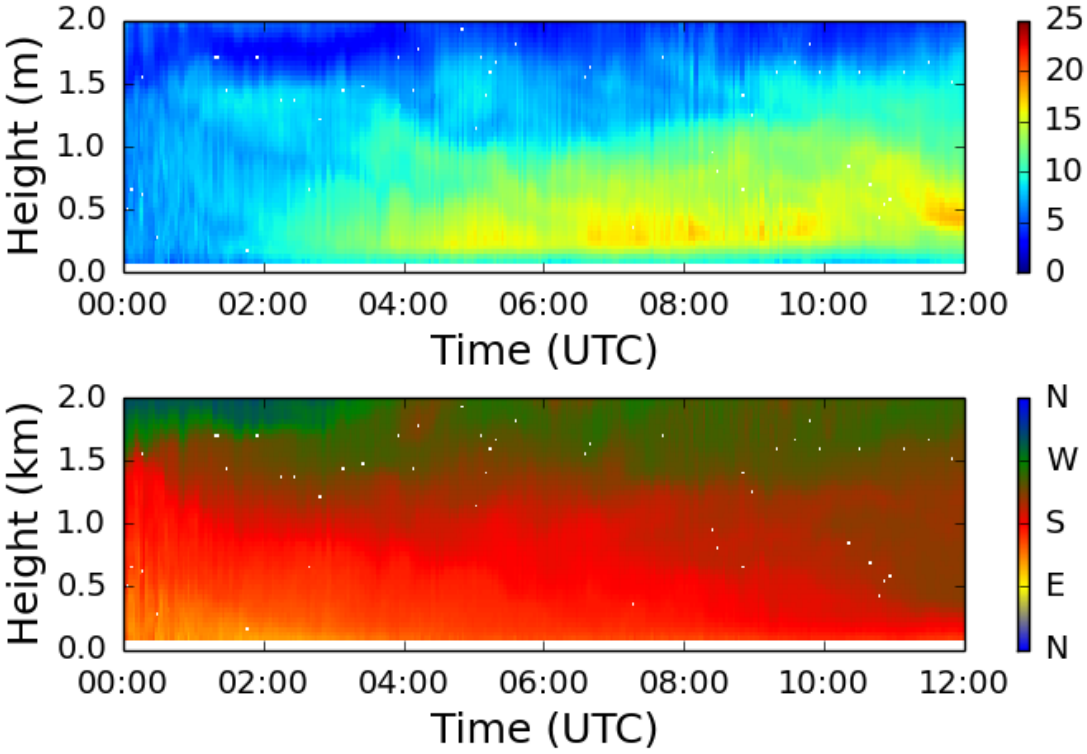

Figure 46. Wind profile time series for 5 July 2015 from the Doppler lidar at FP6. Top panel is wind speed in m s^{-1} and bottom panel is wind direction.

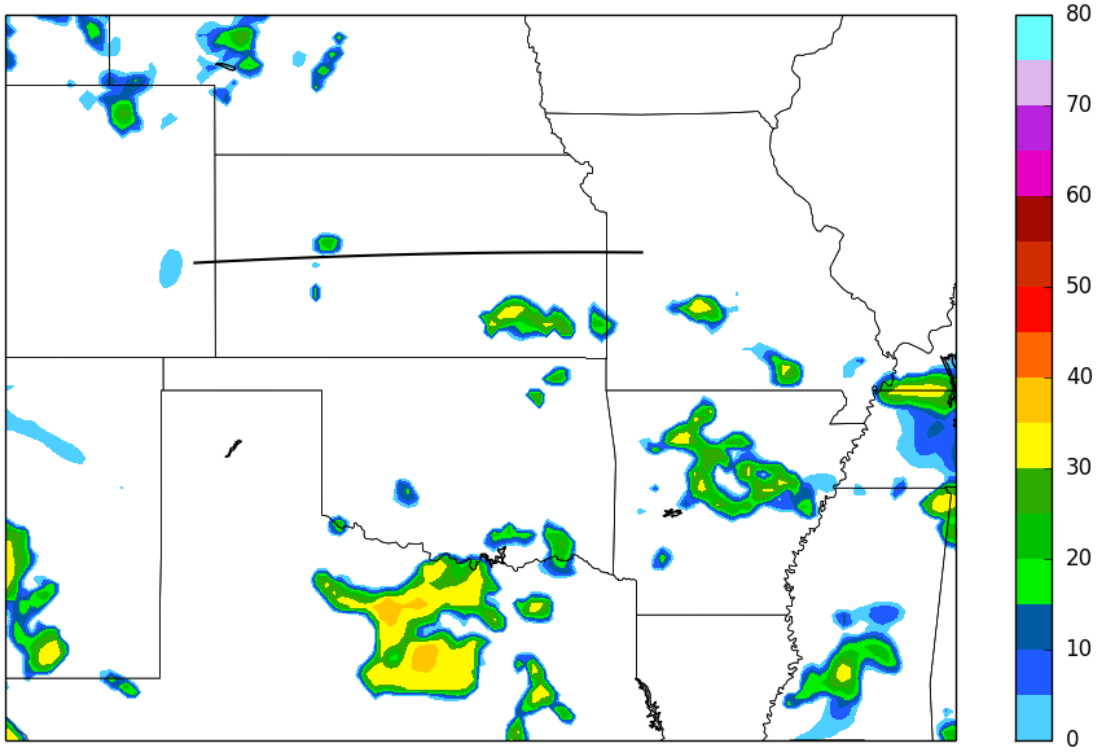

Figure 47. Simulated composite reflectivity valid for 04 UTC on 5 July 2015 from the 00 UTC RAP forecast. The black line indicates where the cross-sections were taken.

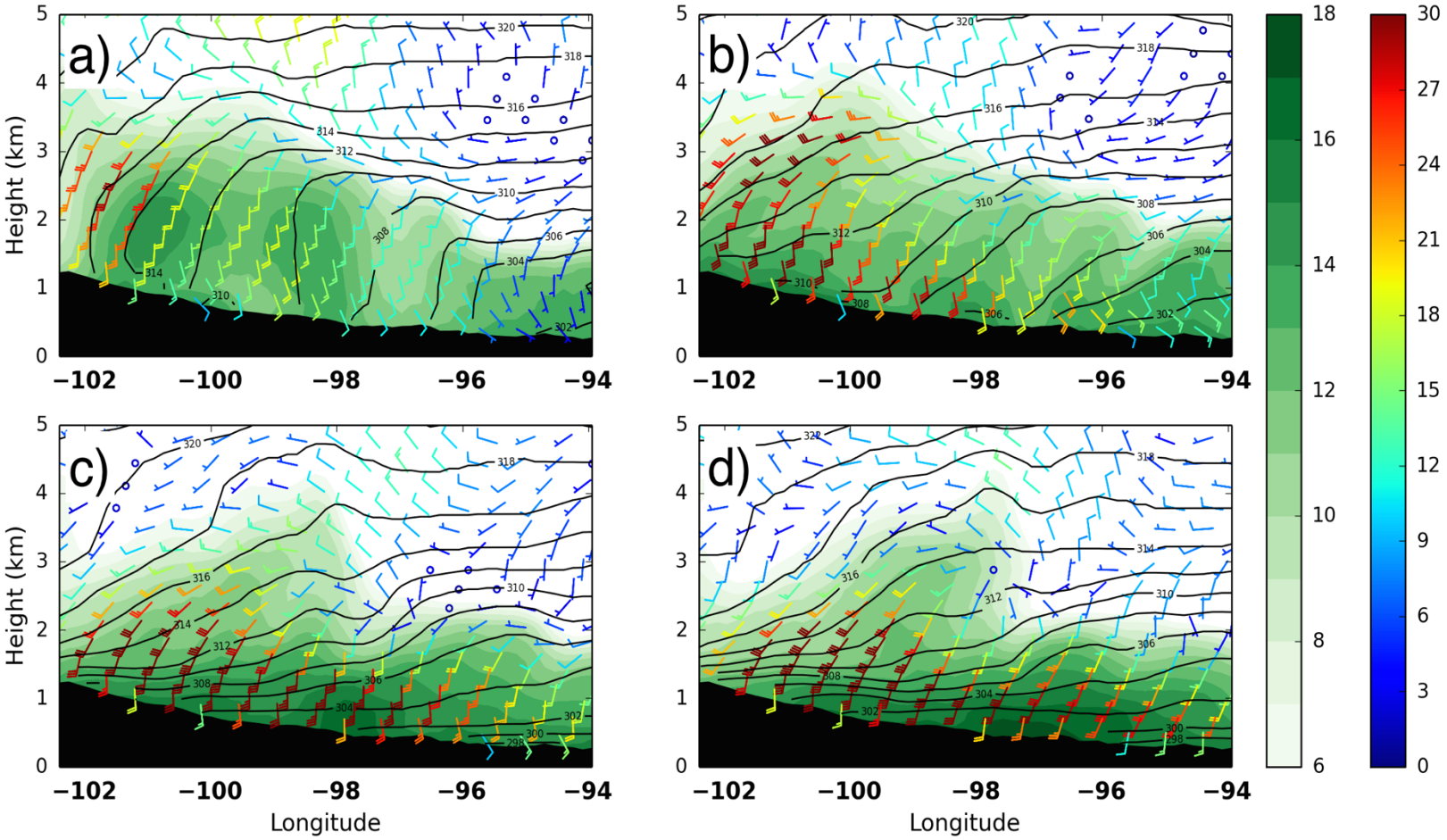

Figure 48. Cross-sections of the 5 July 2015, 00 UTC RAP forecast valid for a) 00, b) 04, c) 06, and d) 12 UTC. Potential temperature (K) is contoured in black. Specific humidity greater than 6 g kg^{-1} is shaded in green. Wind speeds are in knots.

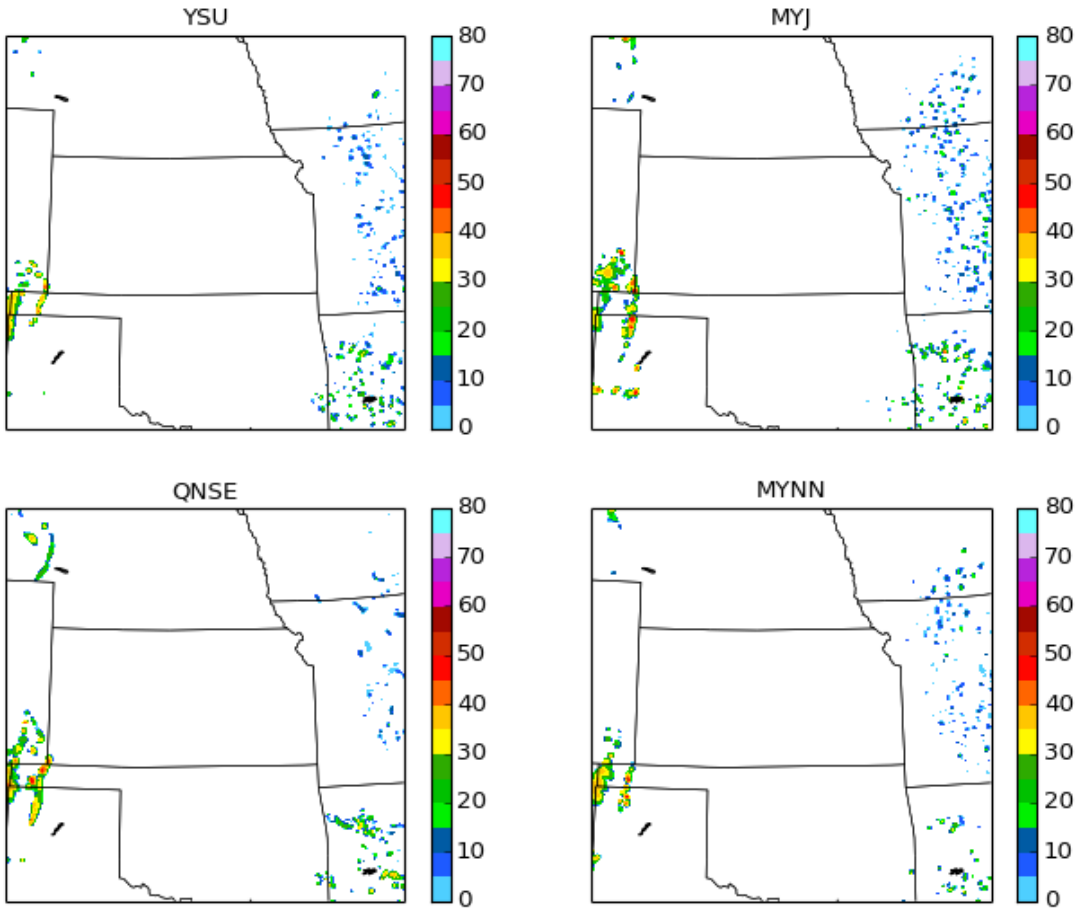

Figure 49. WRF model 1 km simulated reflectivity for 00 UTC on 2 June 2015 for four model runs with varying PBL schemes. Reflectivity values are expressed in dBZ.

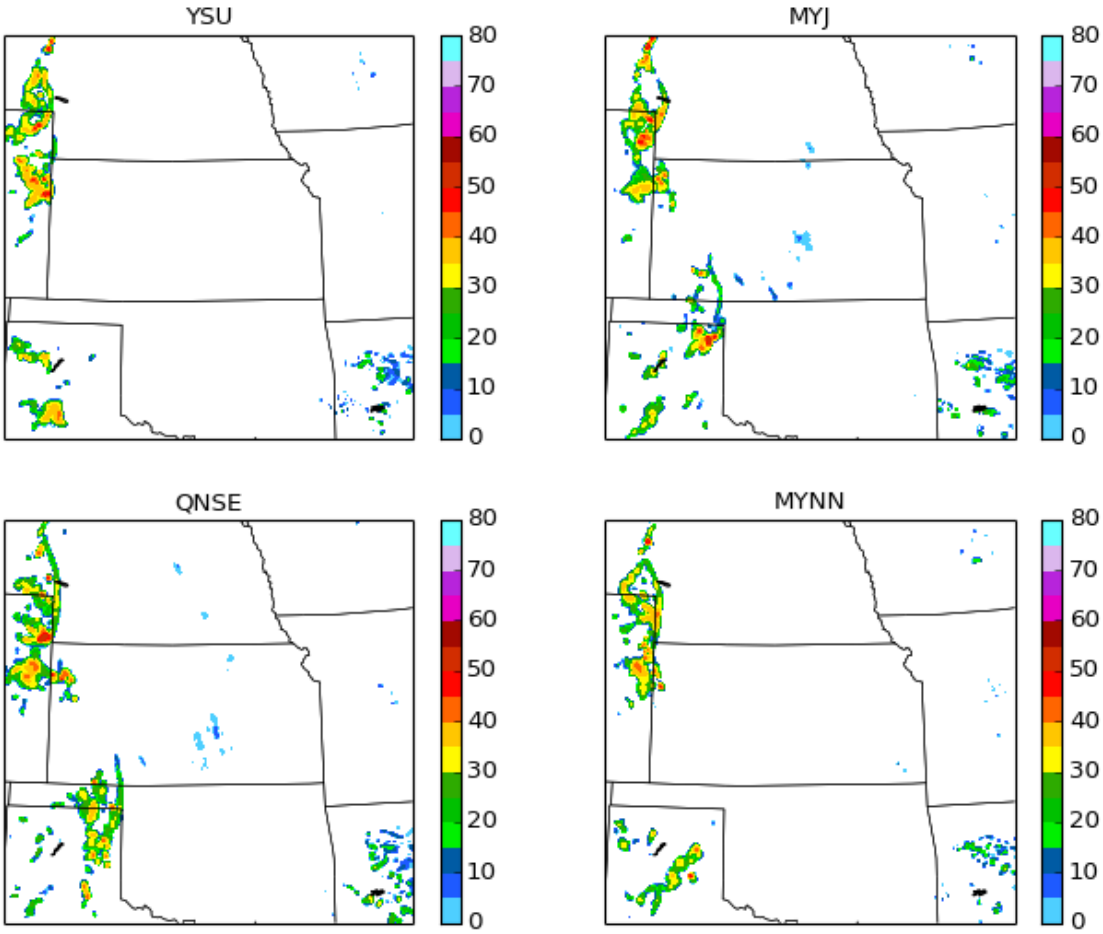

Figure 50. Same as Fig. 49 but for 04 UTC.

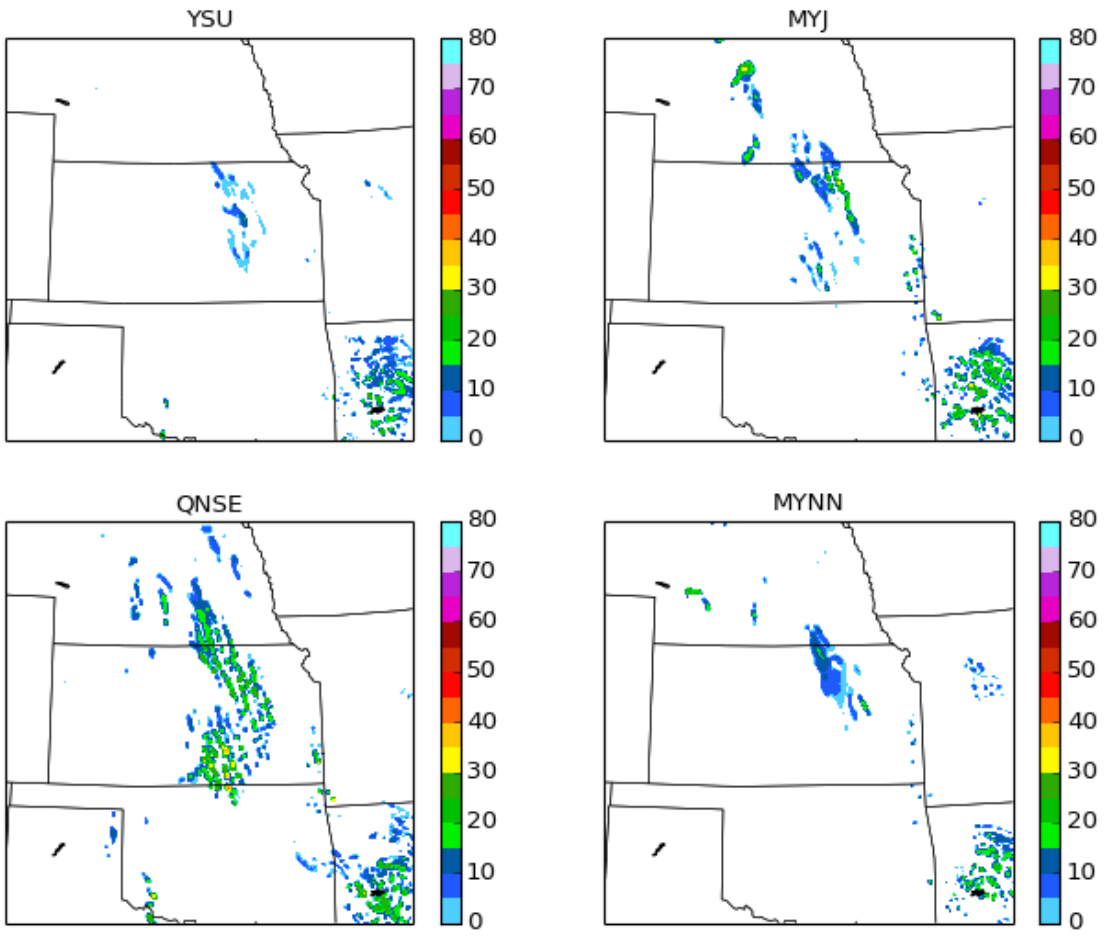

Figure 51. Same as Fig. 49 but for 08 UTC.

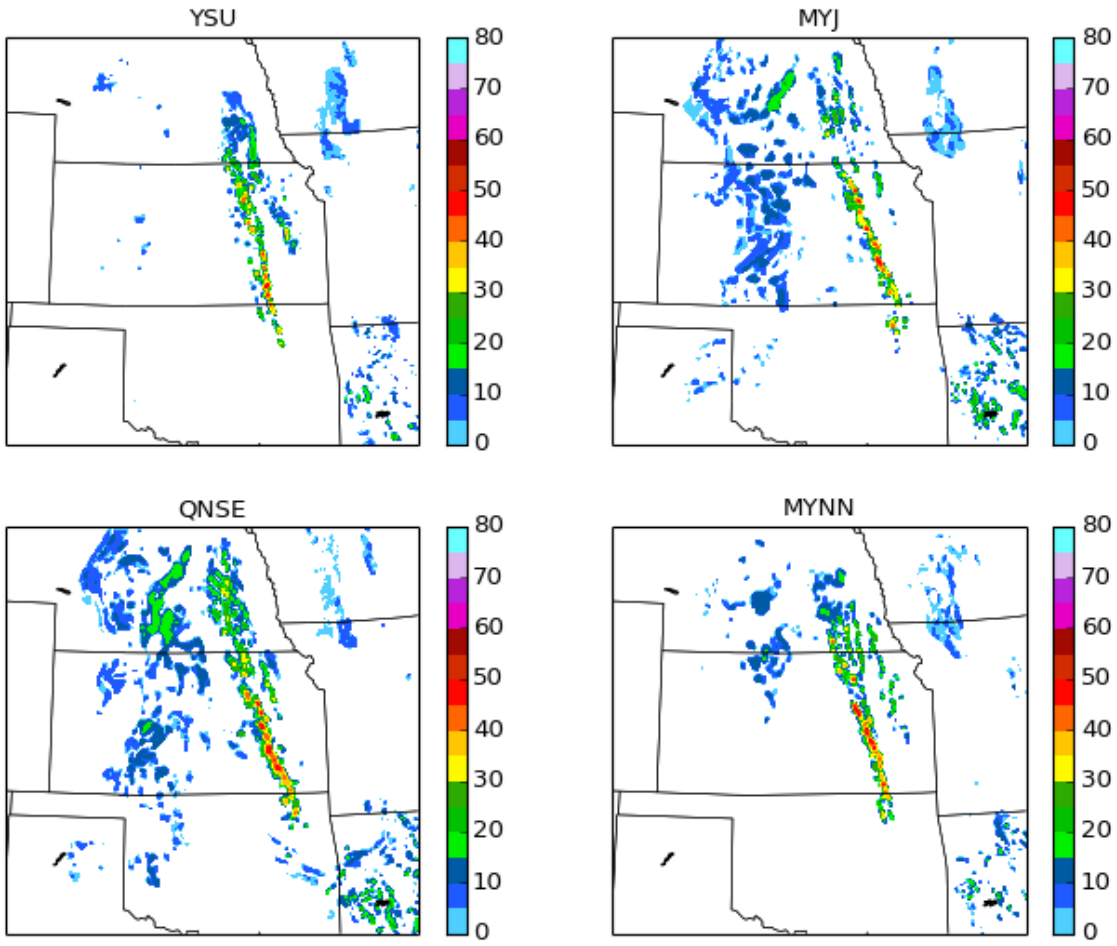

Figure 52. Same as Fig. 49 but for 12 UTC.

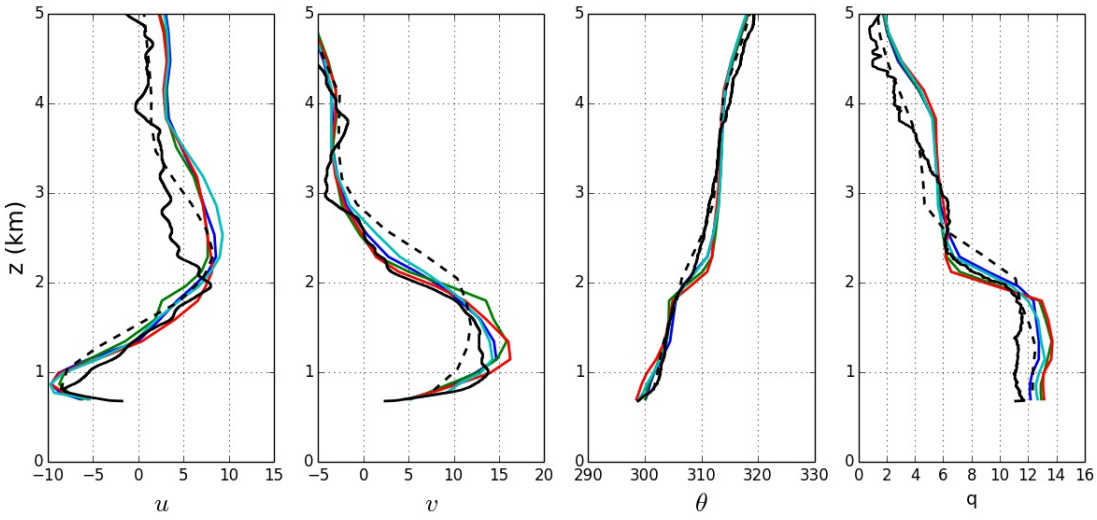

Figure 53. WRF model profiles for 03 UTC on 2 June 2015 for FP-2. The blue line represents YSU, the green line represents MYJ, the red line represents QNSE, and the turquoise line represents MYNN. The observed sounding is shown in black and and the 00 UTC RAP forecast is the dashed line.

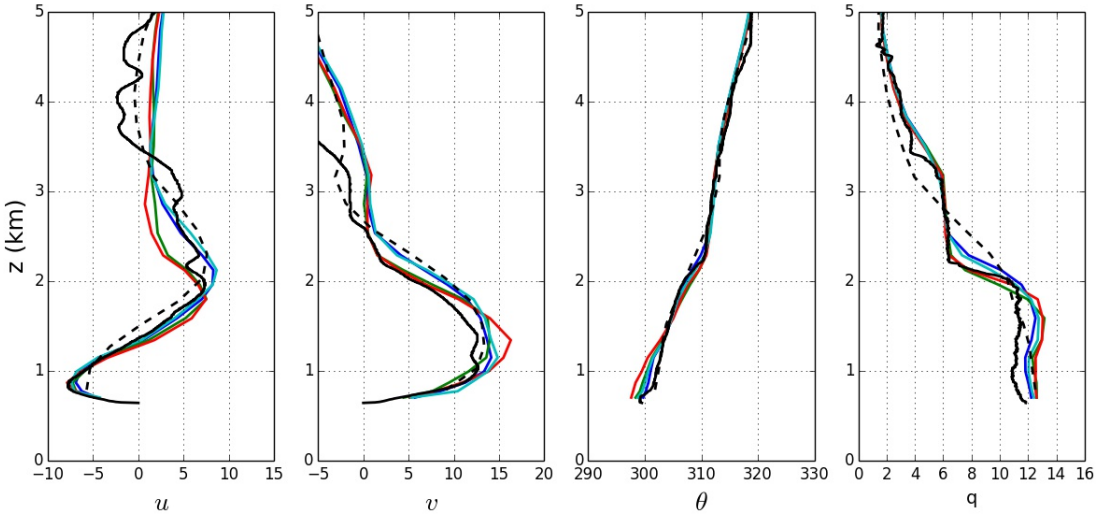

Figure 54. Same as Fig. 53 but for FP-3.

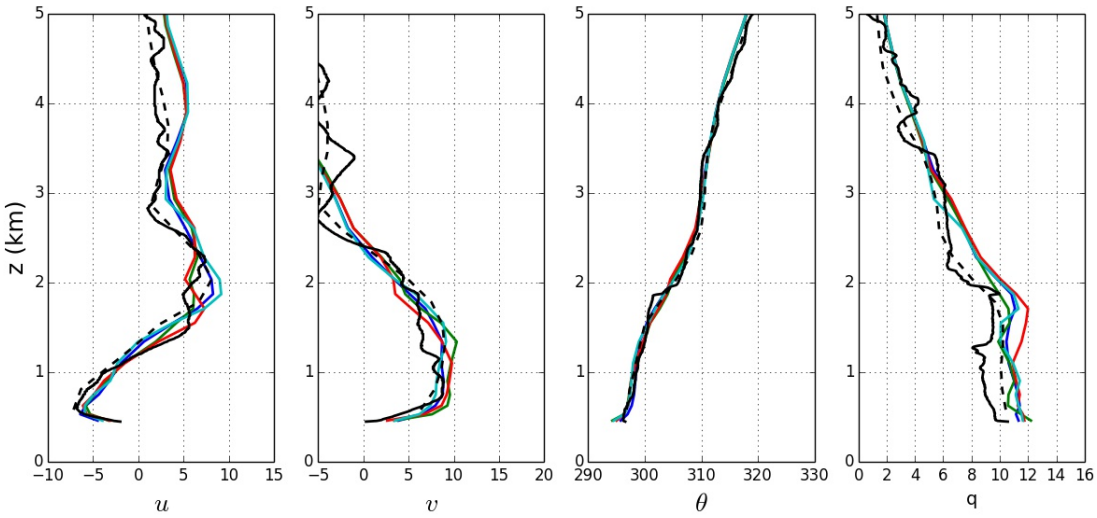

Figure 55. Same as Fig. 53 but for FP-6.

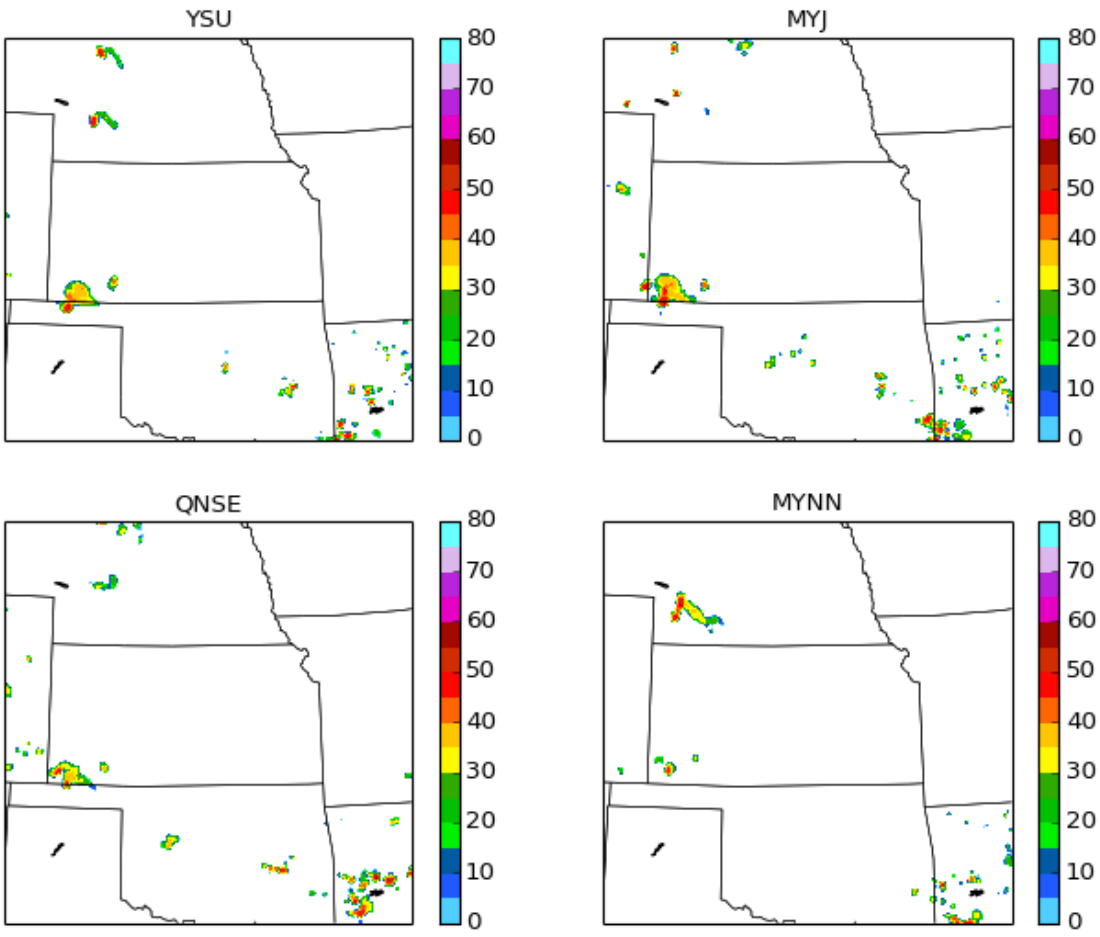

Figure 56. WRF model 1 km simulated reflectivity for 00 UTC on 5 July 2015 for four model runs with varying PBL schemes. Reflectivity values are expressed in dBZ.

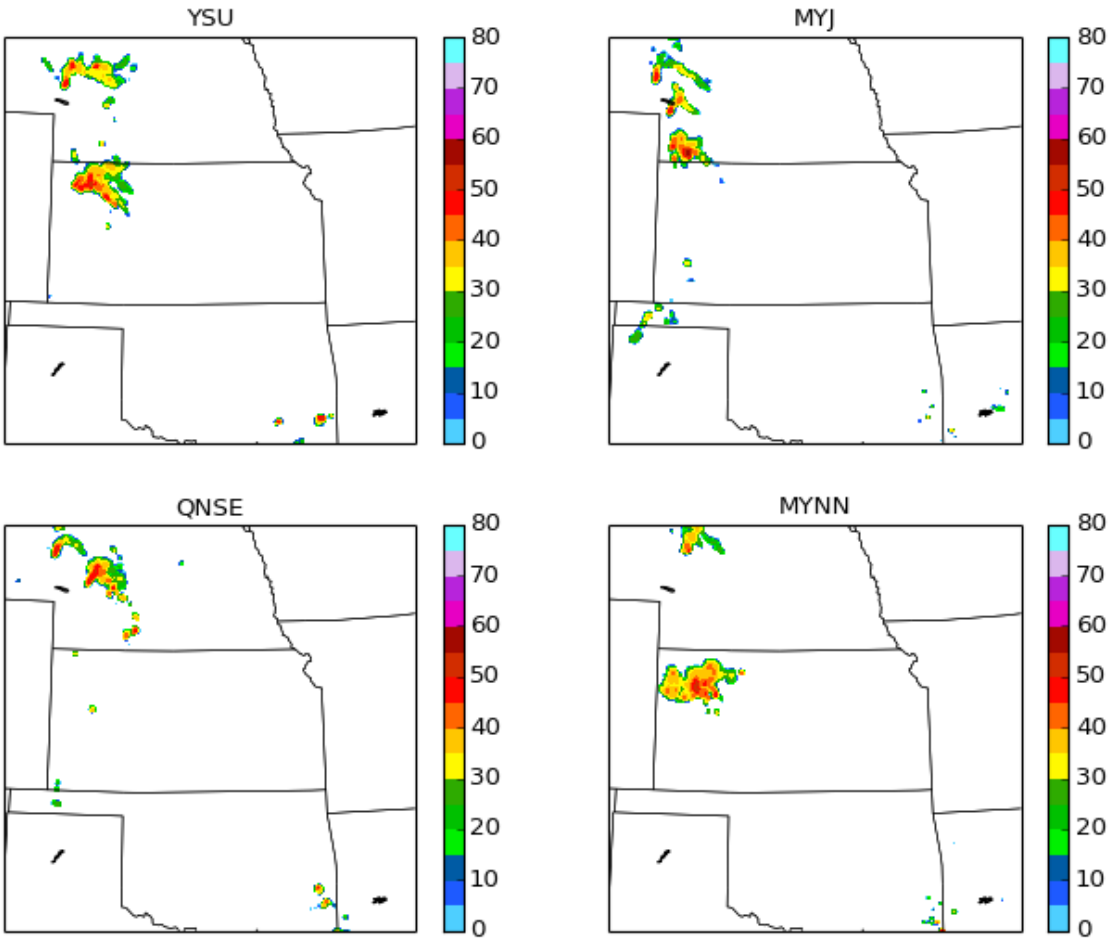

Figure 57. Same as Fig. 56 but for 04 UTC.

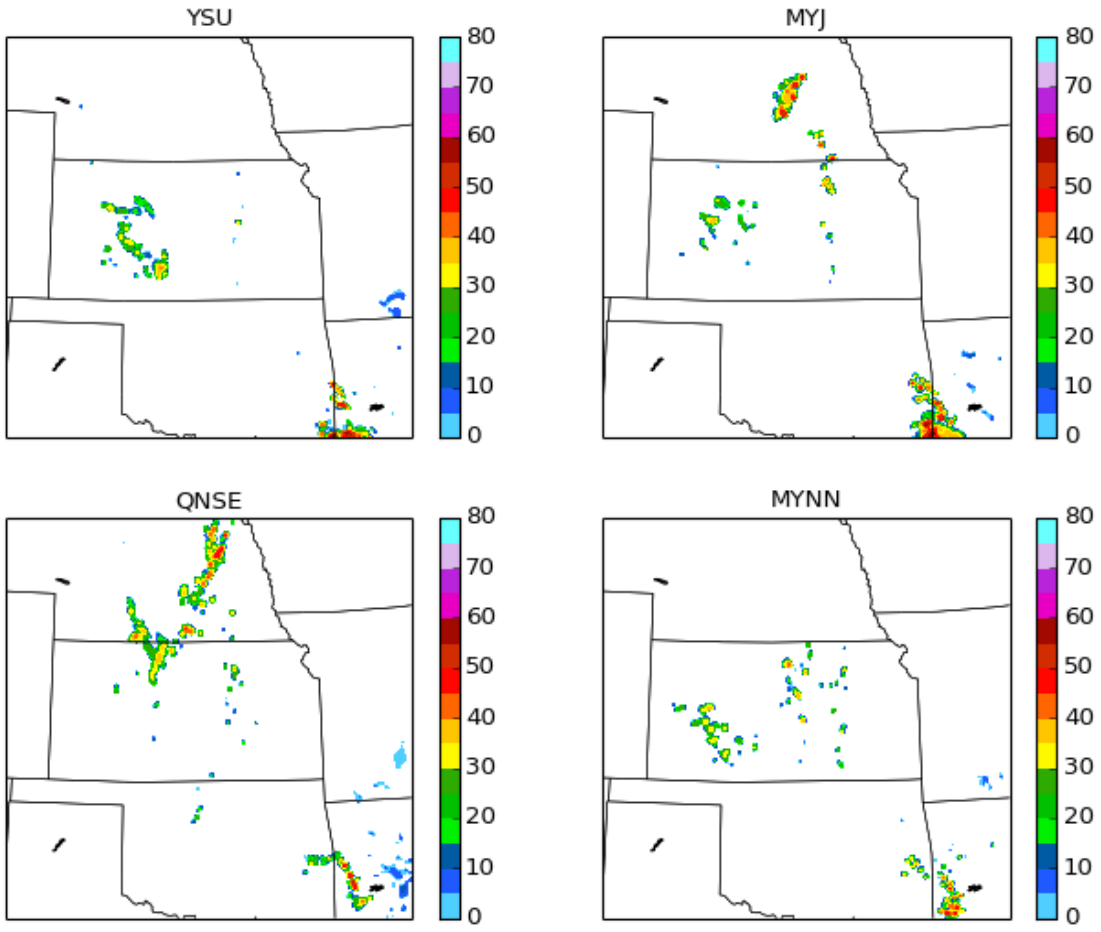

Figure 58. Same as Fig. 56 but for 08 UTC.

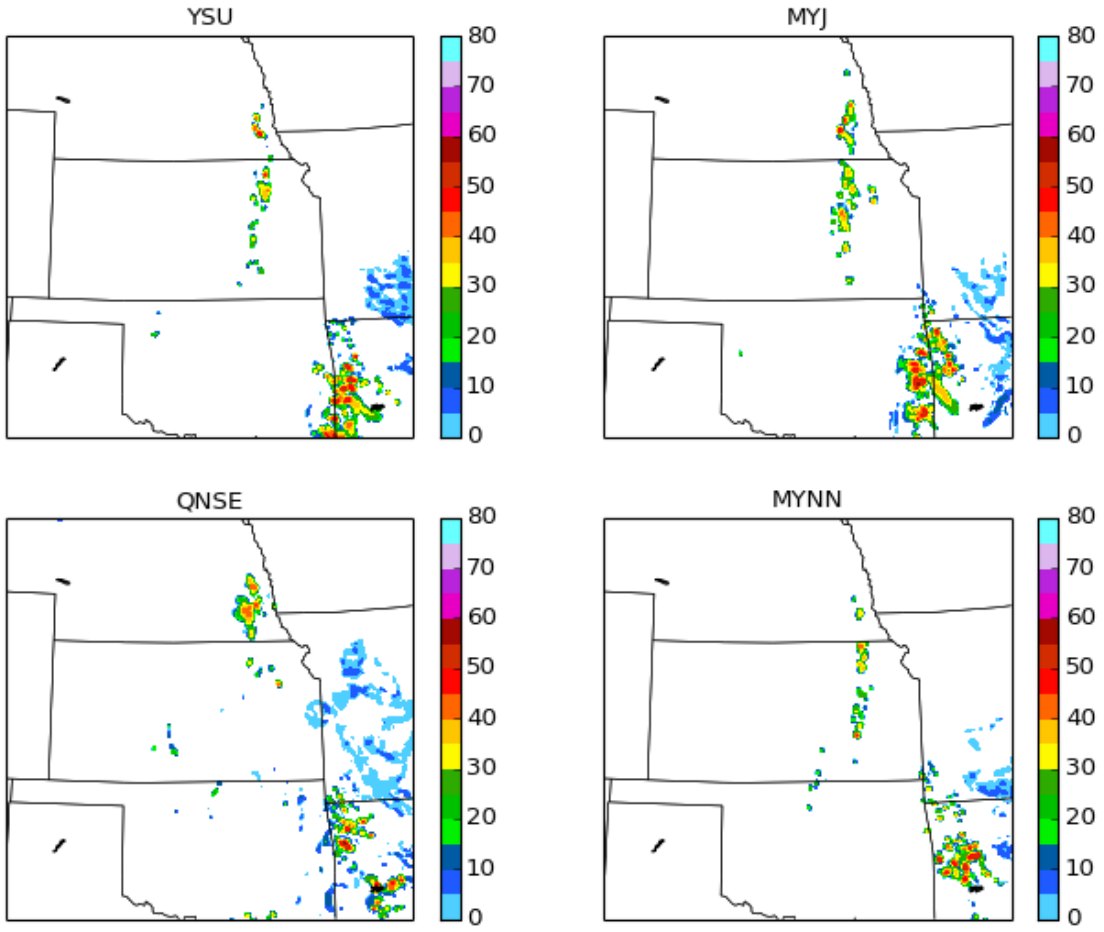

Figure 59. Same as Fig. 56 but for 12 UTC.

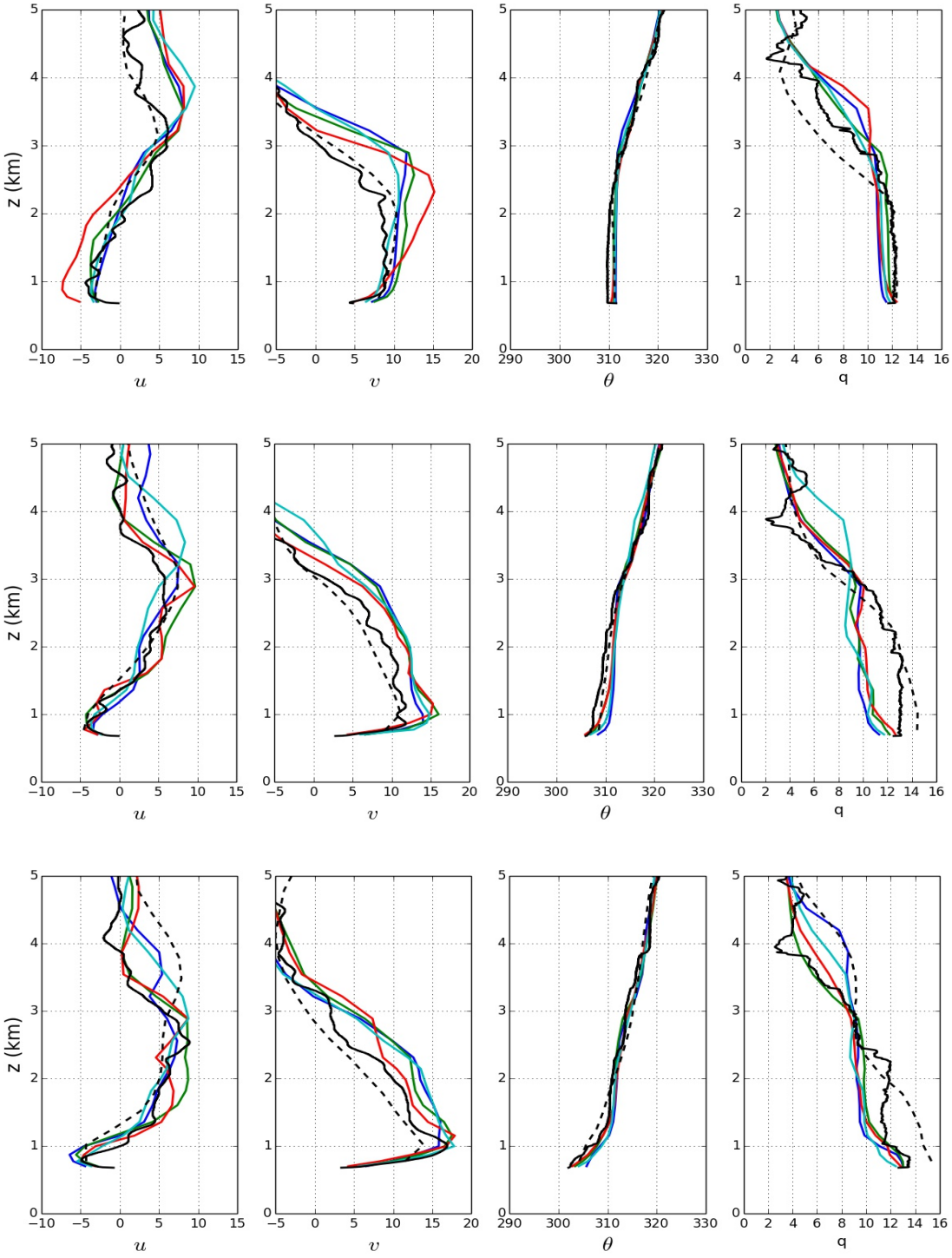

Figure 60. WRF model profiles for 00 (top), 03 (middle), and 06 (bottom) UTC on 5 July 2015 for FP-2. The blue line represents YSU, the green line represents MYJ, the red line represents QNSE, and the turquoise line represents MYNN. The observed sounding is shown in black and the 00 UTC RAP forecast is the dashed line.

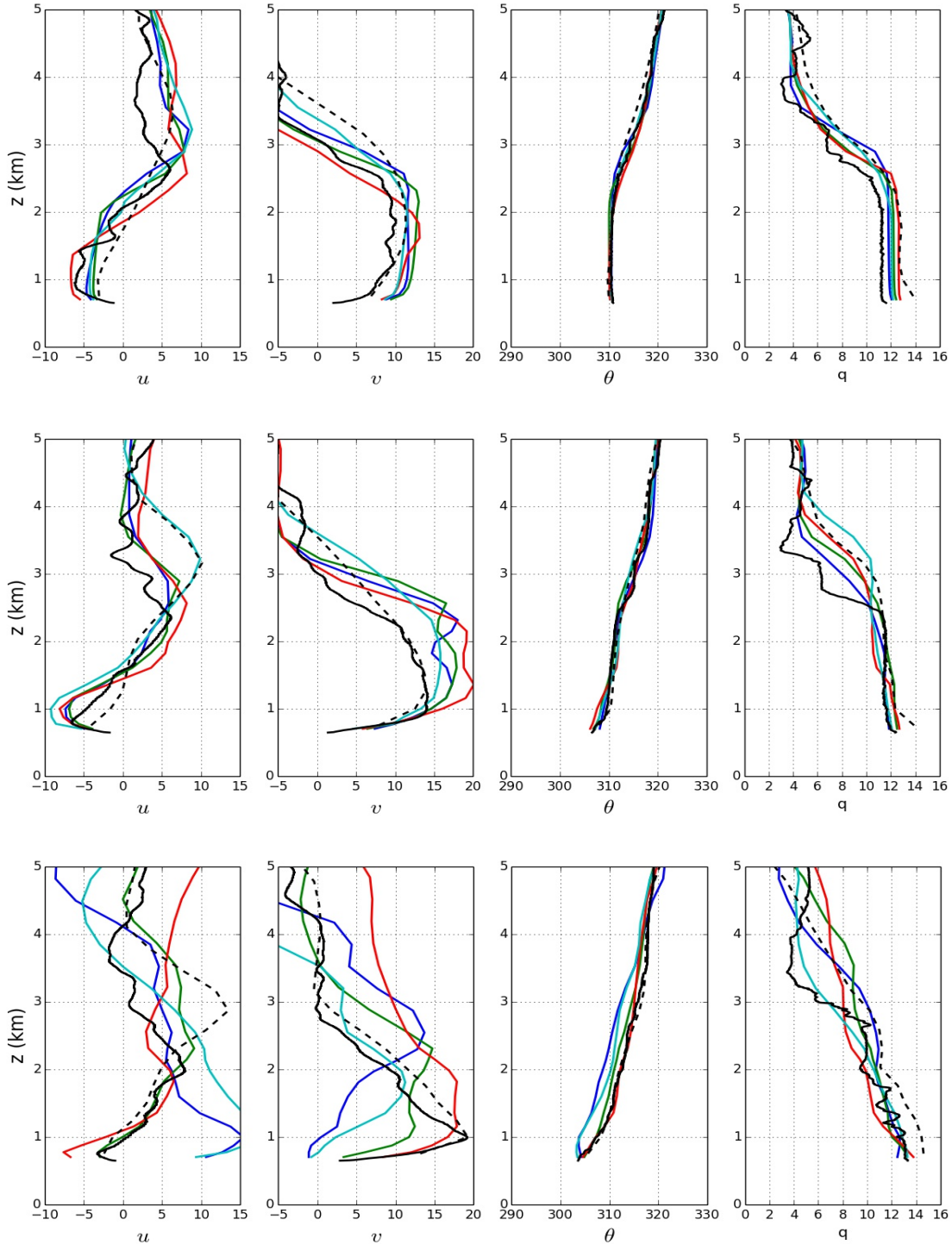

Figure 61. Same as Fig. 60 but for FP-3.

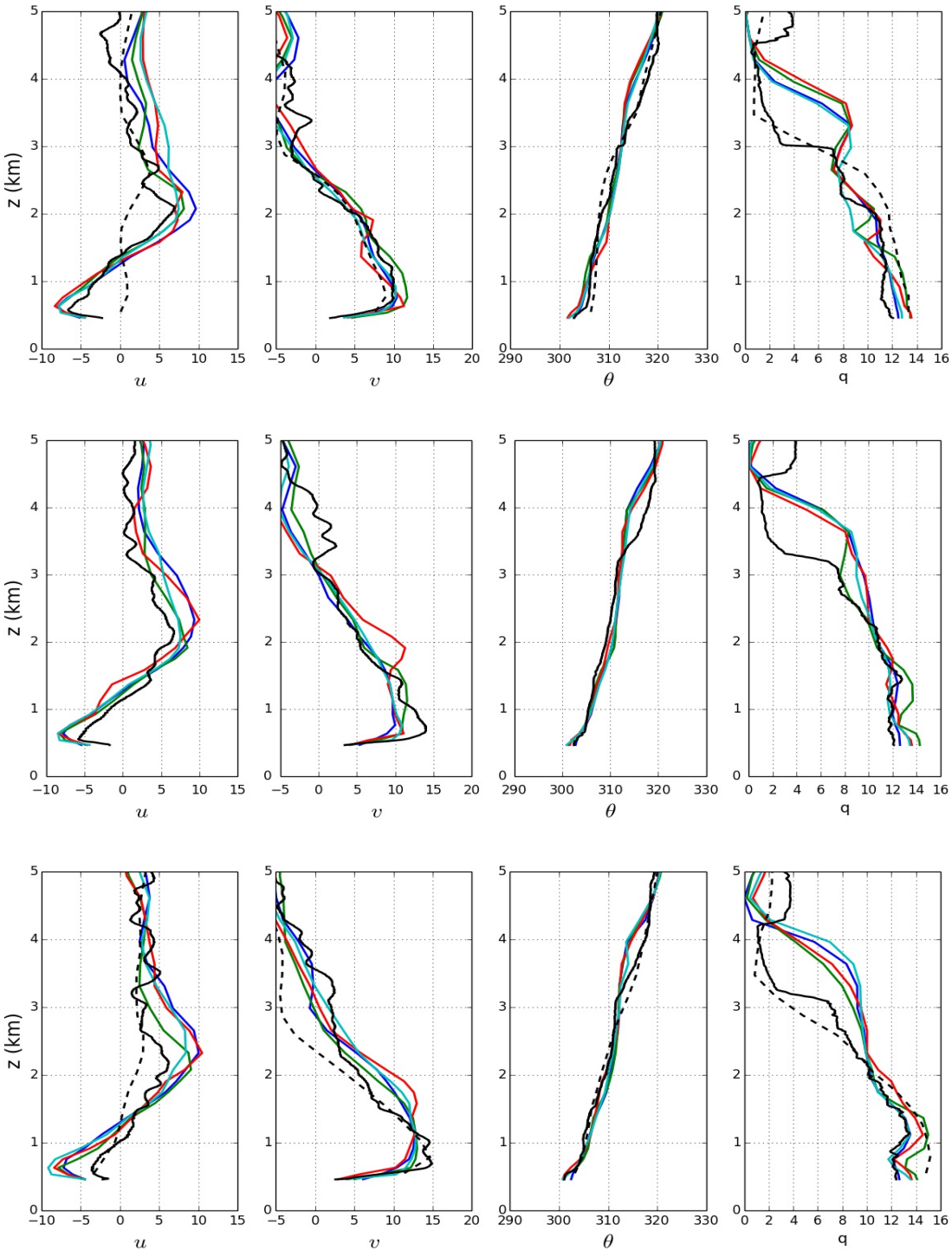

Figure 62. Same as Fig. 60 but for FP-6 at 03, 0430, and 06 UTC.

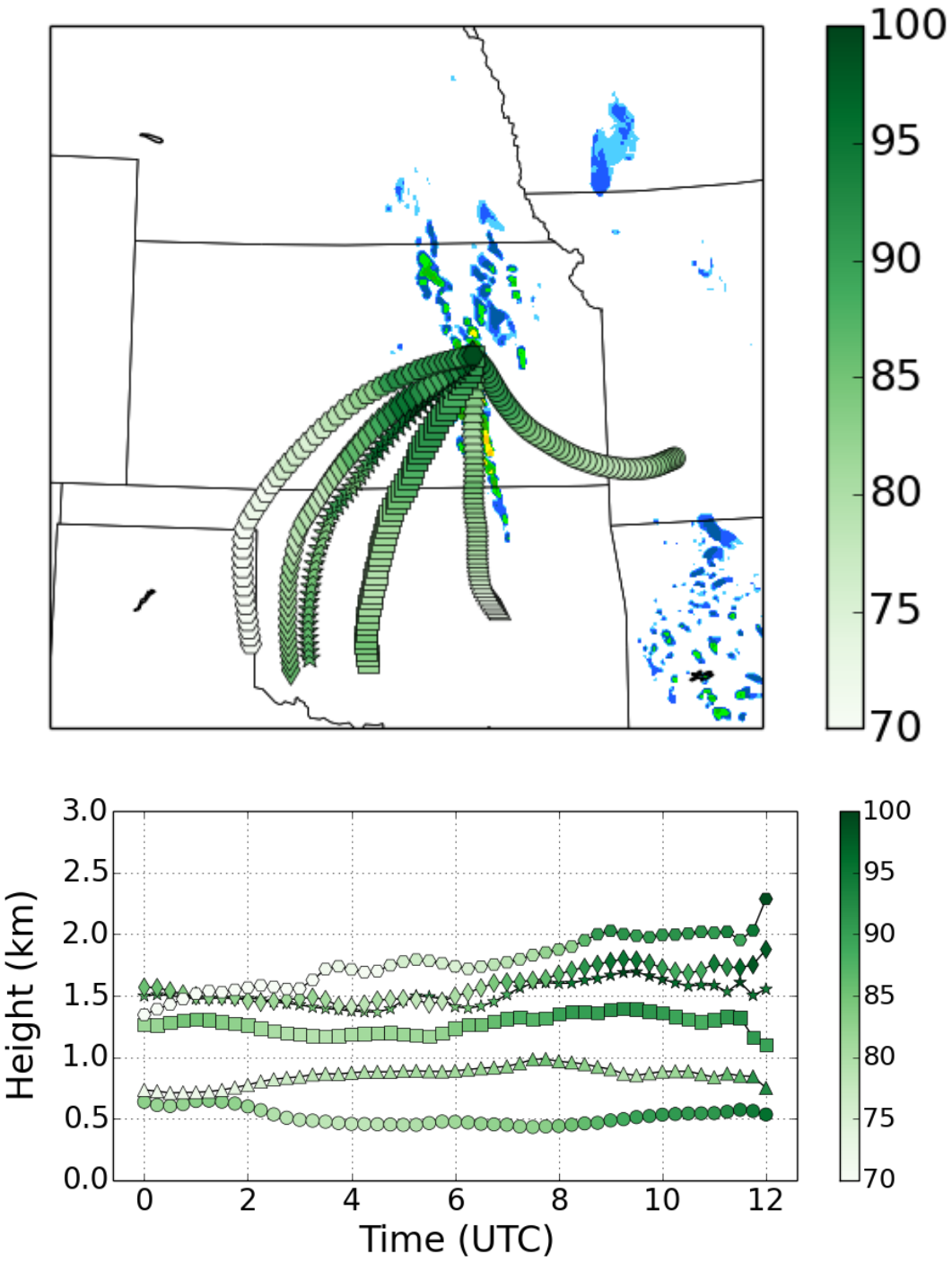

Figure 63. Back-trajectories from 00 to 12 UTC from the YSU WRF model run for 2 June 2015. Each individual trajectory has a different marker symbol. The relative humidity of the parcel is represented by the green shading of the marker.

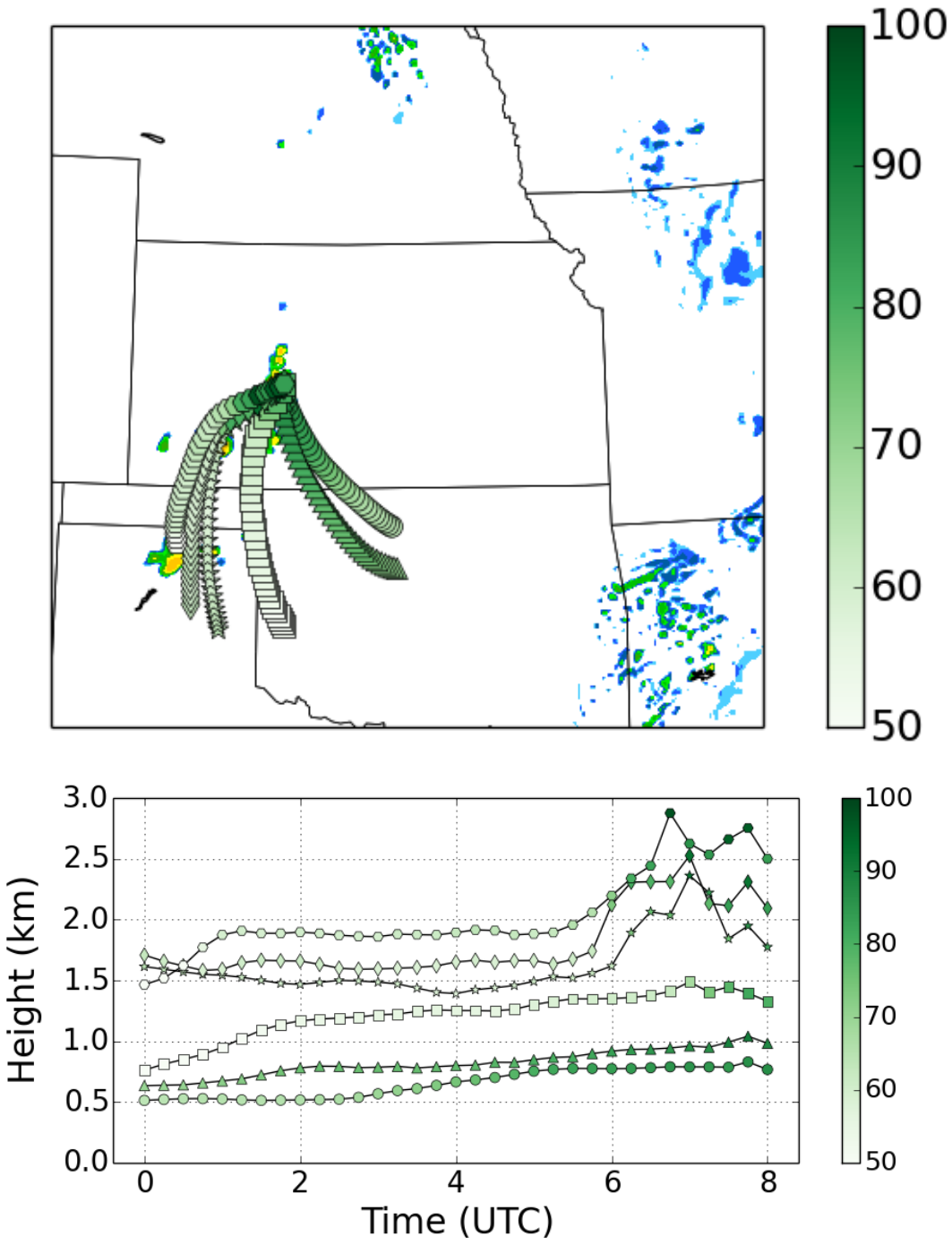

Figure 64. Back-trajectories from 00 to 08 UTC from the YSU WRF model run for 1 June 2015. Each individual trajectory has a different marker symbol. The relative humidity of the parcel is represented by the green shading of the marker.

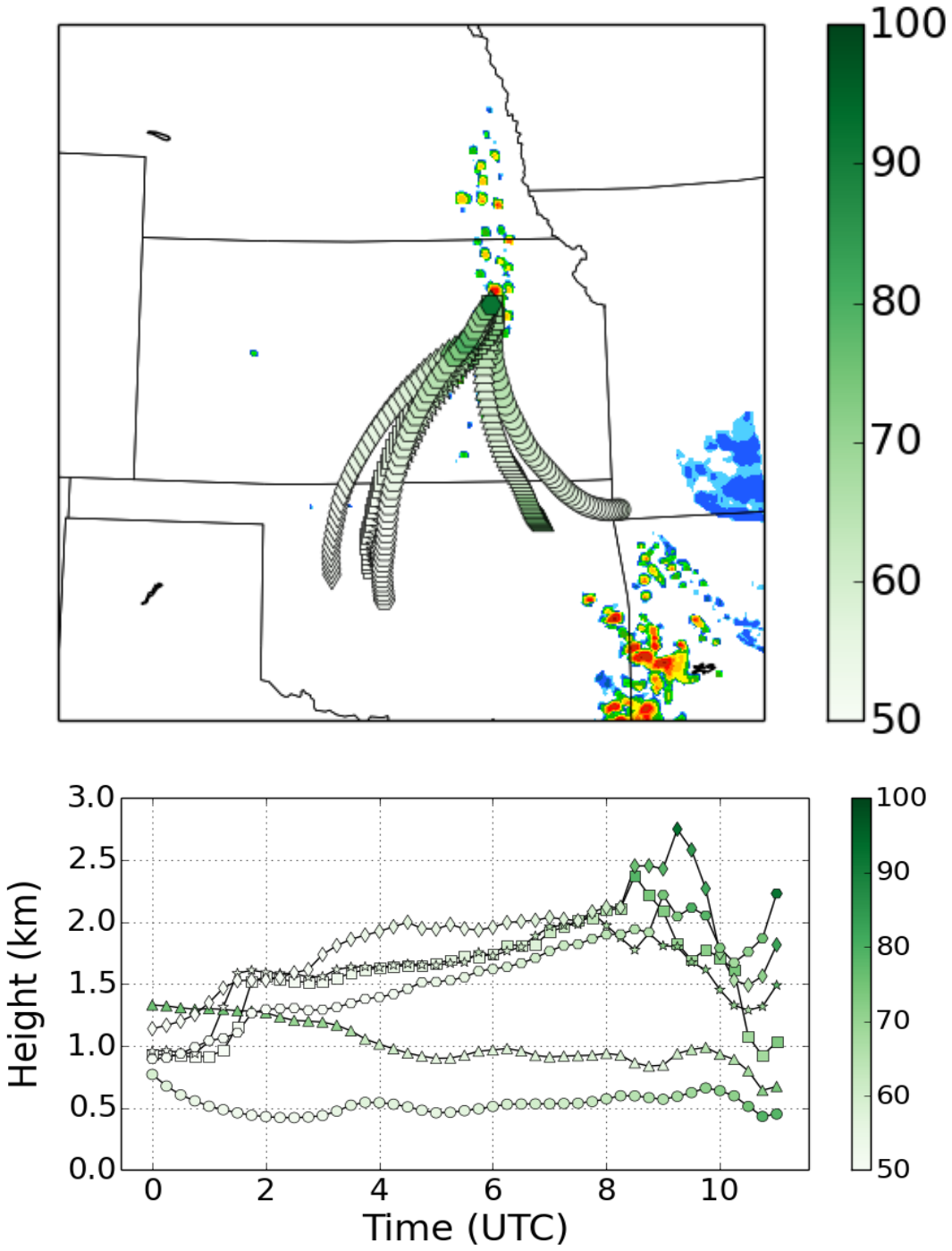

Figure 65. Back-trajectories from 00 to 11 UTC from the YSU WRF model run for 5 July 2015. Each trajectory has a different marker symbol. The relative humidity of the parcel is represented by the green shading of the marker.

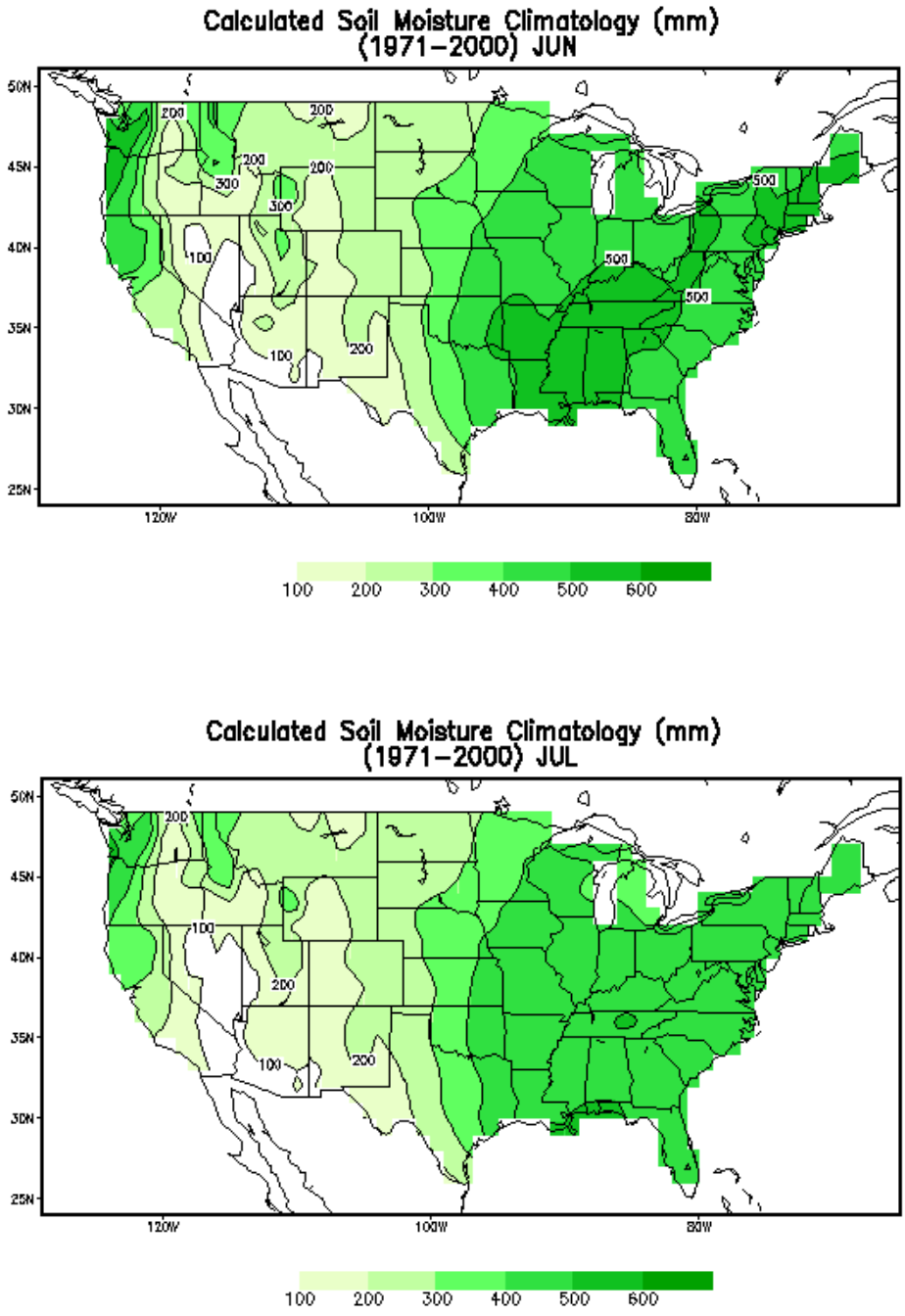

Figure 66. Climatological soil moisture values for the months of June (top) and July (bottom). Images are from the Climate Prediction Center and can be found at http://www.cpc.ncep.noaa.gov/products/Soilmst_Monitoring/US/Soilmst/Soilmst.shtml.

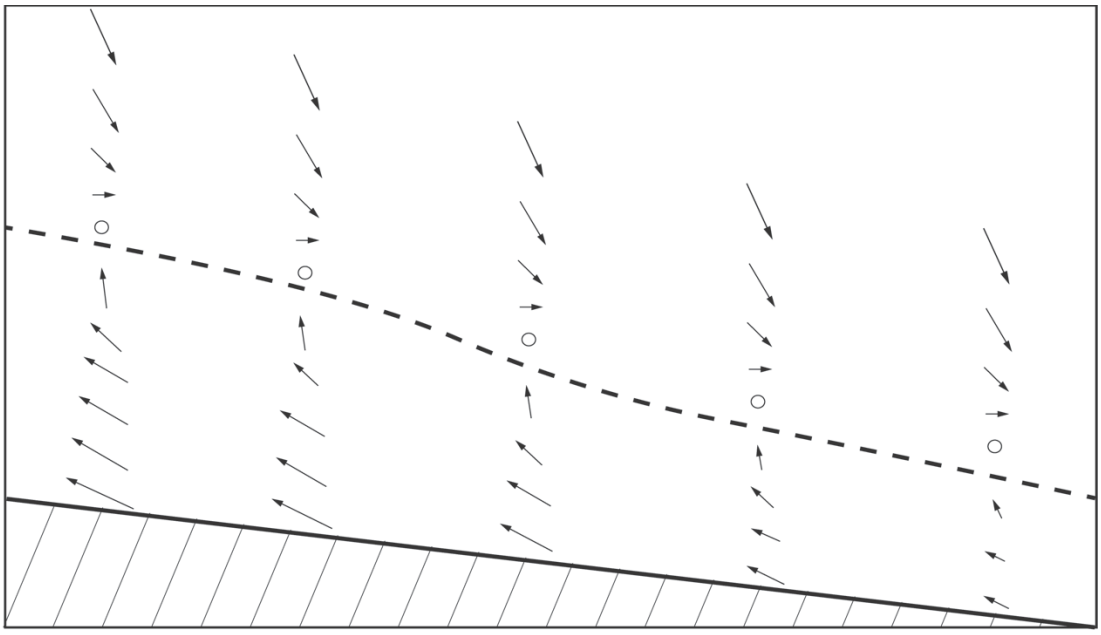

Figure 67. A conceptual diagram of a before sunset cross-section across a slope with a buoyancy gradient. The dashed line represents the top of the boundary layer and the arrows are the horizontal wind vectors.

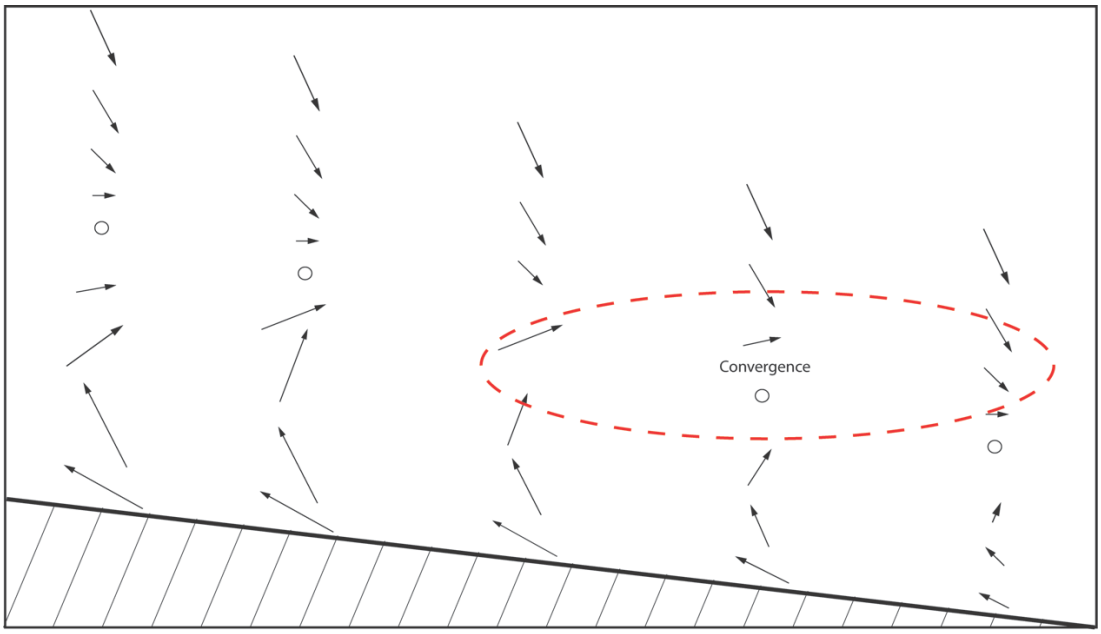

Figure 68. A conceptual diagram of a cross-section of a mature LLJ when a buoyancy gradient is present.